POLYTYPISM AND THE VIBRATIONAL PROPERTIES OF PbI_2

by

WILLIAM MAXWELL SEARS, B.Sc.(Hon.), M.Sc.

A Thesis

Submitted to the School of Graduate Studies

in Partial Fulfilment of the Requirements

for the Degree

Doctor of Philosophy

McMaster University

May 1978

POLYTYPISM AND THE VIBRATIONAL PROPERTIES OF PbI_2

DOCTOR OF PHILOSOPHY (1978) McMASTER UNIVERSITY

(Physics) Hamilton, Ontario

TITLE: Polytypism and the Vibrational Properties of PbI_2

AUTHOR: William Maxwell Sears, B.Sc.(Hon.) (Acadia University)

M.Sc. (McMaster University)

SUPERVISOR: Professor J. A. Morrison

NUMBER OF PAGES: xiv, 140

ABSTRACT

The vibrational properties of polytypes of PbI_2 crystals have been studied experimentally by means of the techniques of Raman spectroscopy, X-ray diffraction and low temperature calorimetry. The crystals were prepared by three different methods: gel growth, thermal annealing and growth from the melt.

The Raman spectra are used to determine features of the phonon dispersion curves, in the crystallographic c-direction, that are common to all of the polytypes. The results are correlated with existing information obtained from measurements of Brillouin spectra and inelastic scattering of neutrons.

Both the heat capacity and the thermal conductivity were determined from the calorimetric measurements in the region $0.5 < T < 4$ K. The thermal conductivity is found to be surprisingly small. Another thermodynamic quantity, the thermal expansion, was obtained from measurements of the lattice parameters of PbI_2 as a function of temperature in the range $100 < T < 300$ K.

All of the results are analysed within the framework of a 6-parameter force constant model. Bounds are placed on the magnitudes of anharmonic and 2-dimensional contributions to the vibrational properties.

ACKNOWLEDGEMENTS

I would like to thank my supervisory committee for their help in the various stages of this thesis. They have included; J. A. Morrison, C. Calvo, M. L. Klein, and D. Walton.

Thanks also go to H. E. Howard-Lock for permission to use the Raman spectrometer, to J. E. Greedan and J. D. Garrett for assistance with crystal growing, and to R. Faggiani for assistance with the X-ray work.

Finally I would like to especially thank the typist of this manuscript without whose work this thesis would not be possible.

DEDICATION

To SUSAN CAROLINE RUSSELL for 10 years.

TABLE OF CONTENTS

CHAPTER (SECTION)		PAGE
1	INTRODUCTION	1
2	EXPERIMENTAL	6
2.1	Preparation/Identification of Polytypes	6
2.1.1	The Technique of Crystal Growth in Gels	6
2.1.2	Preparation of Crystals of PbI_2	7
2.1.3	Experimental Conditions Studied	8
2.1.4	Identification of Polytypes with X-rays	9
2.1.5	Results of Gel-Growth Experiments	27
2.1.6	Preparation of Polytypes by Thermal Treatment of 2H Crystals	28
2.2	Determination of Raman Spectra	31
2.2.1	The Spectrometer and Laser	31
2.2.2	Spectrometer Accuracy	32
2.2.3	Polarization Experiments	33
2.2.4	Low Temperature Cryostat	33
2.3	Heat Capacity Measurements	36
2.3.1	Preparation of Crystal Specimen	36
2.3.2	Calorimetric Technique	38
2.3.3	Assessment of Accuracy	40
2.4	Expansivity Measurements	43
2.4.1	Adaptation of an X-ray Diffractometer	43
2.4.2	Assessment of Accuracy	43

CHAPTER (SECTION)		PAGE
3	EXPERIMENTAL RESULTS	46
3.1	Raman Spectra at Room and Low Temperatures	46
3.1.1	General View of the Raman Effect in Layered Materials	46
3.1.2	Raman Spectra of 2H-PbI_2	47
3.1.3	Raman Spectra of 4H-PbI_2	53
3.1.4	Raman Spectra of 6H-PbI_2	61
3.1.5	Raman Spectra of 8H-PbI_2	68
3.1.6	Raman Spectra of 12H-PbI_2	73
3.1.7	Raman Spectra of 12R-PbI_2	78
3.2	Correlation of Raman Freqencies with other Information on Vibrational Structure	84
3.2.1	Acoustic Branches	84
3.2.2	Optical Branches	86
3.3	Heat Capacities at Low Temperatures	90
3.4	Thermal Conductivity of PbI_2	96
3.4.1	General Remarks	96
3.4.2	Determination of the Thermal Conductivity	96
3.4.3	Numerical Results	100
3.5	Thermal Expansion	106

CHAPTER (SECTION)		PAGE
4	DISCUSSION	111
4.1	A Vibrational Model for PbI_2	111
4.1.1	Calculation of Force Constants	111
4.1.2	Comparison of Results	120
4.1.3	Anharmonic Effects	126
4.2	A Search for 2-Dimensional Effects	130
5	CONCLUSION	134
	REFERENCES	136

LIST OF FIGURES

FIGURE NO.		PAGE
1	Gel Growth Preparations	11
2	X-ray Photographs of OKL Reciprocal Plane	15
3	Low Temperature He^4 Cryostat for Raman Scattering	34
4	Bridgman Growth of PbI_2	37
5	Calorimeter	39
6	Temperature Variation During a Pulse	42
7	Syntex Low Temperature Attachment	44
8	Raman Spectrum of PbI_2 Polytype 2H at Room Temperature	49
9	Raman Spectrum of PbI_2 Polytype 2H at 50 K	50
10	Raman Spectrum of PbI_2 Polytype 4H at Room Temperature	55
11	Raman Spectrum of PbI_2 Polytype 4H at 50 K	56
12	Phonon Dispersion Curves from Raman (4H) Measurements	59
13	Phonon Dispersion Curves from Raman (6H) Measurements	63
14	Raman Spectrum of PbI_2 Polytype 6H at Room Temperature	64
15	Raman Spectrum of PbI_2 Polytype 6H at 50 K	65
16	Phonon Dispersion Curves from Raman (8H) Measurements	69
17	Raman Spectrum of PbI_2 Polytype 8H at Room Temperature	70
18	Raman Spectrum of PbI_2 Polytype 8H at 50 K	71

FIGURE NO.		PAGE
19	Phonon Dispersion Curves from Raman (12H) Measurements	74
20	Raman Spectrum of PbI_2 Polytype 12H at Room Temperature	75
21	Raman Spectrum of PbI_2 Polytype 12H at 50 K	76
22	Phonon Dispersion Curves from Raman (12R) Measurements	79
23	Raman Spectrum of PbI_2 Polytype 12R at Room Temperature	80
24	Raman Spectrum of PbI_2 Polytype 12R at 50 K	81
25	Transverse Acoustical Dispersion Curve Along c-Direction of PbI_2	85
26	Optical Dispersion Curves Along c-Direction of PbI_2	87
27	Heat Capacity of PbI_2	92
28	Comparison of Heat Capacities of PbI_2 and MgO on a Normalized Scale	95
29	Sample Decay Curve of Heat Capacity Measurements in PbI_2	97
30	Thermal Conductivity of PbI_2	103
31	Mean Free Path of PbI_2	104
32	Mean Free Path of PbI_2	105
33	Lattice Parameter of PbI_2 in c-Direction as a Function of Temperature	109
34	Lattice Parameter of PbI_2 in a-Direction as a Function of Temperature	110
35	Interlayer Force Constants for PbI_2	112
36	Compressional Rigid Layer Normal Modes of PbI_2	113
37	Calculated Dispersion Curves of PbI_2 (Acoustic)	118
38	Calculated Dispersion Curves for PbI_2 (Optical)	119

LIST OF TABLES

TABLE NO.		PAGE
1	Experimental Conditions for Gel Growth	10
2	Yield of Polytypes from Heat Treatment of 2H Crystals	30
3	Assignment of Raman Lines in Figures 8 and 9 PbI_2-2H	51
4	Frequencies of Raman Lines from the Literature PbI_2-2H	52
5	Correlation Diagram for Modes of 2H and 4H PbI_2	54
6	Assignment of Raman Lines in Figures 10 and 11 PbI_2-4H	57
7	Frequencies of Raman Lines from the Literature PbI_2-4H	58
8	Correlation Diagram for Modes of 2H and 6H PbI_2	62
9	Assignment of Raman Lines in Figures 14 and 15 PbI_2-6H	66
10	Assignment of Raman Lines in Figures 17 and 18 PbI_2-8H	72
11	Assignment of Raman Lines in Figures 20 and 21 PbI_2-12H	77
12	Assignment of Raman Lines in Figures 23 and 24 PbI_2-12R	82
13	Measured Heat Capacities at Low Temperatures	91
14	Measured Thermal Conductivities at Low Temperatures	101
15	Lattice Parameters of PbI_2 (2H)	108
16	Calculated Force Constants	117
17	Comparison of Force Constant Ratios in Selected Layer Crystals	121
18	Comparison of Force Constants Calculated by "Anderson" Model	122

TABLE NO.		PAGE
19	Comparison of Calculated Davydov Splittings	125

LIST OF SYMBOLS

SYMBOL	MEANING
a	Lattice Parameter
a_1, a_2	Coefficients in Heat Capacity Expansion
A	Area
A_o	Amplitude in Thermal Conductivity
A_1, A_2, A_3	Amplitudes in Force Constant Model
α_a, α_c	Expansivities
β, β_n	Roots of Tan Equation
B	Volume Expansivity
c, c_o	Lattice parameter, at T=0
c'	Lattice Distance
C_v, C_p, C_p', C	Heat Capacities (volume, pressure, stress)
C_{11}, C_{13}, ...	Elastic Constants
d	Thermal Diffusivity
f	Frequency in Hz
g	Anharmonic Force Constant (term in energy expansion)
γ_a, γ_c	Gruneisen Constants
h	Planck's Constant
H, K, L	Millar Indices
κ	Thermal Conductivity
K_B	Boltzmann Constant
K_o, K_2, K_1	
K_o^c, K_1^s, ...	Force Constants (compressional, shear)
k	Harmonic term in Displacement Energy Expansion

SYMBOL	MEANING
ℓ	Length of Crystal
ℓ_m	Mean Free Path
M, m	Masses
n, n'	Indices
N	Number of Atoms
N_A	Avogadro's Number
Θ_o^c	Debye Temperature (T=0)
P	Pressure
ρ	Density
π	Pi (3.14.....)
q	Momentum
r	Parameter in Thermal Conductivity Calculation
R	Gas Constant
S_{11}, S_{13}, ...	Compliances
T, T', T_o	Temperatures
t	Time
U	Energy
u	Frequency in cm^{-1}
v, v_l, v_t, v_{av}, v_{av}^c	Wave (sound) Velocities
V	Volume
V_A	Molar Volume
w	Angular Frequency (rad/s)
X	Bulk Compressibility
Z_o, Z_{-1}, ...	Vibrational Displacements

CHAPTER 1

INTRODUCTION

Many crystals display extreme anisotropy and form layer-type structures in which bonding between layers is much weaker than that within a layer. In some examples, bonding of the atoms in a layer may be covalent while the bonding of the layers may be largely of the van der Waals type. The anisotropy has consequences on the physical properties of the crystals. For example, there will be marked weakening or softening of vibrational modes in the crystallographic c-direction. This is shown in the phonon dispersion curves where the longitudinal acoustic branch is much lower in energy perpendicular to the layers.[1]

For layer-type structures, some thermodynamic properties, such as the thermal expansion, would obviously be expected to display anisotropy.[2] In other properties, such as the heat capacity, that are related to the whole vibrational spectrum, it will be difficult to detect effects of anisotropy except under particular circumstances. For instance, 2-dimensional effects have been found in the heat capacity of graphite at low temperatures.[3]

In this thesis, we are concerned with lead iodide (PbI_2) which forms layer-like structures but of a less extreme form than the structure of graphite. PbI_2 was chosen

because of its relative ease of preparation and because it shows another property exhibited by some layered crystals; polytypism. We wished to use various physical properties of PbI_2 as a means of studying the vibrational structure of a system in which the size of the unit cell could be varied in a controlled manner.

Because of the relative weakness of the interlayer interaction, layered crystals can be thought of in terms of planes being stacked in the c-direction. There are, in general, three possible positions for each layer (as in the hexagonal close packed and face centered cubic structures for the packing of spheres). Since there is little restriction on the order of packing, unit cells of almost any repeat distance can be formed in the c-direction. A well-known example is silicon carbide which is discussed in detail in reference 4. The number of space groups available to layered structures is limited ($P\bar{3}m1$, $P\bar{3}m1$, $P\bar{6}m2$, $P6_3mc$, $P6_3/mmc$, $R\bar{3}m$, $R\bar{3}m$, and $F\bar{4}3m$ (ref. 4 pg. 159)) but the stacking order is almost unlimited. A separate type of notation is thus desirable to describe the situation. Several types exist,[4] but some give more detail than is necessary. One of the simpler types, the Ramsdell notation,[5] is used throughout this thesis. It consists of a number/letter combination (such as 6H or 12R) in which the number refers to the repeat distance along the c-direction. In PbI_2, however, a layer consists of a plane of lead atoms sandwiched

between two planes of iodine atoms. The notation refers to the sequence of iodine atoms in PbI_2 and so a "6H" polytype contains three complete layers. The letter refers to the Bravais lattice that results from the stacking arrangement. The only lattices possible, in general, are cubic (C), hexagonal or trigonal (H), and rhombohedral (R). In PbI_2, the cubic arrangement is not observed.

This notation does not distinguish between types of the same Bravais lattice and repeat distance but of different stacking order. It is thus ideal when such information is not known or, as here, is not needed.

PbI_2 is known to form many different polytypes through the technique of gel growth.[6] However, it is not a straightforward matter to produce a specific polytype because this experimental method nearly always yields a distribution of different polytypes. Also, the polytype 2H is by far the most common one formed. Other methods, which have been of some success, are Bridgman growth from a melt [7] and thermal annealing of samples.[8] All of these methods have been used to prepare crystals for the studies to be described in this thesis. Each crystal studied has been identified by X-ray diffraction.

The higher polytypes are of particular value in allowing Raman and infrared data to be used to obtain elements of the vibrational structure of layered crystals that are not ordinarily accessible to study through this method. Only

the q=0 portion of the dispersion curve is usually available. In polytypic substances, however, the various polytypes can be considered to share the same dispersion curves. The effect of the larger cell is then to fold back the dispersion curves in the c-direction, thus making more modes accessible to the Raman and infrared techniques (at q=0). This method has been used extensively in the study of the vibrational structure of SiC.[9,10,11,12]

Much of the prior work on PbI_2 has been concerned with its band structure, semiconducting properties, and exciton spectrum.[13,14,15,16,17,18,19] Less has been done on the vibrational properties. Raman measurements have been made on 2H and 4H polytypes and some infrared data obtained for 2H.[20,21,22,23,7] Inelastic neutron scattering experiments have been performed on a large crystal (probably 2H) at room temperature [24] and the results used to delineate portions of dispersion curves in particular crystallographic directions. Information about velocities of sound at room temperature have been obtained from measurements of the Brillouin spectrum.[25]

The experiments to be described in this thesis provide the following new information: Raman spectra of polytypes 2H, 4H, 6H, 8H, 12H and 12R at temperatures T=50 K and 400 K; thermal expansion for T>100 K; heat capacity and thermal conductivity of a bulk 2H crystal for the region $0.5<T<4$ K. The details are given in Chapters 2 and 3. In

Chapter 4, the new experimental results are correlated with existing information in terms of a relatively simple force constant model.[26] The 2-dimensional character of the vibrational spectrum turns out to be relatively small despite the fact that PbI_2 forms structures that are clearly strongly layer-like.

CHAPTER 2

EXPERIMENTAL

2.1 Preparation/Identification of Polytypes

2.1.1 The Technique of Crystal Growth in Gels

Interest in crystal growth in a gel medium goes back to the turn of the century to the study of the phenomenon of Liesegang Rings. Liesegang [27] had added silver nitrate to gelatin containing potassium chromate. Concentric rings of silver chromate were precipitated in the form of microcrystallites. Larger crystals were occasionally seen and the technique of crystal growth in gels gradually evolved even though the Liesegang Ring phenomenon is not well understood even today. [28]

In the last decade, there has been considerable interest in gel-grown crystals. A need for single crystal specimens in solid state science has led to the exploitation of all available techniques, however exotic they might be.

The best medium for growing crystals appears to be silica gel although other gels such as gelatin and agar have been used. The preparation of a silica hydrogel involves the mixing of a solution of sodium metasilicate and water to a density of 1.04 to 1.08 g/cm^3 (or a commercial waterglass adjusted to that density) with an equal volume of about one molar acid solution. The resultant mixture will

gel in a time (between seconds and days) that depends mainly on the density and acidity.

After the gel is formed another solution can be placed on top and its components will slowly diffuse in. If one of the components of the desired reaction is mixed with the gel and the other put in the supernatant solution, the crystals will nucleate and grow in the medium as the components diffuse through.

Alternatively, a system can be set up using a gel bridge (e.g. a U-tube) where both components are allowed to diffuse into the gel from opposite directions.

A good review of gel-growth can be found in "Crystal Growth in Gels" by H. K. Henisch.[29]

2.1.2 Preparation of Crystals of PbI_2

The basic procedure required to prepare PbI_2 crystals is to mix a small amount of one molar lead acetate solution with the gel and to place one molar potassium iodide solution on top. Hexagonal lead iodide platelets and dendrites form in the gel over a period of a few weeks.

H. K. Henisch [6,29,30] seems to have been the most successful in growing PbI_2 crystals of various polytypic structure. In his thorough investigation [6] he examined the dependence of polytypes formed, on concentrations of reactants, and on temperature. He concluded that a lower concentration of KI favoured the formation of high polytypes. He did not

observe any temperature dependance of polytypism in the region of room temperature to 83°C.

Henisch also noted [6] the prevalence of syntactic coalescence in lead iodide especially of 2H with higher polytypes. After polytype 2H, the most common ones found were 12H and 12R. Also found were 4H, 6H, 14H, 16H, 18H, 18R, and 24R but not 8H although its identification is stated to be somewhat uncertain.

2.1.3 Experimental Conditions Studied

When sodium metasilicate is mixed with acetic acid to form a gel, the pH of this mixture determines the time required for gel formation. A solution of pH ≈ 8 to 10 gels very quickly, in a few seconds or minutes, depending upon the density. Higher density ($\sim$ 1.1 g/cm^3) solutions gel more quickly, but the resulting gel is too stiff. On the other hand, too low a density ($\sim$ 1.02 g/cm^3) produces a gel that is too weak. Thus, in the preparations to be described, solutions of intermediate density (1.04 to 1.08 g/cm^3) were used. It is desirable to adjust the pH so that the gels form in a couple of days. This has the advantage that there is time for particulate impurities to settle out. For pH greater than 7, there is the possibility of lead hydroxy-iodide being formed [31] and thus the gel was always adjusted to be acidic. A pH of 5 was found to give the required gelling time of a couple of days.

The gels were contained in sealed test tubes that were normally suspended in a constant temperature water bath. Table 1 summarizes various experimental conditions that were tried and that produced usable PbI_2 crystals.

In experiments 1 to 5, the effect of KI concentration was examined following Henisch et al [6] (see pictures in Figure 1). In experiment 6, the test tube was not thermostatted and the result was a much higher degree of nucleation (see Figure 1) presumably because of temperature fluctuations. The object of experiments 7 to 9 was to examine a reported effect of silver impurities on polytypic growth in PbI_2.[8,32]

The possible effect of light was explored by allowing gel and crystal formation in experiments 10 to 12 to take place in the dark.

Experiments were tried using gels that were less dense than 1.04 g/cm^3 but no crystals were formed. The gel would not be dense enough to support the potassium iodide solution or diffusion would be too rapid to produce more than powdery crystals.

2.1.4 Identification of Polytypes with X-rays

A Buerger precession camera and molybdenum radiation were used in the identification of the various polytypes in lead iodide. The hexagonal platelets were easily aligned visually so as to give an X-ray photograph of the 0,K,L

TABLE 1

EXPERIMENTAL CONDITIONS FOR GEL GROWTH

reparation #	Na_2SiO_3 density (g/cm^3)	Solution Volume (cm^3)	Volume of 2M Acetic Acid Sol. (cm^3)	Volume of 1M lead Acetate Sol. (cm^3)	Resultant pH	KI solution Molarity	KI solution Volume (cm^3)	Ambient Temperature (°C)	Time for Gel to Set (days)	Time for Crystal Growth (days)
1	1.048	40	40	16	5	2	54	43	2	8
2	"	"	"	"	"	1	"	"	"	"
3	"	"	"	"	"	0.5	"	"	"	"
4	"	"	"	"	"	0.35	"	"	"	"
5	"	"	"	"	"	0.25	"	"	"	"
6	1.079	60	60	24	5.5	0.75	80	21	2	11
7[1]	1.060	20	20	9.1	5	1	25	37	4	25
8[2]	"	"	"	"	"	"	"	"	"	42
9[3]	"	"	"	"	"	"	"	"	"	"
10	1.047	"	"	8	4.5	0.4	48	50.7	3	13
11	"	"	"	"	"	0.6	"	"	"	"
12	"	"	"	"	"	0.8	"	"	"	"

1 Gel also contained 0.9 cm^3 of 0.01 M silver acetate.

2 " " " " " " 0.001 M " "

3 " " " " " " 0.0001 M " "

FIGURE 1

GEL GROWTH PREPARATIONS

(a) Test Tubes in Thermostated Water Bath

(b) Beaker in Open Air

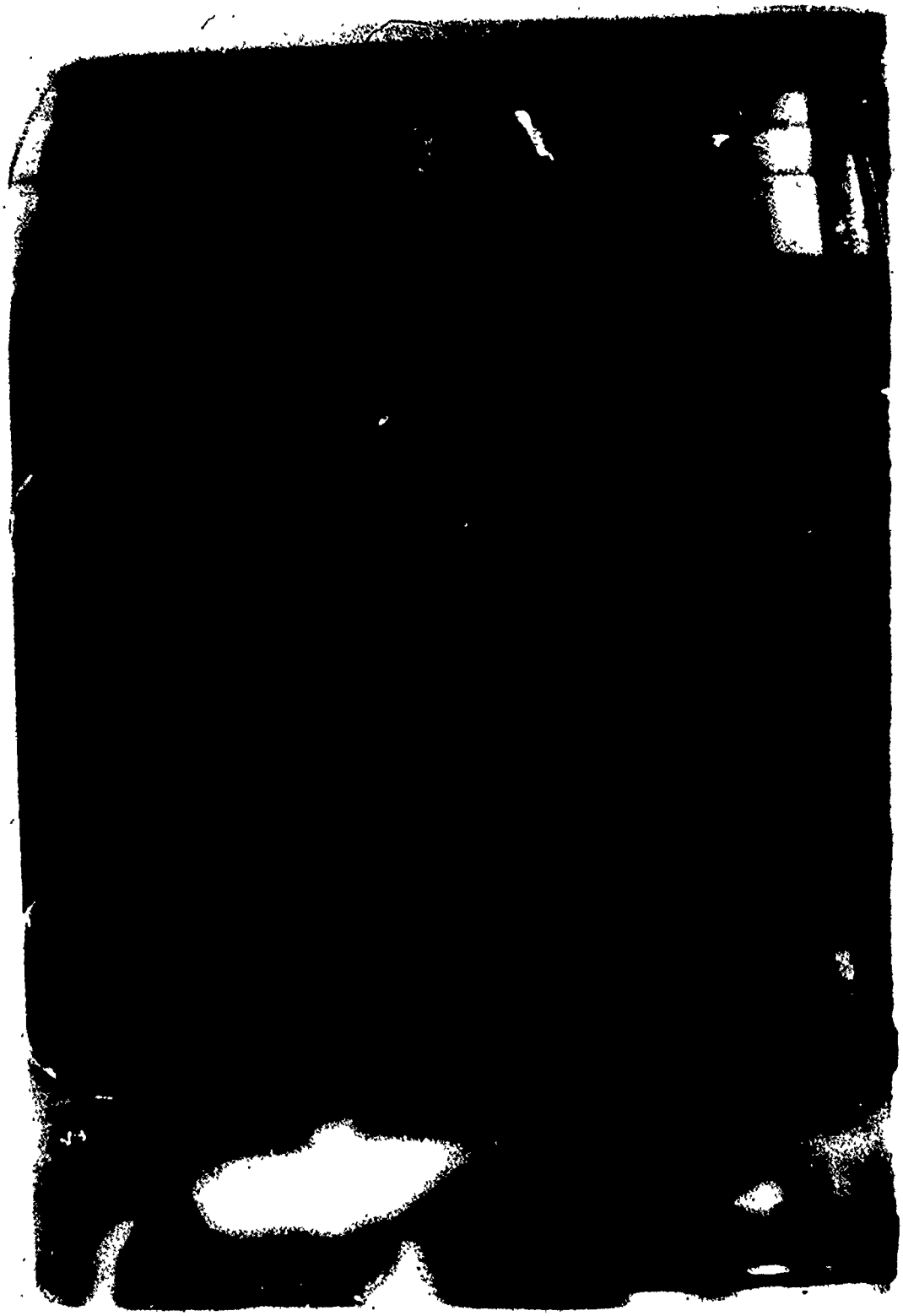

(a)

(b)

reciprocal plane.

Since all polytypes are built up from the same 2H layer, the photographs of the 0,K,L plane superimpose over the 2H reflections (Figure 2). This makes the identification of various polytypes reasonably straightforward. It should be noted that in the PbI_2 structure, all polytypes have the extinction

H,K,L for H+K = 3n (n = 0,1,2 ...)

and L ≠ n'n/2 (n' = order of polytype, i.e. 4 in 4H). This means, for hexagonal polytypes, it is simply a matter of counting the reflections which appear between the 2H reflections. For this case along 0,1,L; 0,2,L; 0,$\bar{1}$,L and 0,$\bar{2}$,L directions are best.

For the rhombohedral polytypes account must be taken of the R-centering extinctions; -H+K+L ≠ 3n. For the 0,K,L plane examined here, K+L ≠ 3n. By comparing adjacent lines (say 0,1,L and 0,2,L) this extinction can be easily seen. Thus one can distinguish between polytypes 2H and 6R, 4H and 12R and so on.

The toughest structures to identify are coalesced combinations of 4H and 12R. Rhombohedral structures, and therefore extinctions, can occur in an obverse or a reverse direction (Figure 2) depending on crystal orientation. In fact, both the obverse and reverse orientations can exist in the same crystal. Therefore great care must be taken in separating the various combinations of 12R-obverse, 12R-reverse and 4H (see Figure 2). Notice that the 12R (obverse) + 12R (reverse) + 4H appear the same as 12H in the X-ray

FIGURE 2

X-RAY PHOTOGRAPHS OF 0KL RECIPROCAL PLANE

(c-axis is vertical)

(a) 2H

(b) 4H

(c) 6H

(d) 8H

(e) 12H

(f) 12R-obverse

(g) 12R-reverse

(h) 12R-obverse + 4H

(i) 12R-reverse + 4H

(j) 12R-obverse + 12R-reverse

(k) 12R-obverse + 12R-reverse + 4H

(c)

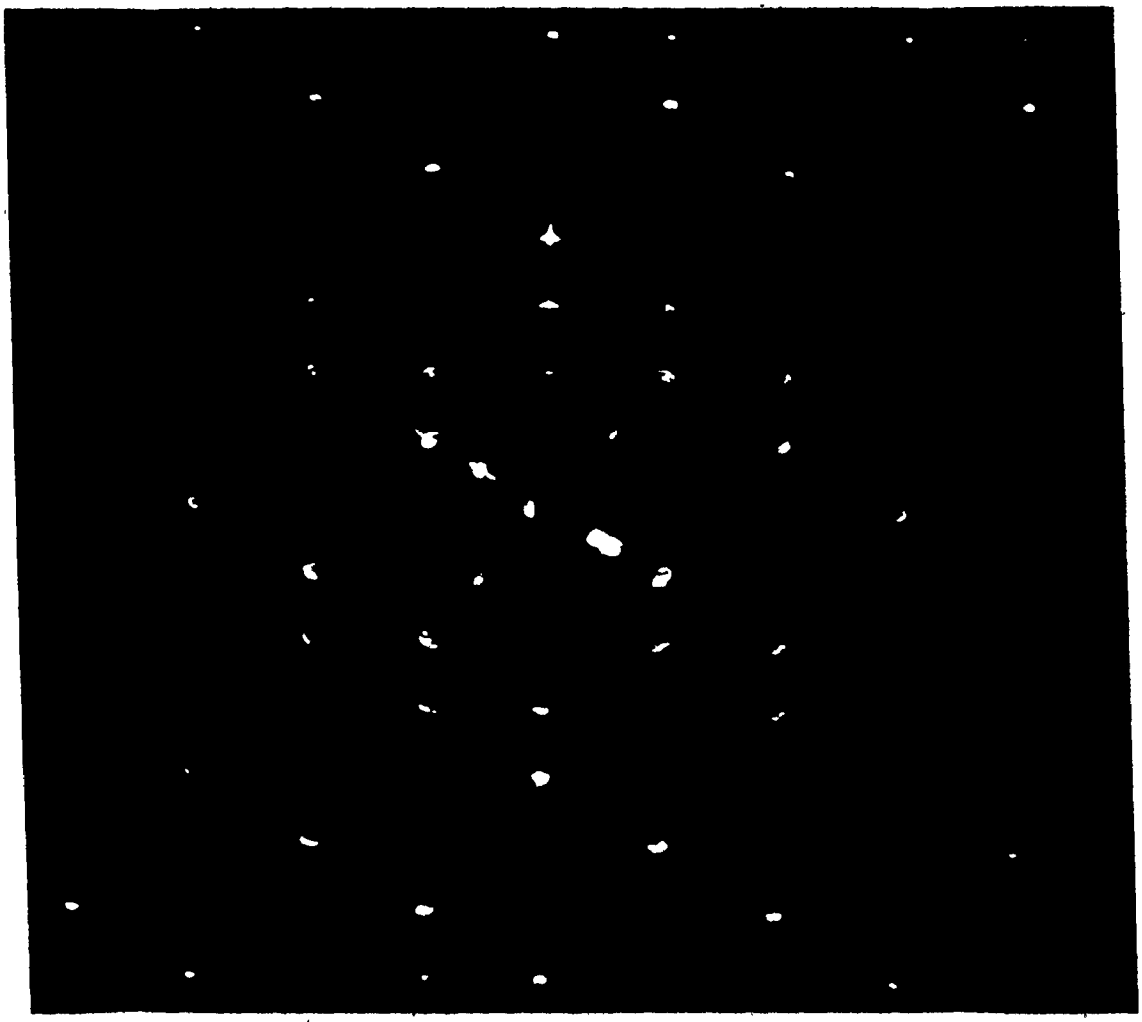

(b)

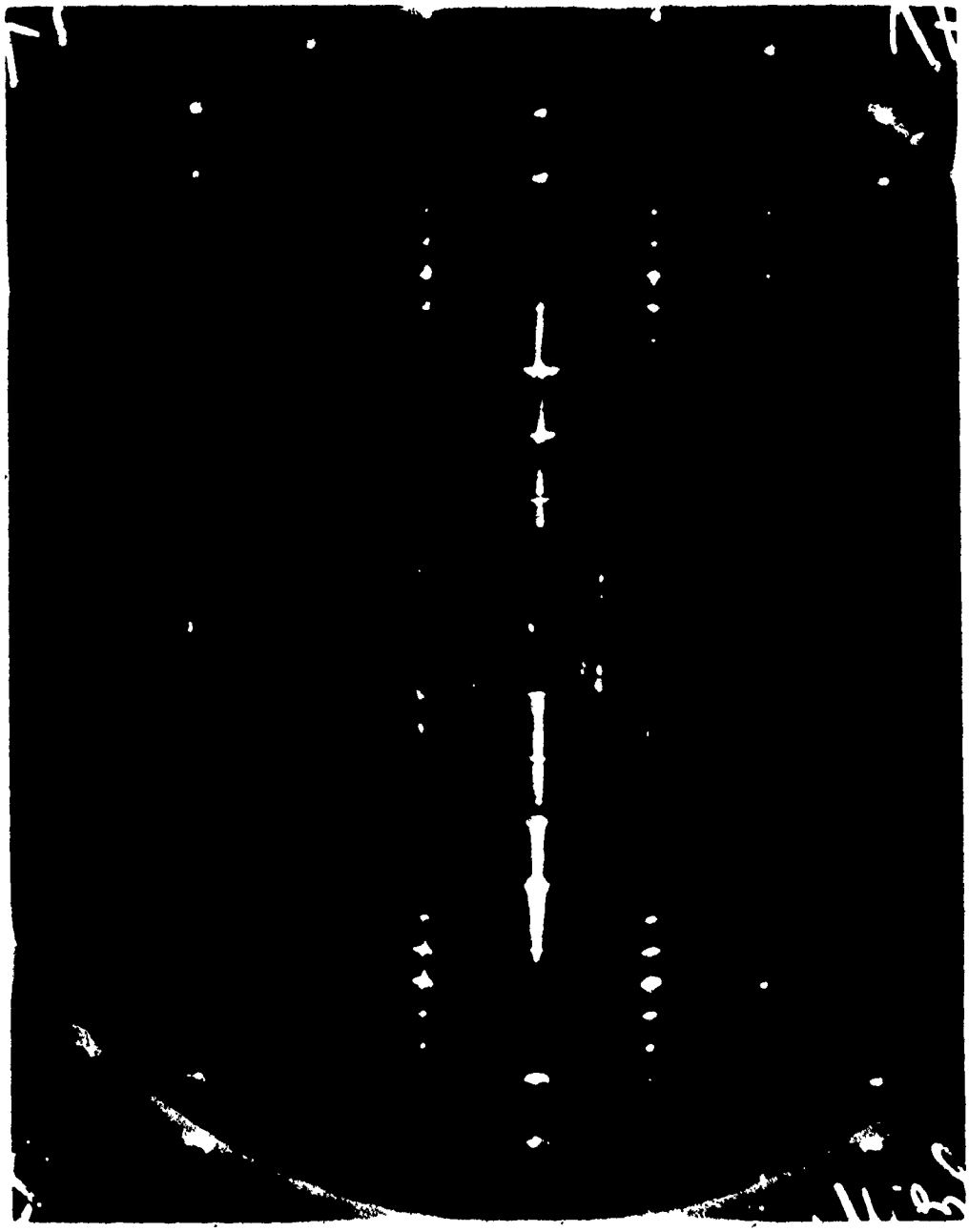

(c)

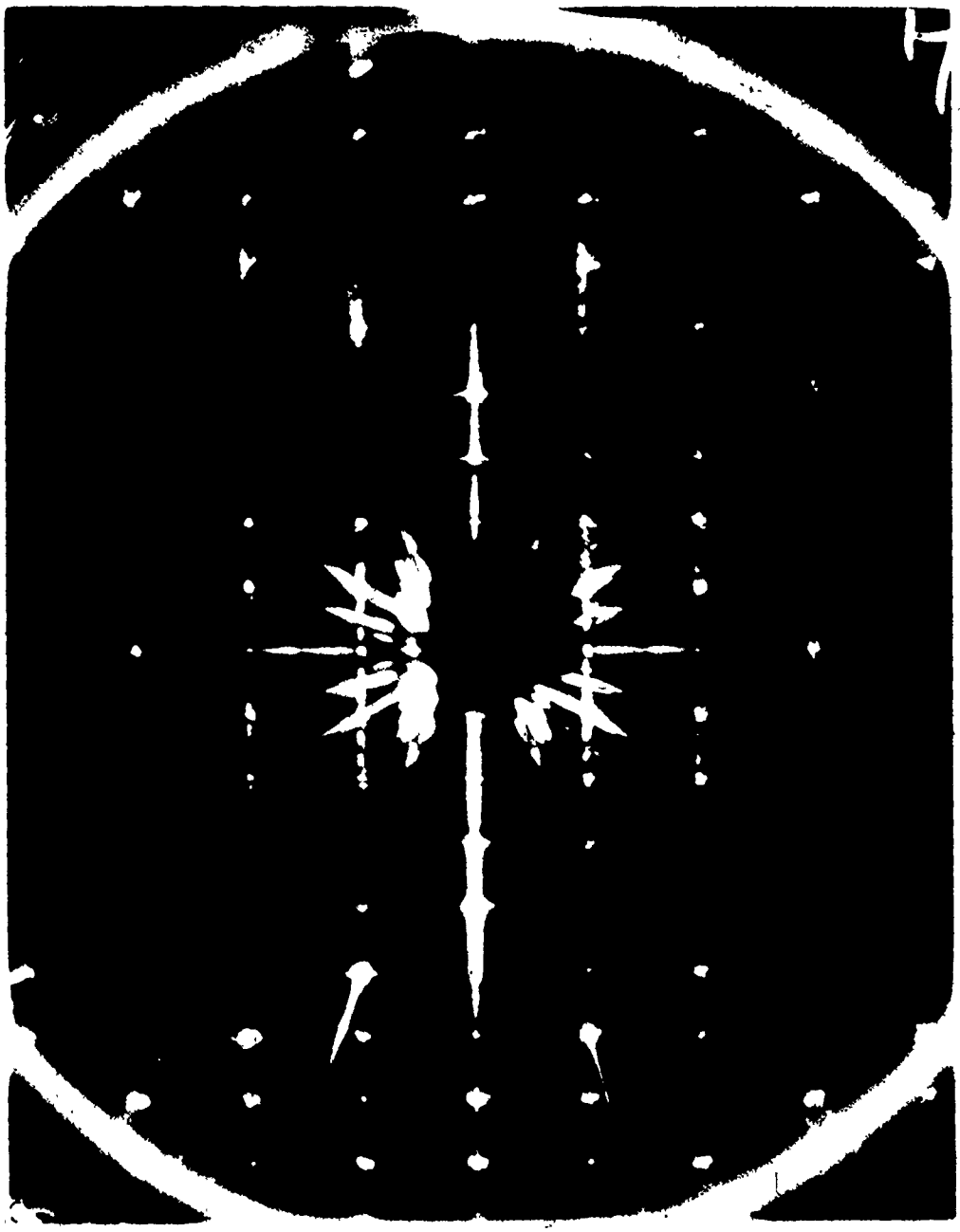

(d)

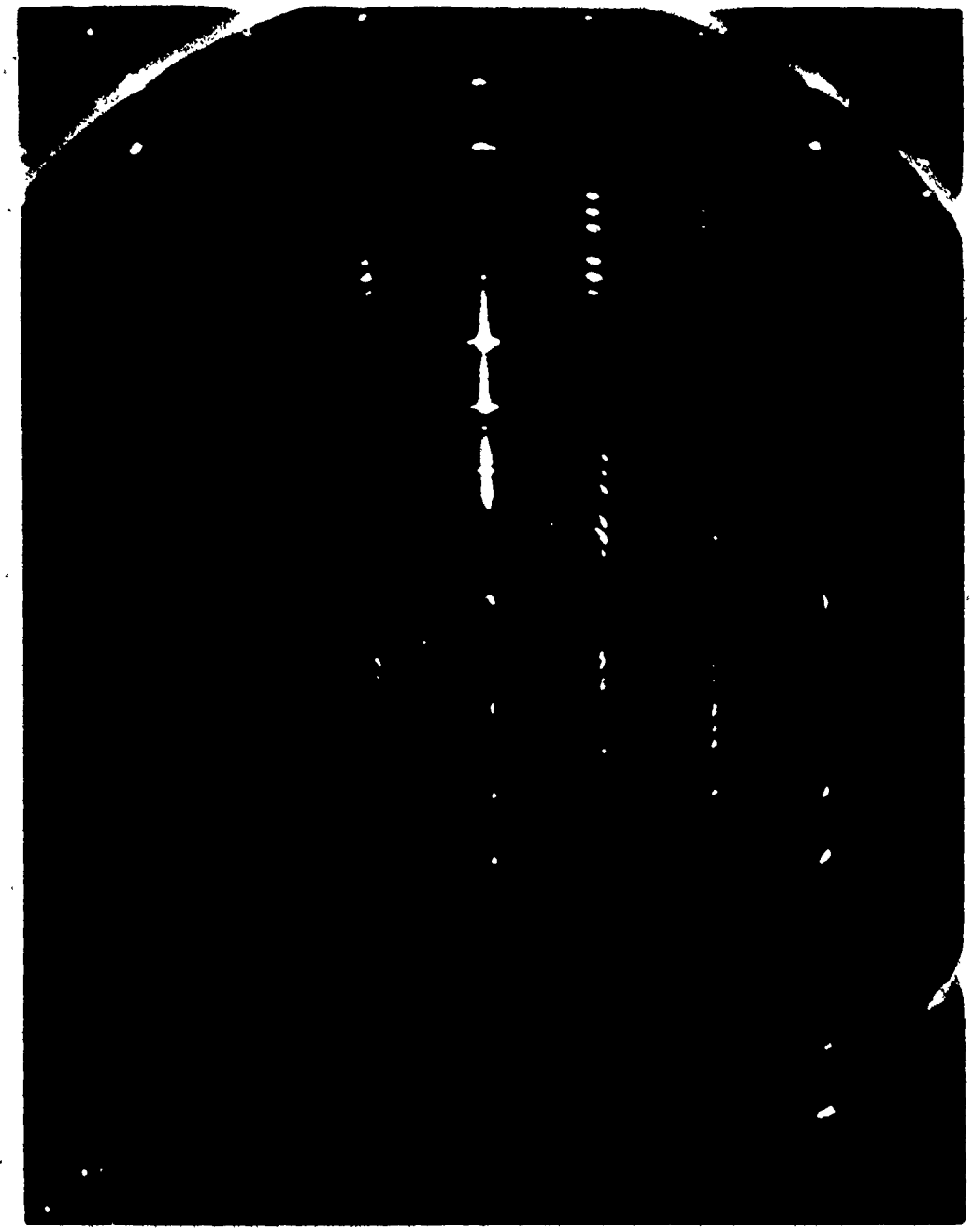

(e)

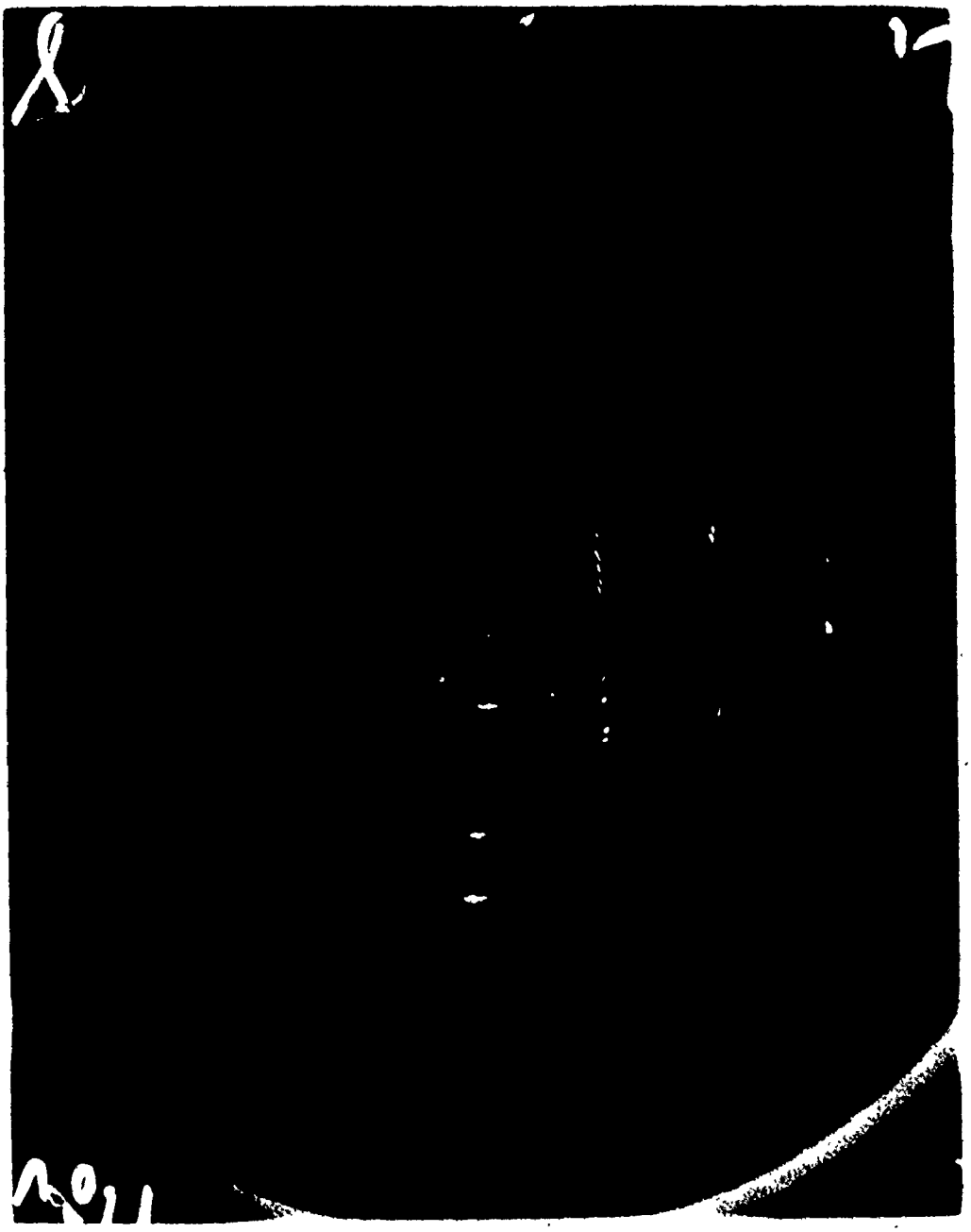

(f)

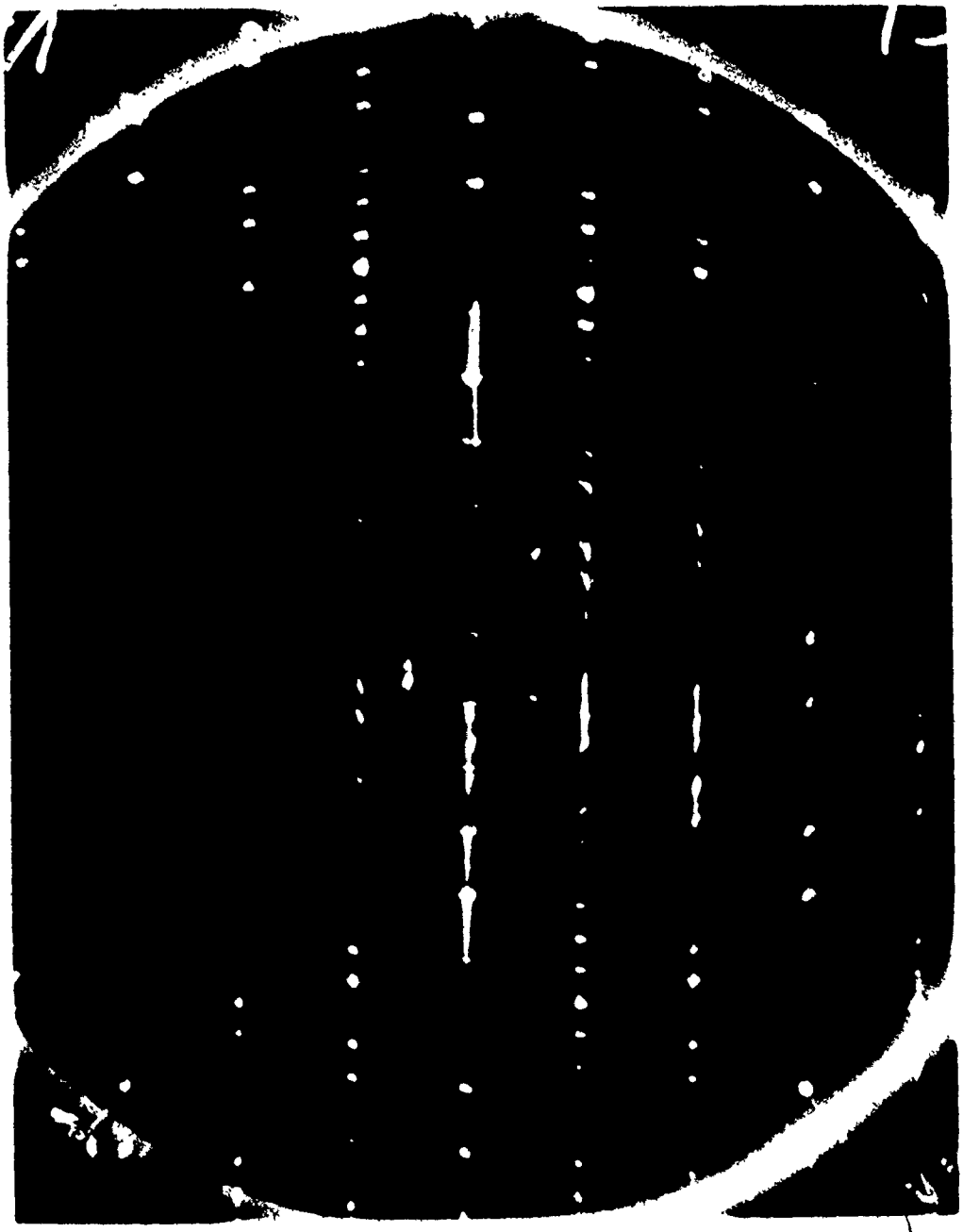

(g)

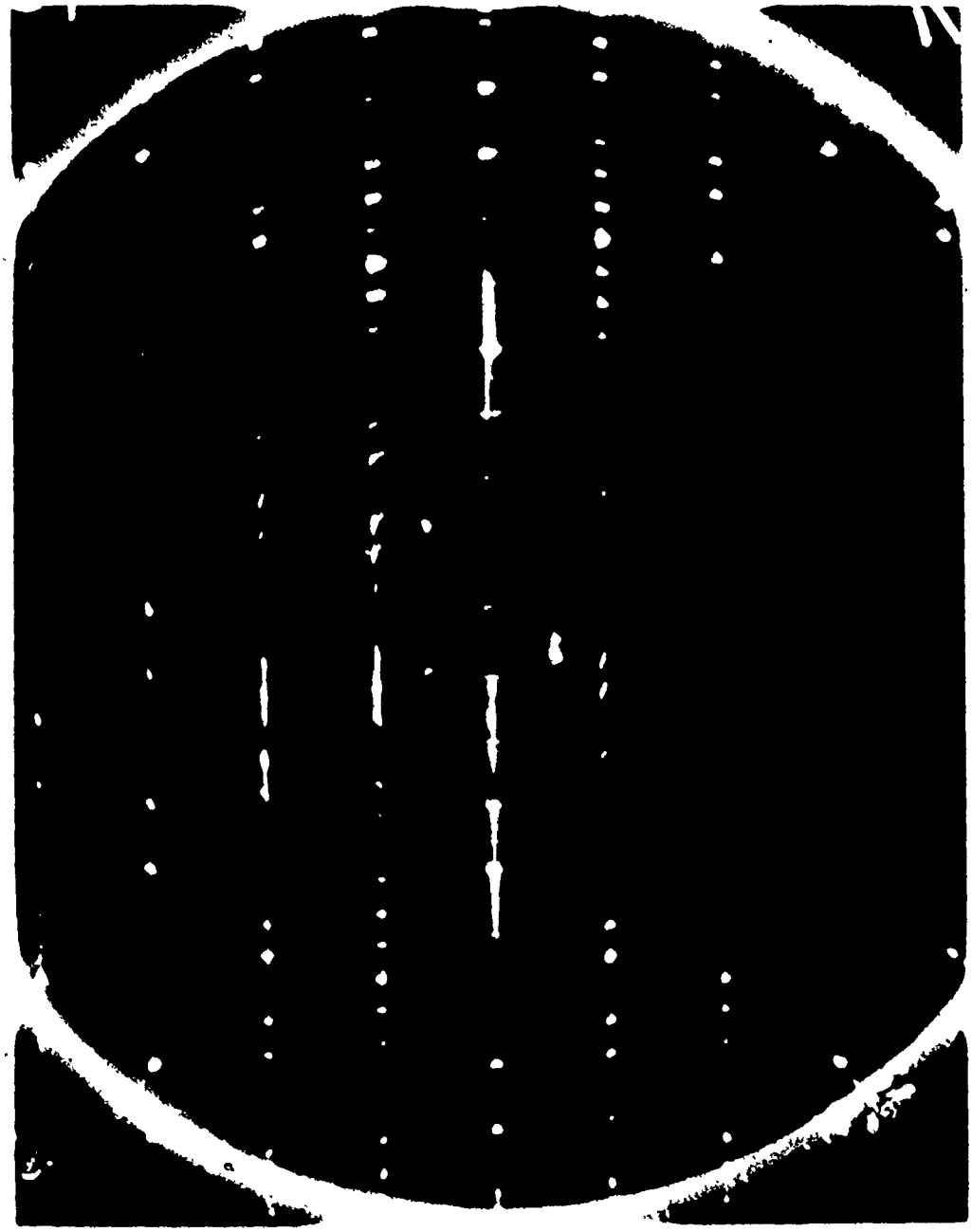

(h)

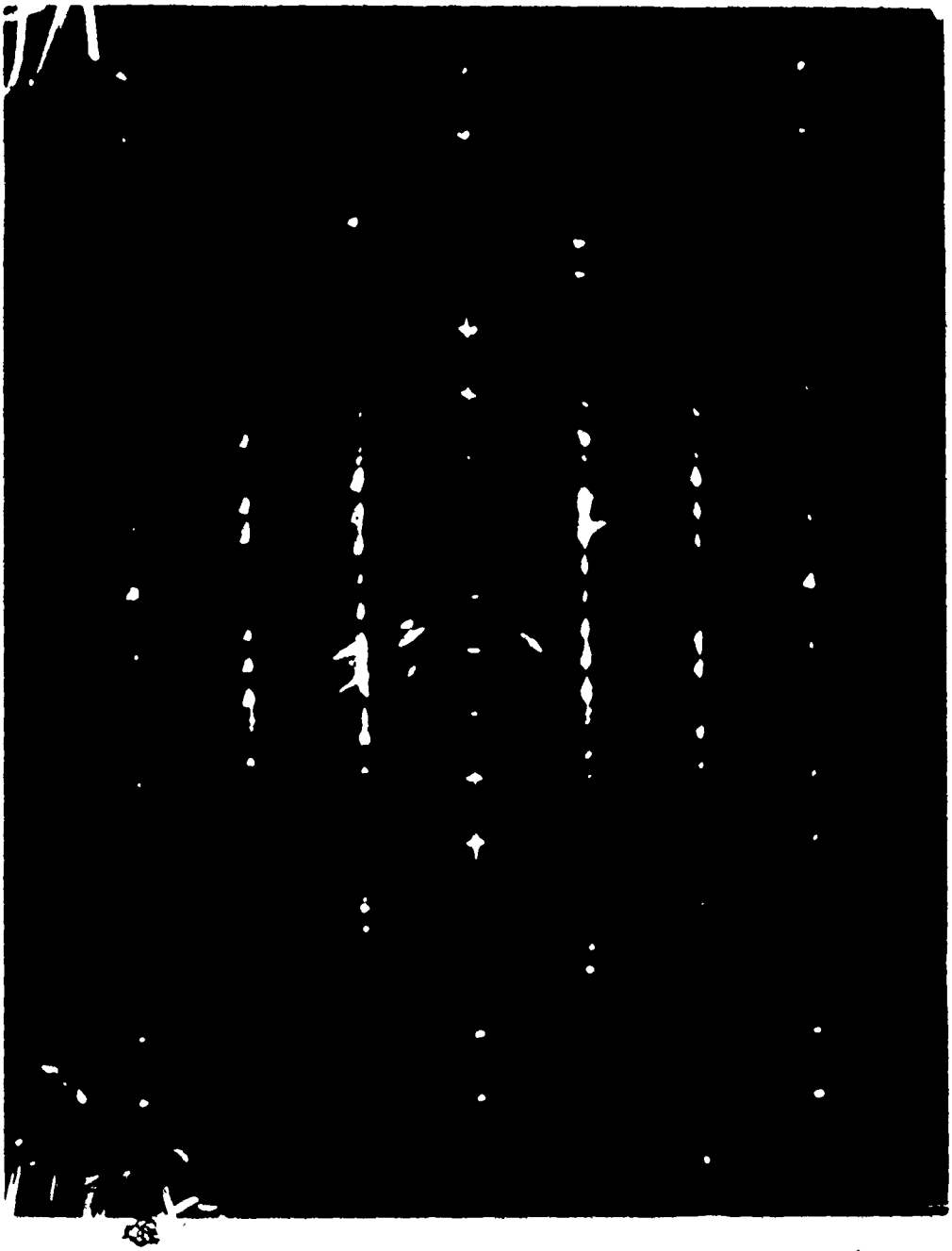

(i)

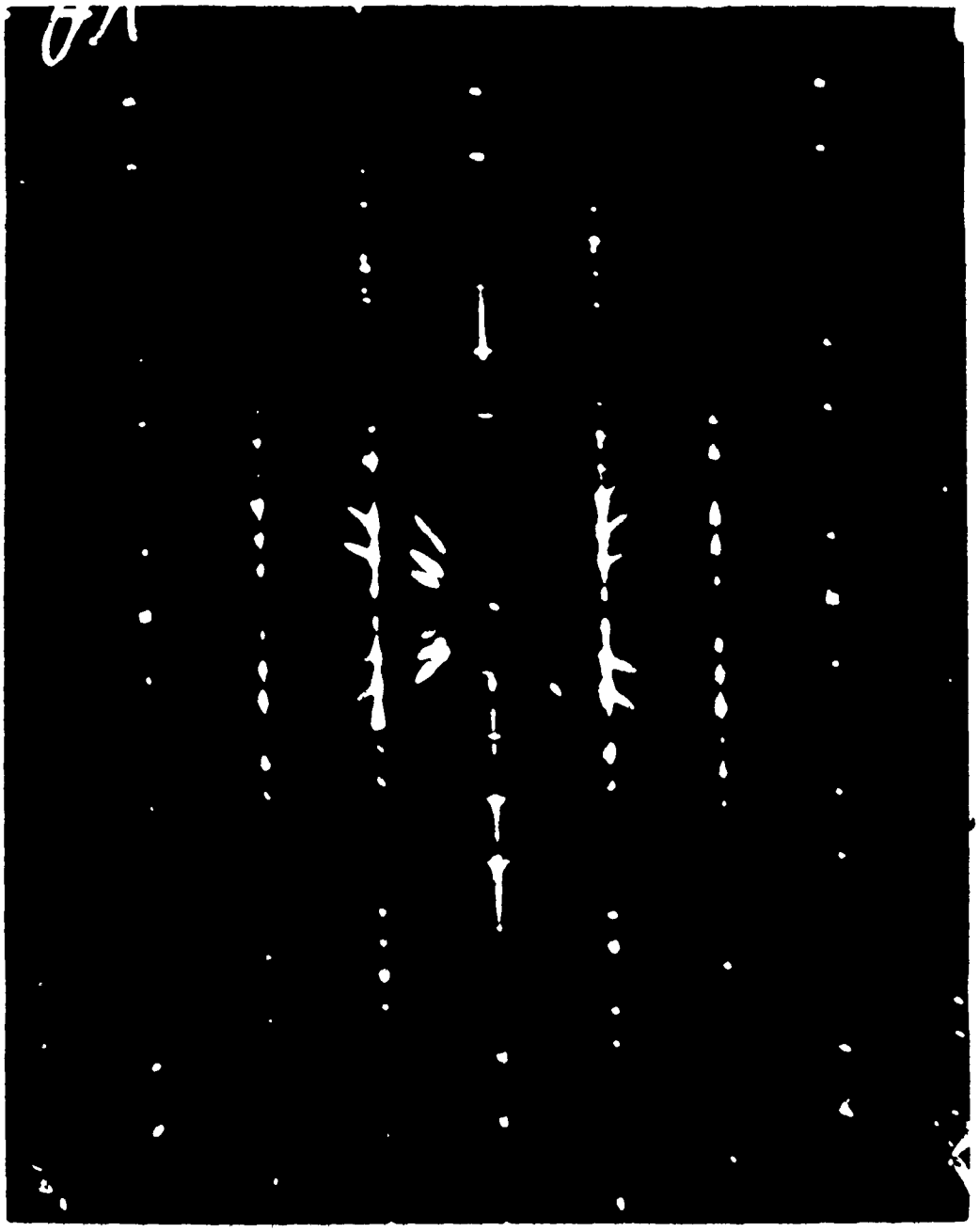

(j)

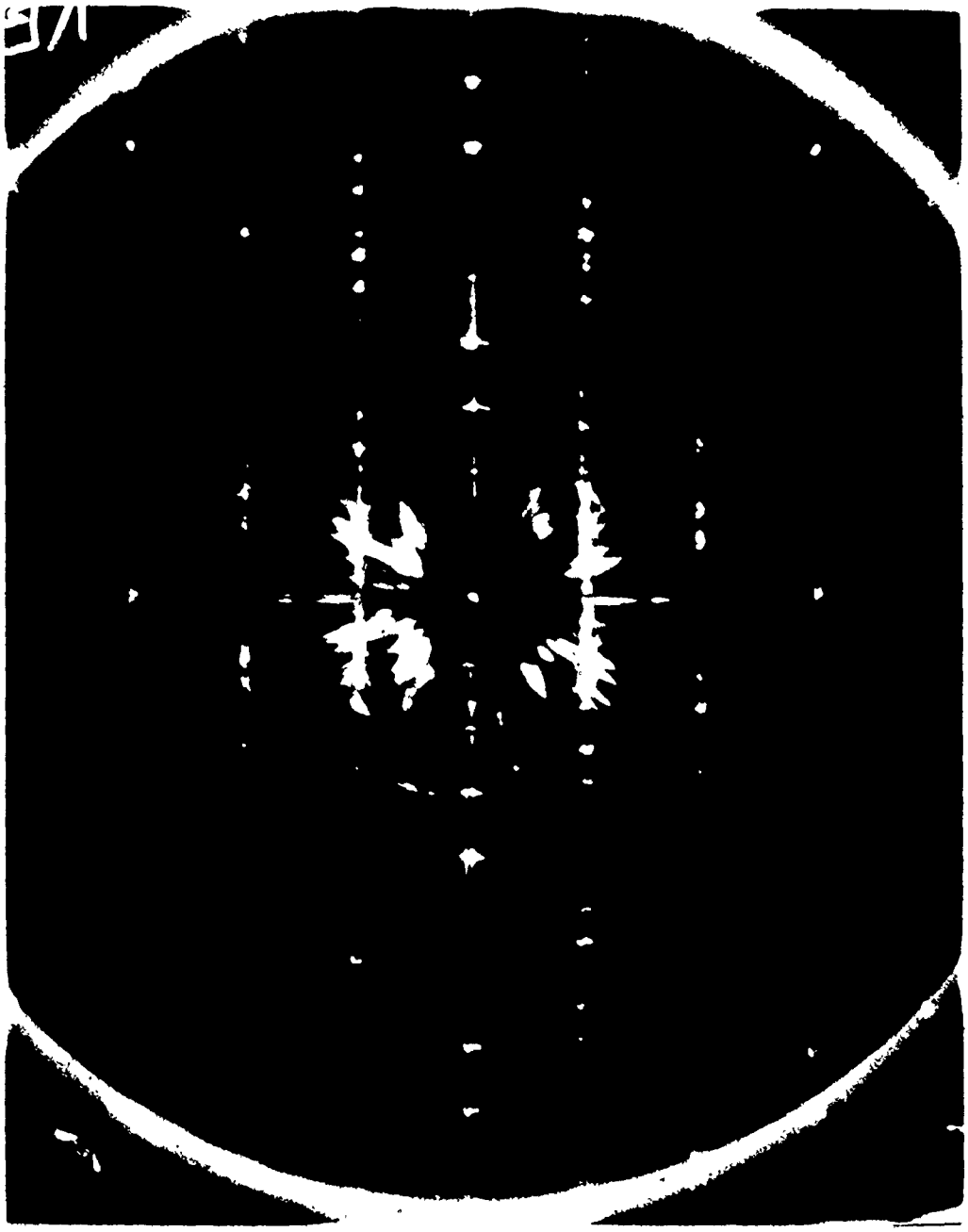

(k)

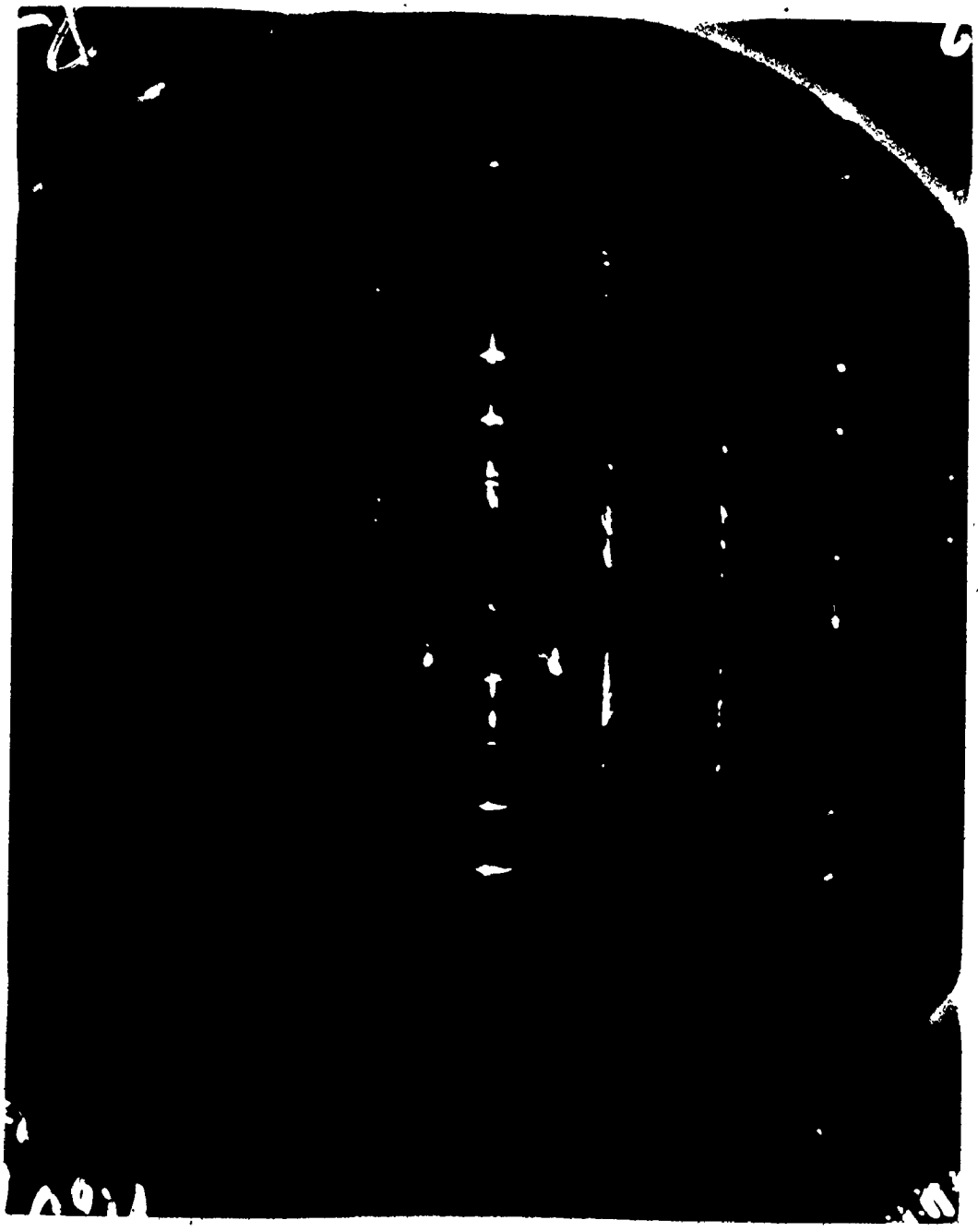

photograph. Of course, not all reflections are of the same intensity as they must reflect the detailed structure of the crystal. Also, the higher polytypes can have more than one structure. These structural differences do not effect the experiments in this thesis and they will thus be ignored. In connection with this it should be noted that the Raman experiments can distinguish between 12H and 12R (obverse) + 12R (reverse) + 4H.

2.1.5 Results of Gel-Growth Experiments

The yield of higher polytypes was smaller than that reported by Henisch [6] but similar to that found by others.[33, 34, 35] Of 89 crystals that were examined, 7 turned out to be other than pure 2H. A reason given [8, 32, 34] for the higher yield found by Henisch is the strategic presence of silver impurities in the lead acetate that he used. Three experiments were performed in which silver acetate was purposely added but no polytypes other than 2H were found in the crystals grown. It is possibly significant [6, 29] that Henisch's gel-growth was performed in the dark. As mentioned in a preceding section, three experiments were done with the gel-growth test tubes placed in continual darkness. There was a slight improvement in the yield of higher polytypes. Silver acetate is sensitive to light and perhaps a combination of the two conditions is required.

Non-2H PbI_2 crystals are seldom, if ever, composed

of a single polytype. The 7 crystals concerned were: 6H with 2H, 12H with 2H, 12R with 12H and 2H from preparation 10; 8H with 16H from preparation 12; 8H with 4H from preparation 1; 12H with 2H from preparation 5 and also one from preparation 6.

2.1.6 Preparation of Polytypes by Thermal Treatment of 2H Crystals

A more productive method of obtaining certain polytypes turned out to be to heat 2H crystals that had been prepared by gel-growth. The crystals were heated in an evacuated ($P < 1 \times 10^{-4}$ torr) glass tube at various temperatures and for various times as is summarized in Table 2.

Only 4H, 12R and mixtures of the two were formed by this method. The data suggests a 2H to 4H or 12R phase transition at about 170 °C. This has been observed by others.[8,20,34,35] Also suggested by the data is a 4H to 12R transition at 270 °C.[8]

Prasad [34] has reported to have seen a 2H to 8H transition which was not observed here.

Minagawa [35] suggests that these high temperature forms, especially 12R, are metastable and tend to revert back to 2H at room temperature. However, this could take from months to years.

The last entry in the table refers to heating PbI_2

powder as received from a chemical supplier. The resulting mixed 4H-12R specimen was ill-formed and had a coating of impurities on its surface; it was therefore not suitable for further investigation. However, see Section 2.3.1 for further information in this regard.

One 2H crystal, not listed in the table that received an excess of laser radiation during a Raman experiment was found to have transformed into a mixed 4H-12R polytype.

TABLE 2

YIELD OF POLYTYPES FROM HEAT TREATMENT OF 2H CRYSTALS

Temperature (°C)	Time (hr)	Number of Crystals	Yield of Polytypes			
			2H	4H	12R	4H/12R
130	1.5	6	6	-	-	-
170	1	6	-	3[1]	3[1]	-
210	2	4	-	2	-	2
250	42	2	-	1	-	1
270	2	4	-	-	1	3
280	21	3	-	-	3	-
300	1	1	-	-	1	-
300	44	1	-	-	-	1

1 still partially 2H.

2.2 Determination of Raman Spectra

2.2.1 The Spectrometer and Laser

A Coderg PHO laser Raman spectrometer was used for the experiments on lead iodide. It has double Ebert Fastie gratings that cover the wavelength range 4000 to 9000 Å. The accuracy and reproducibility are stated to be $\pm$ 1 cm^{-1}. The output from a photomultiplier and DC amplifier was fed into a recorder which was coupled to the frequency scan of the gratings (linear in wave number (cm^{-1})).

The crystals were mounted on a goniometer head that could be attached to a room temperature single crystal mount on the transfer plate of the spectrometer. The transfer plate transfers the laser beam to the crystal and the scattered light into the main lens of the spectrometer.

For the low temperature experiments, the goniometer head was mounted in a liquid He^4 optical cryostat which could be suspended over the transfer plate.

A Spectra-Physics krypton ion laser (model 164-01) was used with the Coderg spectrometer. It emits at a number of frequencies through the visible spectrum. The most useful radiation is the 6471 Å line which has a power in excess of 0.5 watts at maximum current and lies well above the absorption edge in lead iodide.

Because of the many plasma lines which also appear in the output of the laser, a diffraction grating was usually

used to filter the light before it entered the transfer plate of the Coderg.[36] This caused an 80% reduction in the power of the laser beam for the 6471 Å line, but at high current the power remaining was much more than was actually needed.

2.2.2 Spectrometer Accuracy

The precision of a recorded frequency is determined by the scanning speed of the gratings and by the linearity of the frequency response of this scan. The linearity of the tracking of the gratings is specified as ± 0.1%. The scanning speed and resolution (slit width) were adjusted for optimum response.

The stated accuracy of the spectrometer is ± 1 cm^{-1} but in practice Raman lines could often be determined to better than this. The agreement observed between the present results (to be described in the next Chapter) and some published Raman spectra for PbI_2 lie within this 1 cm^{-1} tolerance.

Difficulties were encountered in determining the zero of the spectrometer (i.e. the position of the Rayleigh peak). For example, in successive scans of a spectrum, the center of the Rayleigh peak could shift by as much as 1 cm^{-1}. It was therefore important to record both the Stokes and anti-Stokes components so that this shift could be cancelled out. This would not prevent the effect of slippage occurring in the scan from anti-Stokes to Stokes. It is not clear

whether this, in fact, occurred in a few of the experiments.

This shifting of the Rayleigh peak caused the most trouble at low temperatures and for low frequency shifts because of the obscuring effect of the Rayleigh tail and because the anti-Stokes peaks lose most of their intensity at low temperatures.

2.2.3 Polarization Experiments

The output of the krypton laser is polarized in the vertical direction by the Brewster windows used in the plasma tube. The sense of polarization could be rotated by means of a double prism mounted on the front of the laser. The Coderg contained slots for the insertion of analysers and by this means, both vertical and horizontal polarizations could be observed. Quarter wave plates were also used to eliminate the grating bias to polarization direction.

It was not possible to polish the PbI_2 crystals because they were so fragile. Moreover, the crystals tended to display appreciable internal scattering. On these accounts, the polarization measurements were not always as successful as desired.

2.2.4 Low Temperature Cryostat

For measurements at low temperatures, the PbI_2 crystals were mounted in the cryostat that is shown in Figure 3. Cooling was achieved by continuous transfer of

FIGURE 3

LOW TEMPERATURE He^4 CRYOSTAT FOR RAMAN SCATTERING

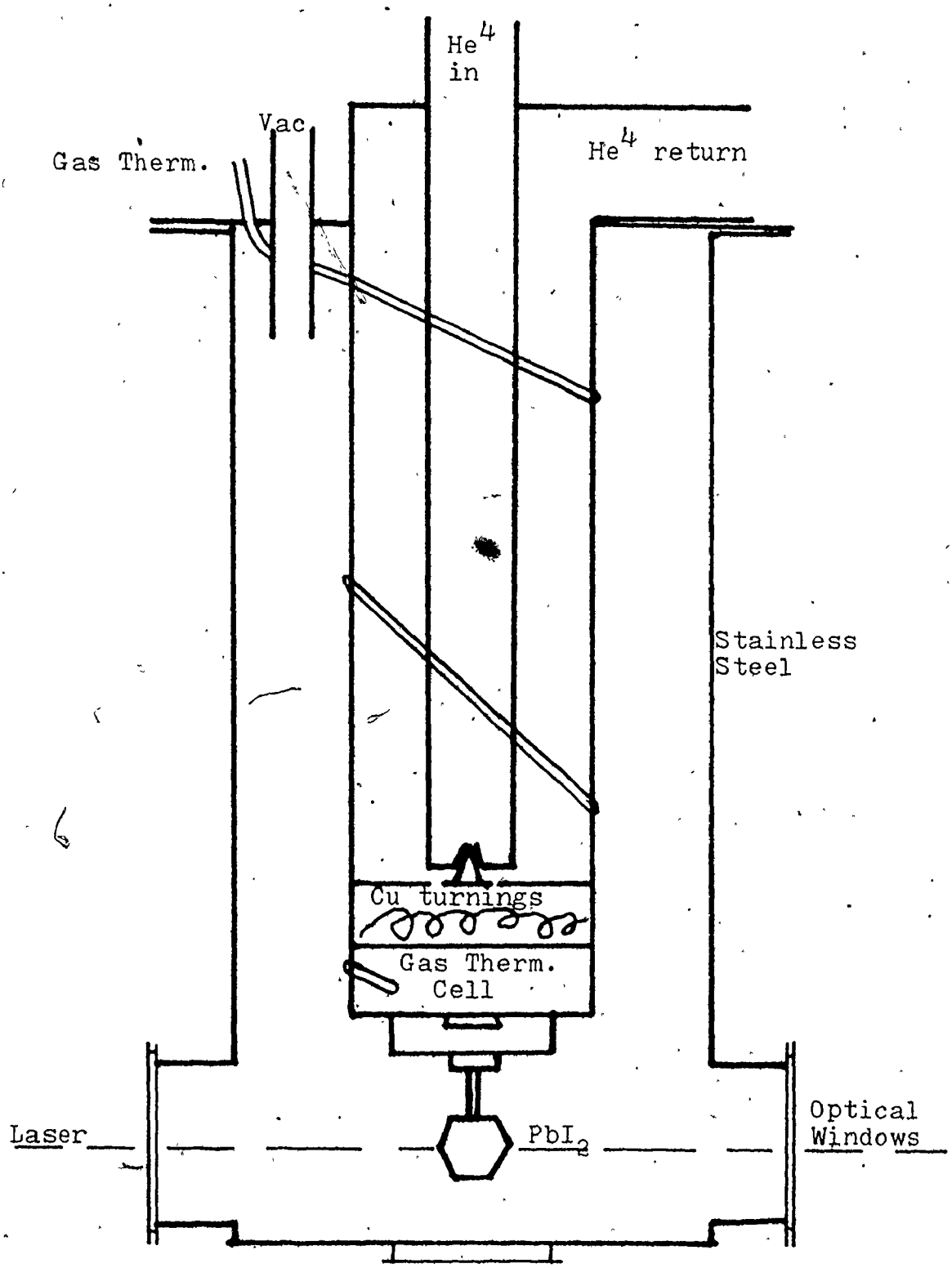

liquid helium to the cryostat. The temperature of the crystal mount was monitored by the attached gas thermometer which was able to achieve liquid helium temperatures (4.2 K).

The temperature of the PbI_2 crystal itself was determined by the Raman effect, that is the ratio of the Stokes to anti-Stokes Raman peaks. Because of the amount of blackbody radiation passing through the optical windows and the heating by the laser beam, the lowest temperature obtained for the crystal was invariably about 50 K.

Consumption of liquid helium was rather high ($\sim$ 15 liters/hour) on the same account.

2.3 Heat Capacity Measurements

2.3.1 Preparation of Crystal Specimen

For the heat capacity measurements on lead iodide, a large crystal was needed. It was found that a suitable crystal could be grown by the Bridgman technique.

Reagent grade (98.5%) lead iodide powder was placed in a glass tube which was evacuated ($P < 1 \times 10^{-4}$ torr) and then the lead iodide was melted to drive out any trapped gas. After the tube was sealed under vacuum, it was slowly lowered through a furance (Figure 4) set at a temperature just above the melting point of lead iodide, about 400°C.

The rate of lowering was controlled with a low speed motor and was such that the crystal grew over a period of four days. When it was removed from the tube, the crystal was found to have an "impurity" layer on top. This part of the crystal was cut off, the remainder was resealed in a glass tube and the melting and growth processes were repeated. The regrown crystal did not have an impurity layer on its top surface.

A spectrographic analysis was made of small samples scraped from the crystal and it showed the presence of only a few parts per million of Ag and Sn. The crystal was thus judged to be suitable for the calorimetric measurements.

One end of the crystal was cut with a diamond saw which gave the surface a smooth enough finish for mounting on the calorimeter tray (see following section). The cut

FIGURE 4

BRIDGMAN GROWTH OF PbI_2

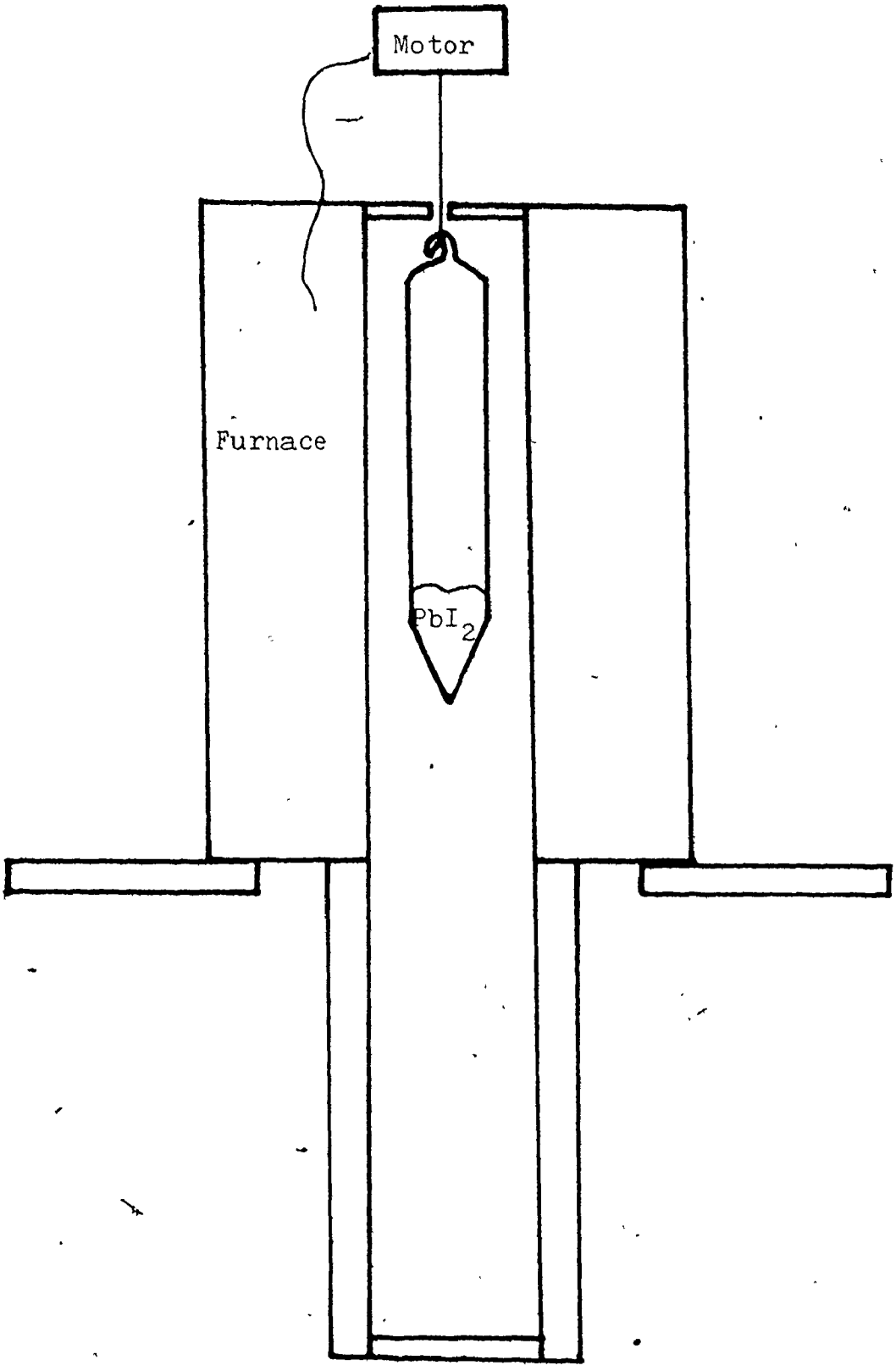

was made perpendicular to the layers of the crystal.

The crystal contained two boundaries and hence was composed of three crystals (but of the same orientation). The mass of the crystal was 56.48 grams.

The mosaic spread of the crystal could not be determined as only X-rays were available for that purpose. The penetration depth of X-rays into lead iodide is too small for a large crystal.

2.3.2 Calorimetric Technique

A tray type calorimeter was used for the measurements. The PbI_2 crystal was placed on the small copper tray as is shown in Figure 5. Good thermal contact was ensured through the addition of a measured quantity (0.01 cm^3) of silicone grease placed in the contact area between the polished surface of the crystal and the tray.

The tray was mounted in a frame suspended below the mixing chamber in a He^3-He^4 dilution refrigerator. Cooling was accomplished through closure of a heat switch, in thermal contact with the mixing chamber, that gripped a gold-plated copper spike attached to the tray.

The tray carried an electrical heater and a germanium thermometer that had been intercompared with a germanium thermometer carefully calibrated over the temperature range $0.1 < T < 4.3$ K.[37] The electrical leads between the calorimeter tray and an anchoring point on the mixing chamber

FIGURE 5

CALORIMETER

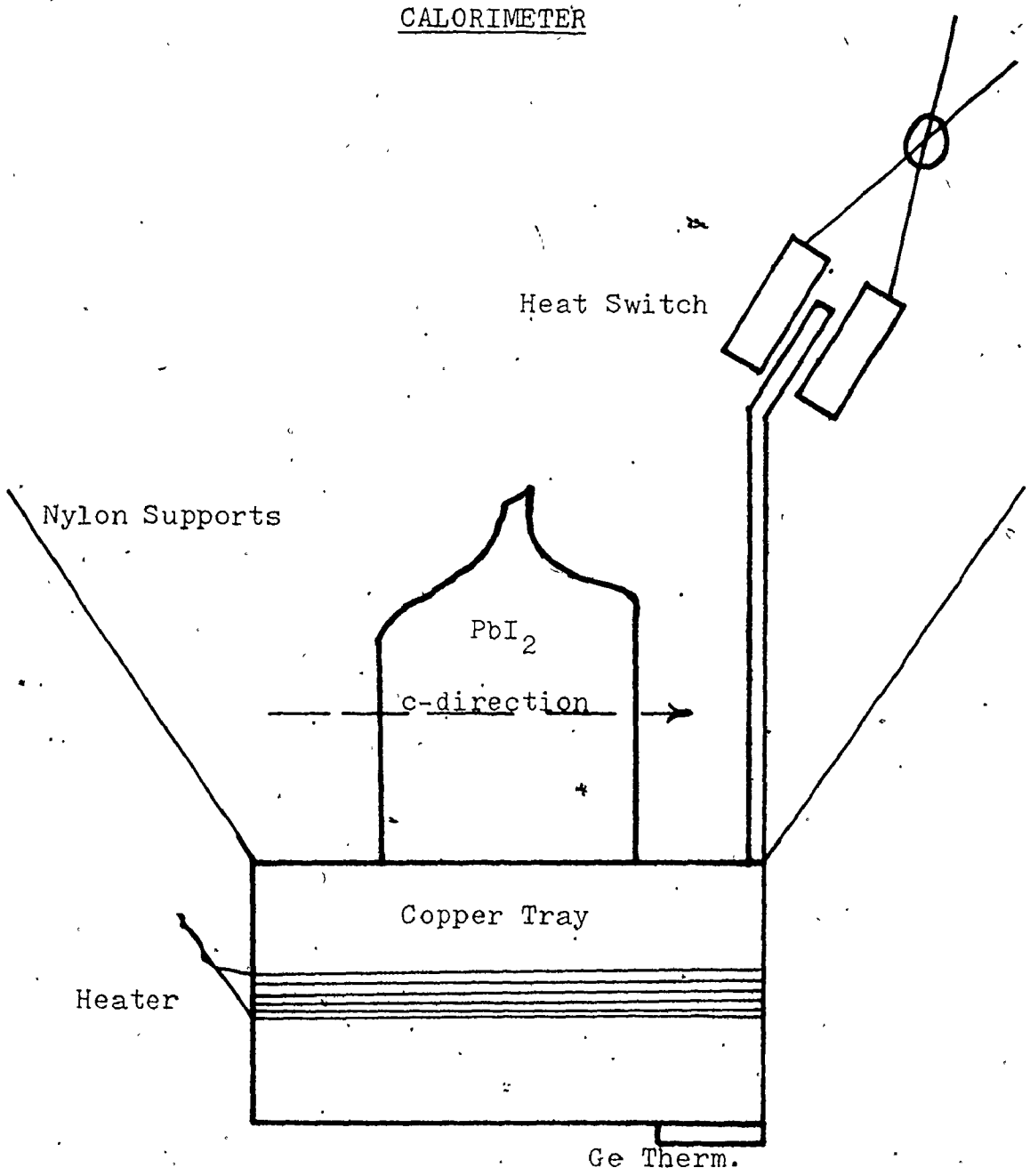

were of lead-covered manganin wire. The thin nylon filaments that held the tray within the frame were spring-loaded to damp out vibration.

The method of determining the heat capacity is depicted in Figure 6 which shows the variation of the temperature of the tray with time. The PbI_2 crystal turned out to be a surprisingly poor thermal conductor. It thus required several minutes for the energy supplied to the tray in each interval to be distributed through the crystal. Other measurements on aluminum alloys with the same tray assembly [38] showed that the thermal contact through the grease was extremely good (equilibrium time < 1 sec.).

In a separate series of measurements, the heat capacity of the tray assembly, including 0.01 cm^3 of silicone grease, was determined. From the results, a smoothed heat capacity - temperature function was constructed for computing the contribution of the tray assembly to the total heat capacity of the system.

2.3.3 Assessment of Accuracy

Measurements were performed over the temperature range $0.5 < T < 4.2$ K. In this region, the temperature scale is known with an uncertainty not exceeding several millikelvin.[37]

The tray assembly contributes 50% of the total heat capacity at 0.5 K to 3% at 3.9 K.

The principal uncertainty at the higher temperatures comes from the long extrapolation of the temperature back to the mid-point of the heating period (Figure 6).

The resulting errors are estimated to be 5% at T = 0.5 K to 2% at T = 1.5 K to 20% at T = 3.9 K.

FIGURE 6

TEMPERATURE VARIATION DURING A PULSE

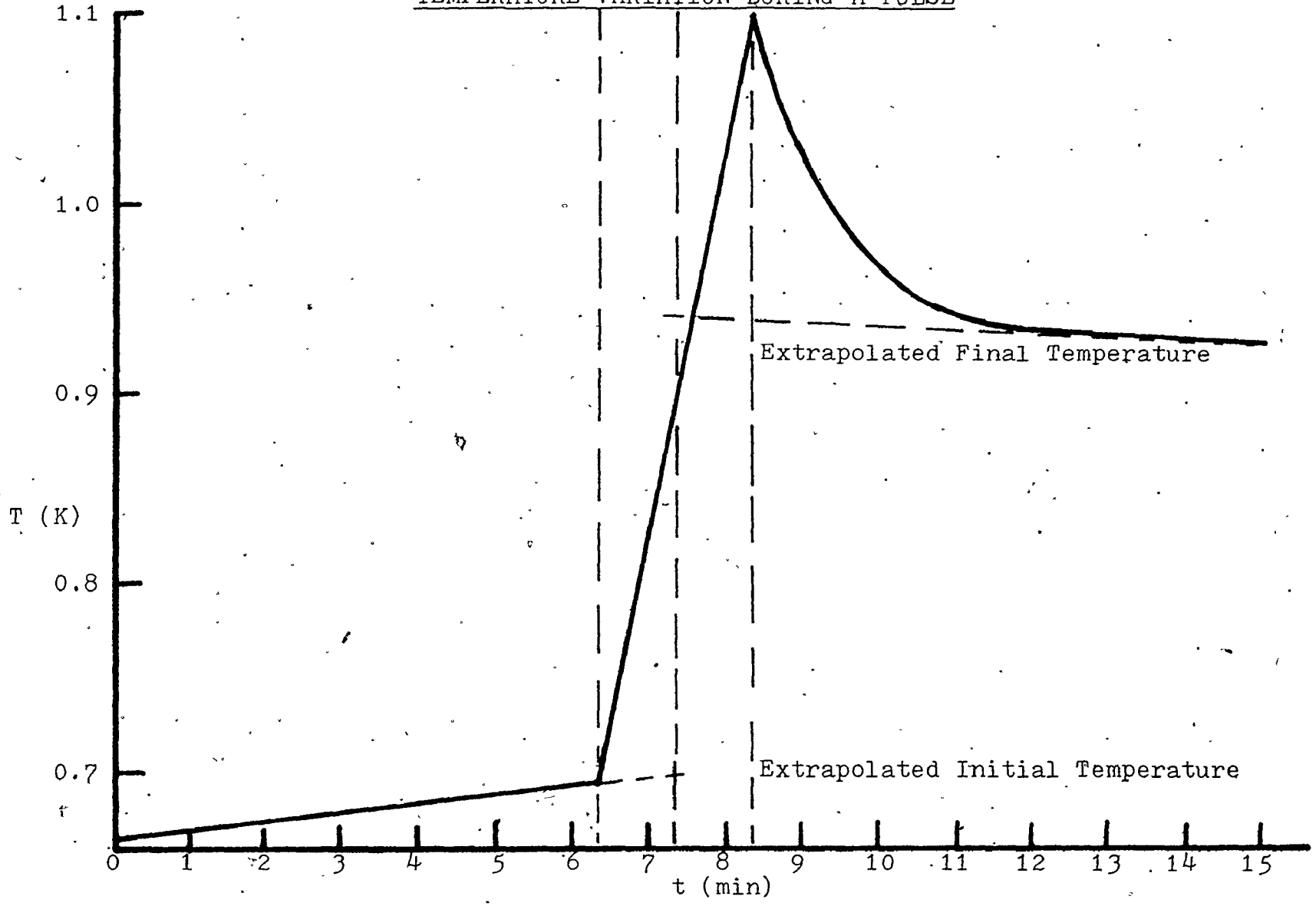

2.4 Expansivity Measurements

2.4.1 Adaptation of an X-ray Diffractometer

A Syntex $P2_1$ diffractometer was used to determine the lattice parameters as a function of temperature for a small gel-grown lead iodide crystal. The diffractometer had a low temperature attachment by means of which cold dry nitrogen gas could be impinged on the sample.

The crystal was mounted on the tip of a Chromel-Alumel thermocouple attached to a goniometer head (Figure 7). The gas was cooled by passing it through a heat exchanger immersed in a liquid nitrogen bath.

The goniometer head and the nozzle were mechanically coupled so that they remained aligned reasonably well as the triple axis arrangement moved to line up various reflections. There were, however, small changes in alignment as the system was moved and they caused slight shifts in temperature for different reflections.

With this arrangement, it was possible to cool the crystal to temperatures as low as 100 K.

2.4.2 Assessment of Accuracy

The temperature variation for a given set of data was, on the average, quite small, about 3 K. It did not, therefore, have an appreciable effect on the accuracy of the lattice parameters.

FIGURE 7

SYNTEX LOW TEMPERATURE ATTACHMENT

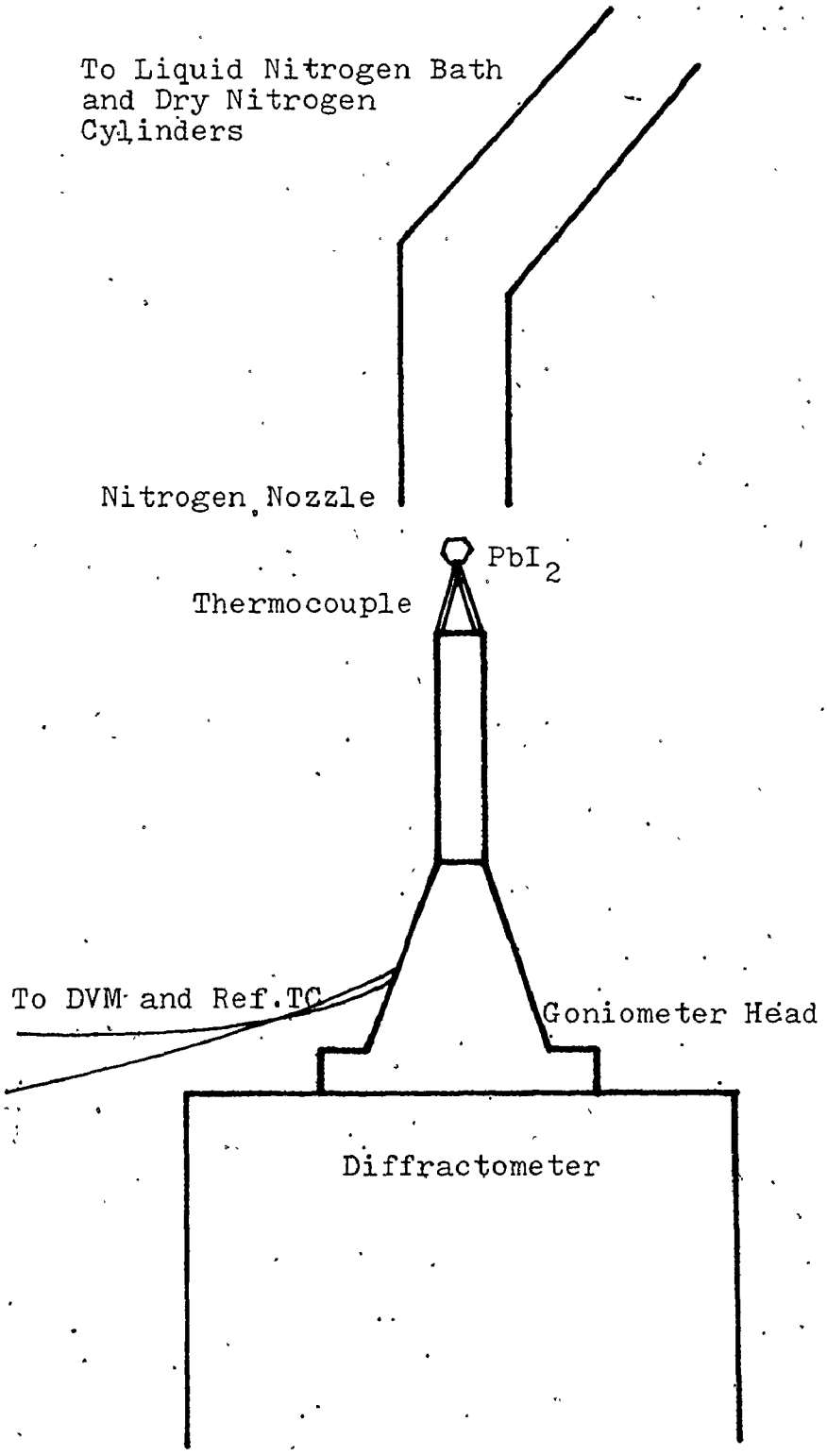

The main sources of error were the small number of reflections used (15) and the problem of centering the three axes of the diffractometer. Only fifteen reflections were used because this was the full capacity of the permanent memory of the computer attached to the diffractometer.

If the computer memory were larger, the uncertainty arising from the centering problem could be reduced. Many reflections and their geometric equivalents could be used with a significant increase in accuracy.

The data obtained from the Syntex were run through a least squares program for a hexagonal structure to obtain the lattice parameters. The absolute errors assigned to the a-parameter are $\pm$ 0.003 Å and to the c-parameter $\pm$ 0.016 Å. The temperature dependence is expected to be more accurate than this as the centering does not change from one set of measurements to another.

The details will be presented in the next chapter.

CHAPTER 3

EXPERIMENTAL RESULTS

3.1 Raman Spectra at Room and Low Temperatures

3.1.1 General View of the Raman Effect in Layered Materials

An important consideration for a layered structure is the strength of interaction between layers. If there were no interaction, the material could be thought of as 2-dimensional and there would be no cooperative modes of vibration between layers. At the other extreme with a strong interaction between layers, the crystal would be 3-dimensional with a quite ordinary vibrational spectrum. One purpose of obtaining the Raman spectra of lead iodide is therefore to measure the degree of 2-dimensionality of the crystal. We are helped in this by the fact that PbI_2, like many layered compounds, forms various polytypic structures. This brings in many more modes of vibration which would otherwise not be Raman active. The underlying assumption here is that, with the addition of more and more layers to the unit cell, there is no change (i.e. distortion of atomic positions) in the basic 2-dimensional unit. If this is the case, as it seems to be in, for example, SiC,[9,10,11,12] then all of the spectra can be related by the simple process of folding the Brillouin zone along the c-axis. This makes acoustic modes that occur in the basic 2H structure Raman active and gives

a direct indication of the strength of interlayer interaction and also, for many polytypes, an idea of the phonon dispersion along the c-axis.

In the remaining sections of this chapter, the results of the Raman experiments performed on polytypes 2H, 4H, 6H, 8H, 12H and 12R will be given. The results will be related to the 2H Brillouin zone through a straightforward application of group theory.

3.1.2 Raman Spectra of 2H-PbI_2

The polytype 2H-PbI_2 contains one molecule per unit hexagonal cell.[39] It has the space group $P\bar{3}m1$ (or in spectroscopic notation, D_{3d}^3). The lead atom has site symmetry D_{3d} and the iodines both have C_{3v}. With three atoms per unit cell, there are (by the correlation method [40]) nine vibrational modes at q=0:

$$A_{1g} + E_g + 2A_{2u} + 2E_u.$$

$A_{1g} + E_g$ are Raman active whereas one set of $A_{2u} + E_u$ is infrared active and the other is acoustical.

The doubly degenerate E_g mode can be thought of as a shear deformation parallel to the layers. The A_{1g} mode can be considered as a breathing deformation perpendicular to the layers.

Figure 8 shows a typical room temperature spectrum of a 2H-PbI_2 sample and Figure 9 the same spectrum at low temperatures (50 K). The frequencies of the observed bands

are listed in Table 3 along with the most probable assignment of modes.

The polarization measurements on the 2H sample were never sufficiently unambiguous to distinguish between the tensors given in Table 3. By comparison with the spectra of higher polytypes and the literature, however, the assignments given seem certain for E_g and A_{1g}.

The absorption edge in PbI_2 lies close to 5300 A and appears to be responsible for resonant enhancement of second order or combinational bands in the spectra.[13,23,31] Table 3 gives possible identification of these normally forbidden modes. The last two bands were only seen when the 5309 Å rather than the 6471 Å Krypton line was used. All of these modes are drastically reduced in intensity at low temperatures. Contrary to this, the E_g and A_{1g} bands become very narrow and strong at low temperature although the A_{1g} mode appears to gain in intensity at the expense of the E_g.

For comparison Table 4 gives the frequencies of Raman bands found by previous workers for crystals which were assumed to be but not actually identified as 2H. In reference 21, infrared absorption frequencies are also quoted but no spectra are given. Bands are listed at 62, 85, 100, 117 and 128 cm^{-1} but it should be noted that only two would be expected from group theory. These results do not therefore correspond well with those given in Table 3. The frequencies given in reference 22 are similar to those

FIGURE 8

RAMAN SPECTRUM OF PbI_2 POLYTYPE 2H AT ROOM TEMPERATURE

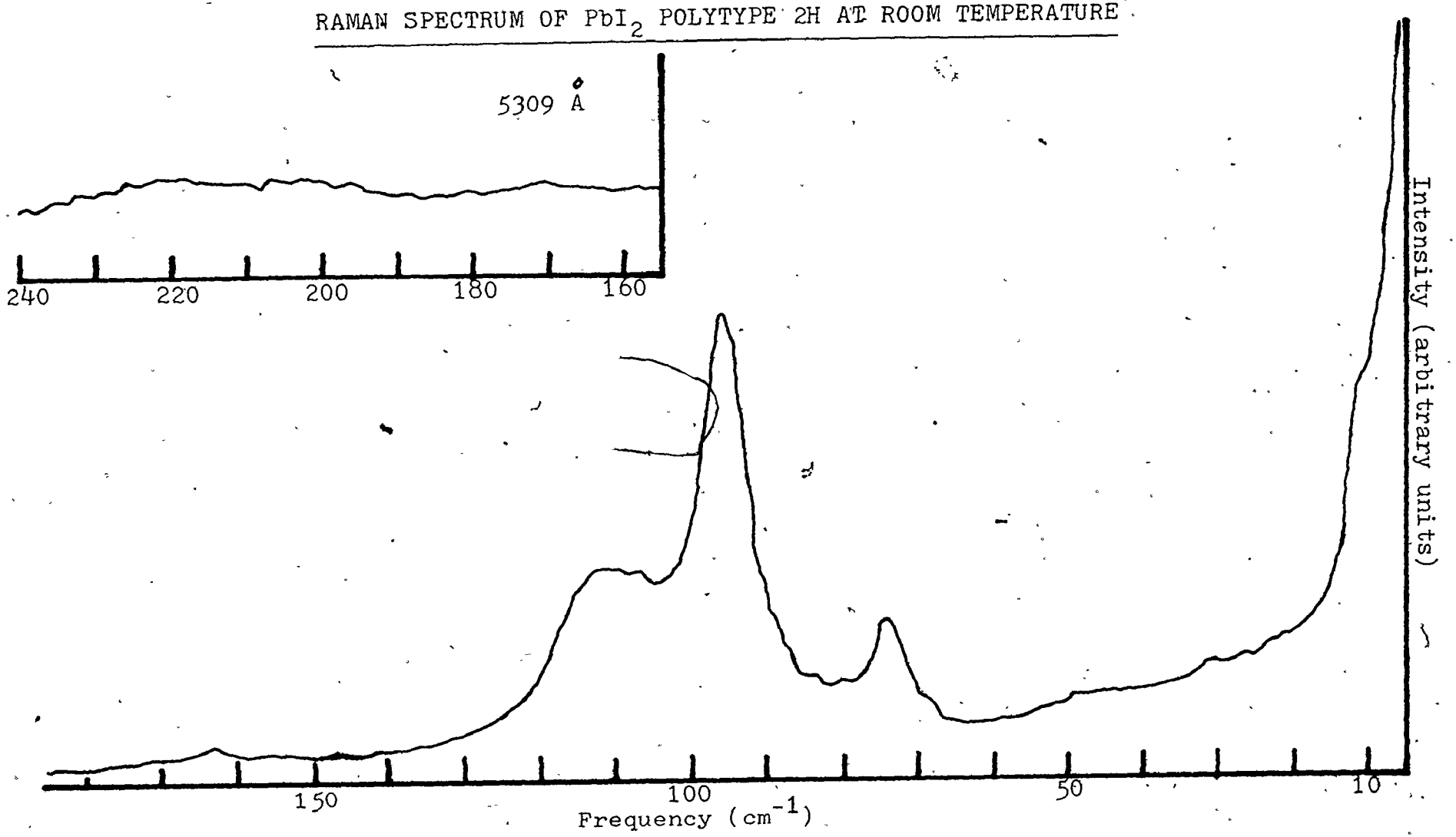

FIGURE 9

RAMAN SPECTRUM OF PbI_2 POLYTYPE 2H AT 50 K

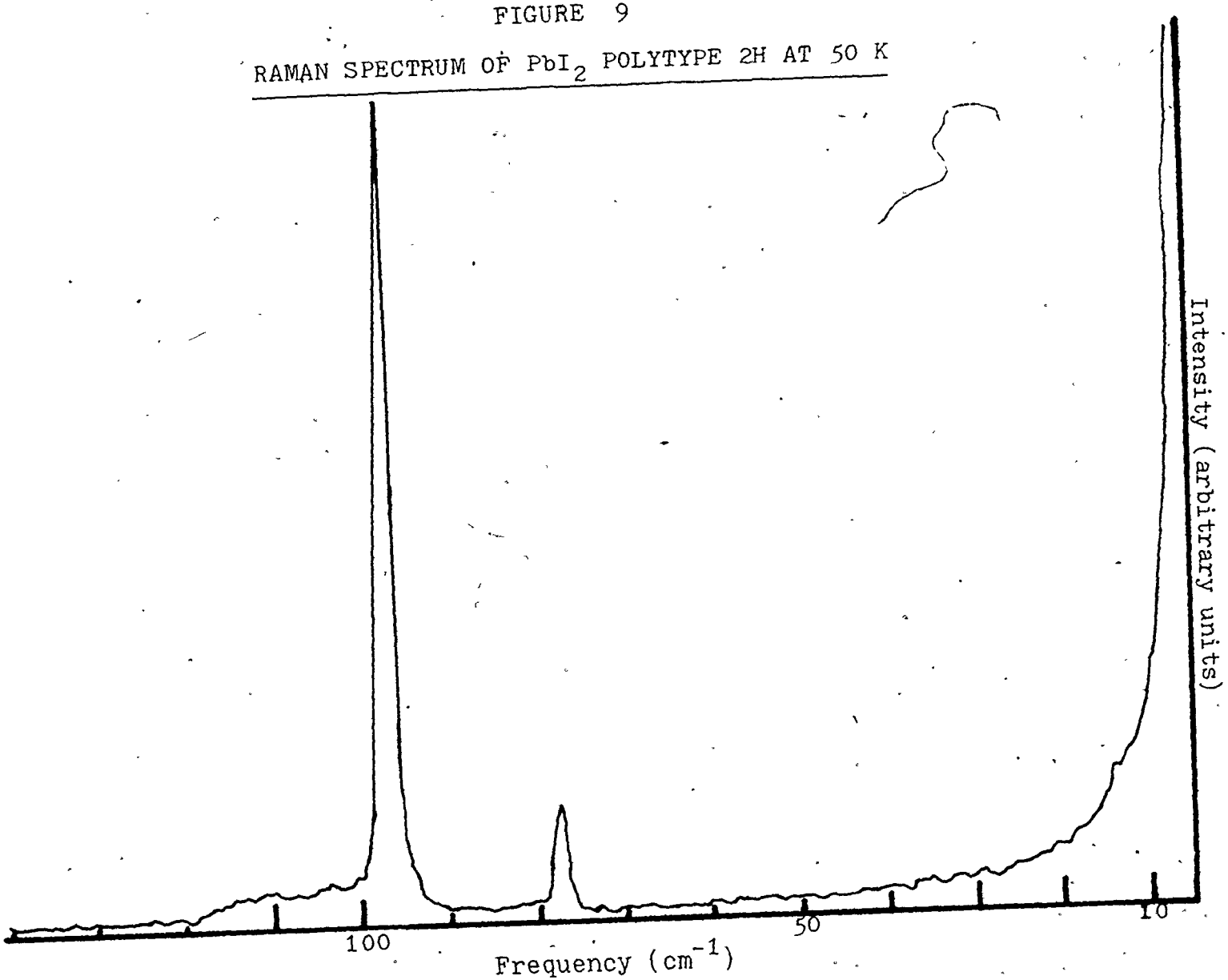

TABLE 3

ASSIGNMENT OF RAMAN LINES IN FIGURES 8 AND 9 PbI_2-2H

Frequencies (cm^{-1})				
Rm Temp	200 K	50 K	Mode	Activity
74.0±0.5	76.5±0.3	77.5±0.5	E_g	$a_{xx} - a_{yy}$, a_{xy} a_{yz}, a_{zx}
95.5±0.5	96.8±0.5	97.3±0.2	A_{1g}	$a_{xx} + a_{yy}$, a_{zz}
106±1	--------	--------	$2E_u$	T_x, T_y
113±1	--------	--------	A_{2u}	T_z
165±5	--------	--------	$2E_g$	$a_{xx} - a_{yy}$, a_{xy} a_{yz}, a_{zx}
205±5	--------	--------	$4E_u$	T_x, T_y
220±5	--------	--------	$2A_{2u}$	T_z

TABLE 4

FREQUENCIES OF RAMAN LINES FROM THE LITERATURE PbI_2-2H

Mode	Frequency (cm^{-1})	Temperature (K)	Reference
E_g	75	Rm	21
	76	Rm	22
	74	Rm	20
	79.0±0.5	77	7
A_{1g}	100	Rm	21
	94.3	Rm	22
	96	Rm	20
	98.0±0.5	77	7
$2E_u$, A_{2u}	120	Rm	21
	101	Rm	22
	110	Rm	20
	106, 113	77	7

found here but are misassigned in the paper.

In reference 7, infrared reflectivity data are presented along with the Raman frequencies. The results were used to assign the anomalous modes in the Raman measurements.

3.1.3 Raman Spectra of 4H-PbI_2

Polytype 4H-PbI_2 contains two molecules per unit hexagonal cell with space group $P6_3mc$ or C_{6v}^4. The site symmetries are; 2Pb at C_{3v} and two sets of 2I at C_{3v}.[39] These six atoms per unit cell lead to 18 vibrational modes at q=0:[40]

$$3A_1 + 3B_1 + 3E_1 + 3E_2.$$

The modes $2A_1 + 2E_1 + 3E_2$ are Raman active with the $2A_1 + 2E_1$ being also infrared active. The remaining $A_1 + E_1$ modes are acoustical with the $3B_1$ not showing any optical activity. Table 5 gives a correlation between the modes of 2H and 4H PbI_2. Figures 10 and 11 give typical spectra of a 4H PbI_2 sample at room and low temperatures and a summary of the results appears in Table 6.

The first thing to note in the 4H spectrum is the appearance of a rigid layer mode at 13.6 cm^{-1}. At room temperature, this is a very strong line which was identified as a E_2 mode by the polarization. Also identified in this manner was the peak at 70.0 cm^{-1}. Given these assignments, the rest fall into place when a comparison is made with the

TABLE 5

CORRELATION DIAGRAM FOR MODES OF 2H AND 4H PbI_2

D_{3d}(2H)	C_{6v}(4H)
A_{1g}	A_1
	B_1
E_g	E_1
	E_2
$2A_{2u}$	$2A_1$
	$2B_1$
$2E_u$	$2E_1$
	$2E_2$

FIGURE 10

RAMAN SPECTRUM OF PbI_2 POLYTYPE 4H AT ROOM TEMPERATURE

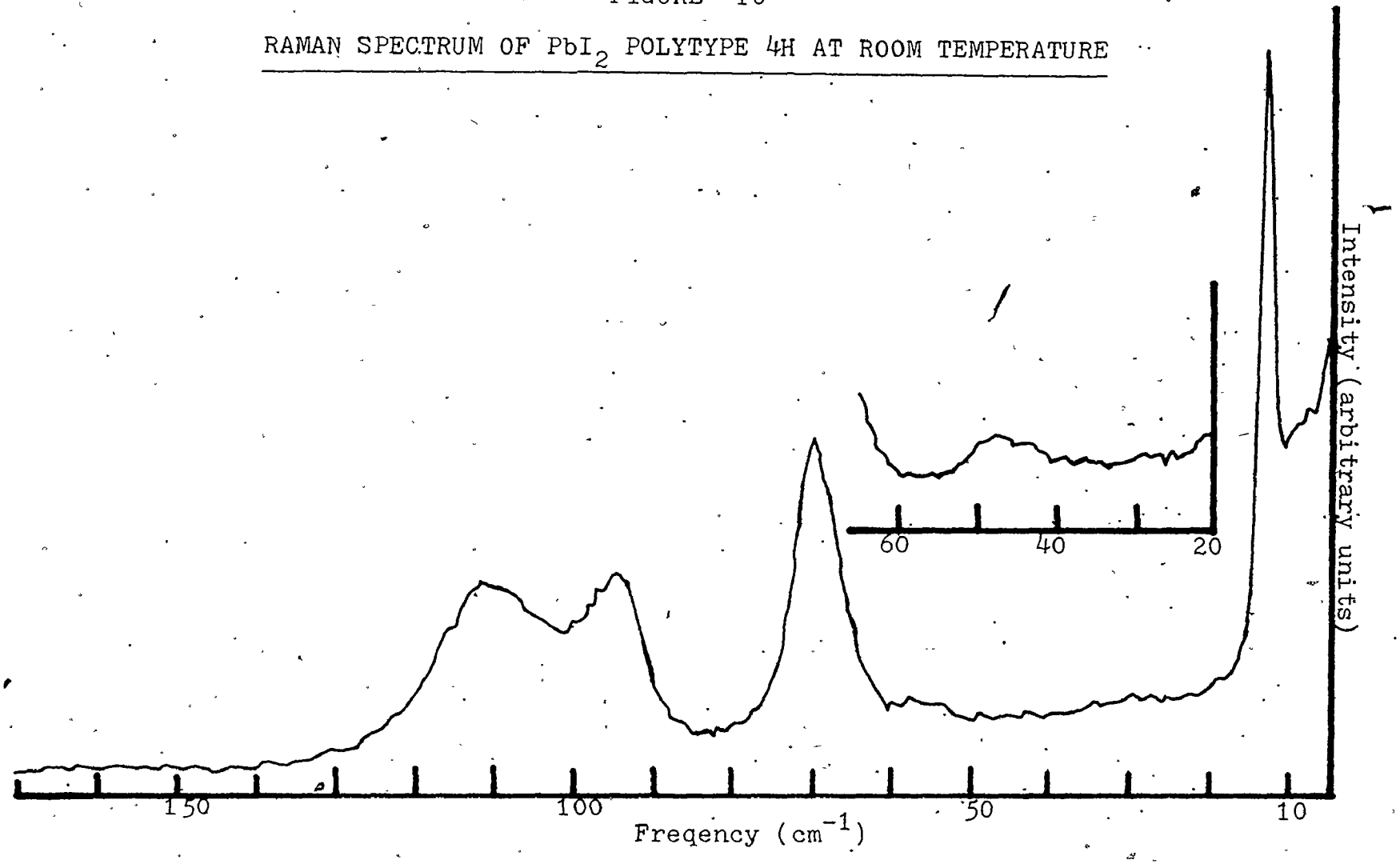

FIGURE 11

RAMAN SPECTRUM OF PbI_2 POLYTYPE 4H AT 50 K

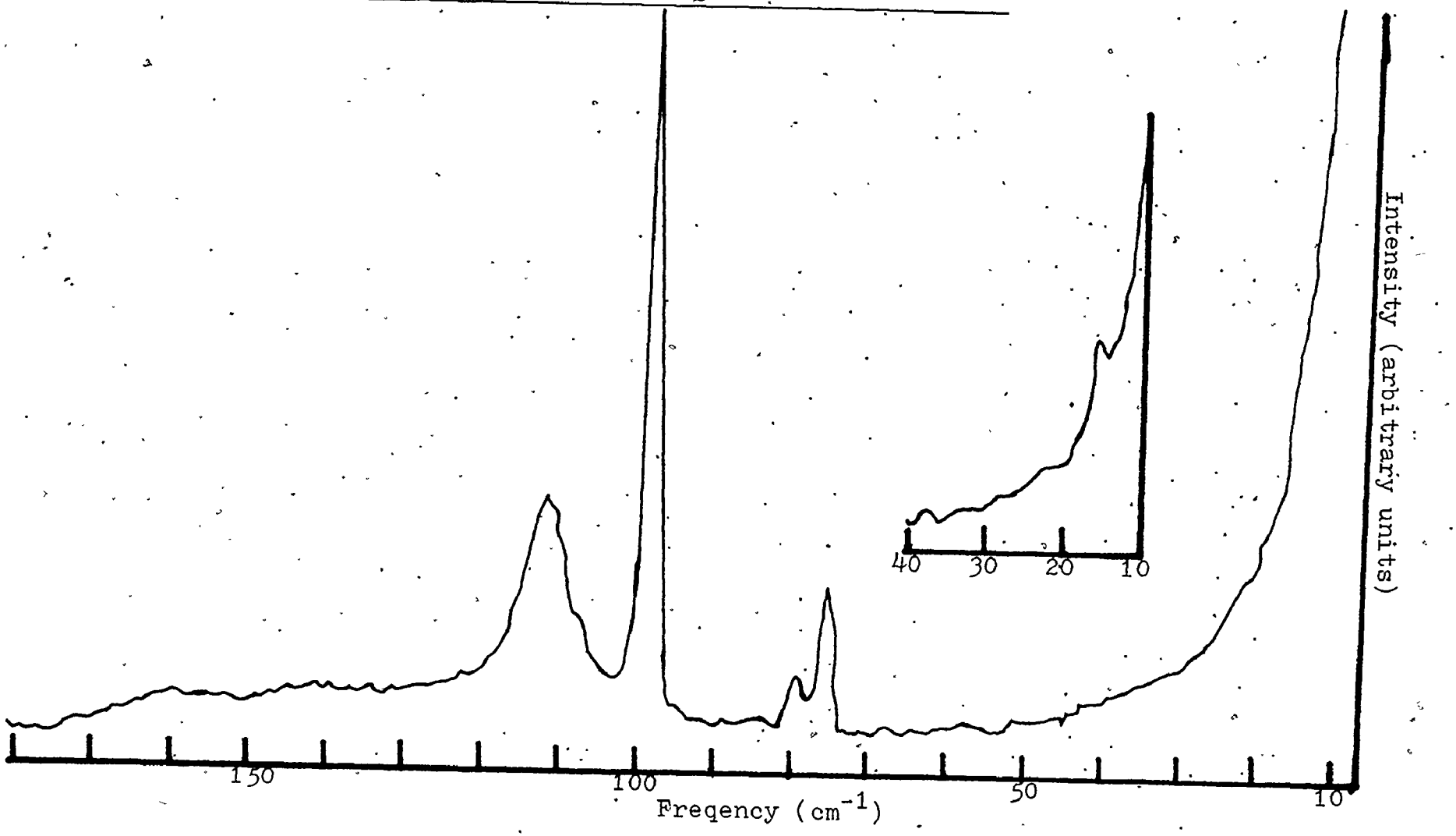

TABLE 6

ASSIGNMENT OF RAMAN LINES IN FIGURES 10 AND 11 PbI_2-4H

Frequency (cm^{-1})				
Rm Temp	200 K	50 K	Mode	Activity
13.6±0.2	-------	15.2±0.2	E_2^3	$a_{xx} - a_{yy}$, a_{xy}
48.5±0.5	-------	-------	E_2^2, E_1^2	$a_{xx} - a_{yy}$, a_{xy} or a_{yz}, a_{zx}, T_x, T_y
70.0±0.5	74.0±0.5	74.6±0.2	E_2^1	$a_{xx} - a_{yy}$, a_{xy}
-------	-------	78.1±0.2	E_1^1	a_{yz}, a_{zx}, T_x, T_y
95.5±0.5	96.8±0.5	97.3±0.2	A_1^1	$a_{xx} + a_{yy}$, a_{zz}, T_z
106±1	-------	-------	$2E_1^2$	a_{yz}, a_{zx}, T_x, T_y
113±1	-------	111.1±0.5	A_1^2	$a_{xx} + a_{yy}$, a_{zz}, T_z
165±5	-------	-------	$2E_1^1, 2E_2^1$	a_{yz}, a_{zx}, T_x, T_y and $a_{xx} - a_{yy}$, a_{xy}

TABLE 7

FREQUENCIES OF RAMAN LINES FROM THE LITERATURE PbI_2-4H

Mode	Frequency (cm^{-1})	Temperature (K)	Reference
E_2^3	13.5	Rm	20
	15.6	9	20
	15.5±0.5	77	7
E_1^2, E_2^2	51±2	77	7
E_2^1	75.2	36	23
	72	Rm	20
	73.9	9	20
	75.0±0.5	77	7
E_1^1	78.2	36	23
	77.2	9	20
	78.5±0.5	77	7
A_1^1	97	36	23
	96	Rm	20
	98.0±0.5	77	7
$2E_1^2, A_1^2$	107, 112	36	23
	106, 113	77	7
$2E_1^1, 2E_2^1$	151, 171.8	36	23
$2A_1^2$	223.2	36	23

FIGURE 12

PHONON DISPERSION CURVES FROM RAMAN (4H) MEASUREMENTS

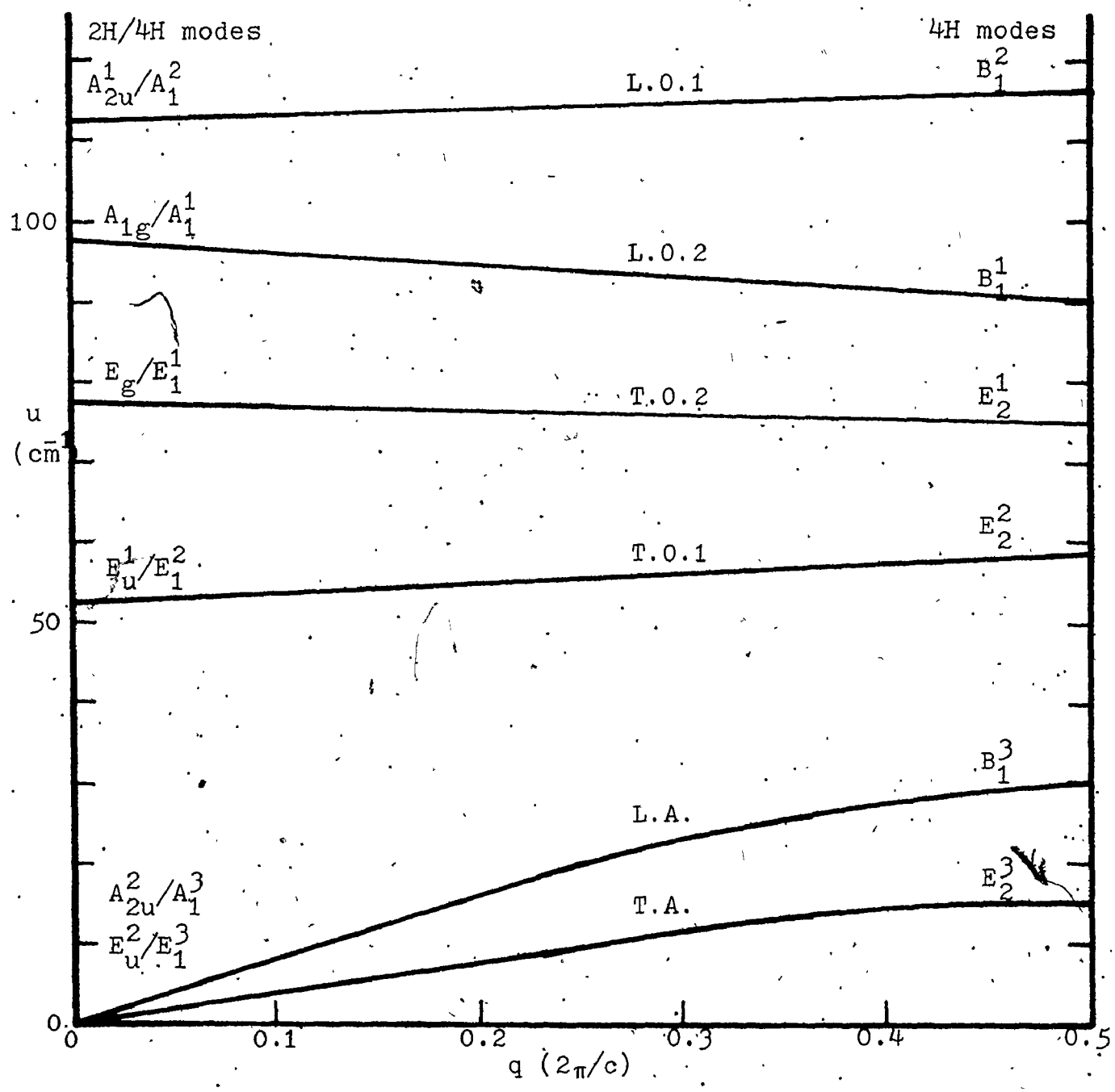

2H spectrum.

At low temperatures, the peak at 15.2 cm^{-1} loses much of its intensity which makes it hard to locate accurately. This is also a problem in analysing the spectra of higher polytypes. The peak at 48.5 cm^{-1} was only seen clearly once in a sample of PbI_2 which was a coalescence of 4H and 12R. Its position identifies it as being related to the 2H infrared mode E_u. The expected splitting was not observed. The splitting of the 2H E_g mode at about 75 cm^{-1} is clearly seen, however, at low temperatures. Again, for comparison, Table 7 gives the Raman frequencies for polytype 4H that have been published. However, it is important to note that the structure of none of the crystals was confirmed by X-rays. The crystals were prepared by different techniques: sublimation,[23] thermal annealing,[20] or Bridgman.[7] It should be realized that the crystals could just as easily have been 12R or an aggregate of 4H and 12R. The difference between the Raman spectrum of 4H and 12R turns out to be small (see section 3.1.7).

In reference 25, there is listed a Raman peak at 25.0 cm^{-1} (36 K) which is incorrectly identified as the $E_2{}^3$ mode. Why a line should be seen here is not obvious but Zallen and Slade [20] suggest that Nakashima [23] observed the $B_1{}^3$ mode (longitudinal rigid layer). The B_1 modes are, however, as mentioned before, optically forbidden.

The extra modes which appear as a result of the doub-

ling of the unit cell from 2H to 4H can be thought of as additional optical branches which then occur at q=0 through the halving of the Brillouin zone in the c-direction. Figure 12 shows the complete zone for the 2H structure based partly on the work of Dorner et al (neutron scattering measurements on PbI_2)[24] and partly on the results of Raman and infrared measurements.

The neutron work provides the lowest three bands and therefore the identification of the E_u^1 mode seems certain. The Raman frequencies give the next two without question but the highest frequency band is somewhat uncertain because it lies in the middle of the second order Raman spectrum just beyond the strong A_{1g} mode.

3.1.4 Raman Spectra of 6H-PbI_2

Polytype 6H-PbI_2 contains three molecules per unit hexagonal cell with space group P3m1 or C_{3v}^1. All the atoms are placed on single atom sites of symmetry C_{3v}.[39] The 9 atoms lead to 27 vibrational modes at q=0:[40]

$$9A_1 + 9E.$$

One set of $A_1 + E$ are acoustical modes. The rest, $8A_1 + 8E$, are both Raman and infrared active. Table 8 gives the rather simple correlation between the modes of 2H and 6H PbI_2. Figure 13 shows the additional modes that should occur for the 6H crystal.

The modes at $q=2\pi/3c$ would be split due to the

TABLE 8

CORRELATION DIAGRAM FOR MODES OF 2H AND 6H PbI_2

D_{3d}(2H)	C_{3v}(6H)
A_{1g}	$3A_1$
E_g	$3E$
$2A_{2u}$	$6A_1$
$2E_u$	$6E$

FIGURE 13

PHONON DISPERSION CURVES FROM RAMAN (6H) MEASUREMENTS

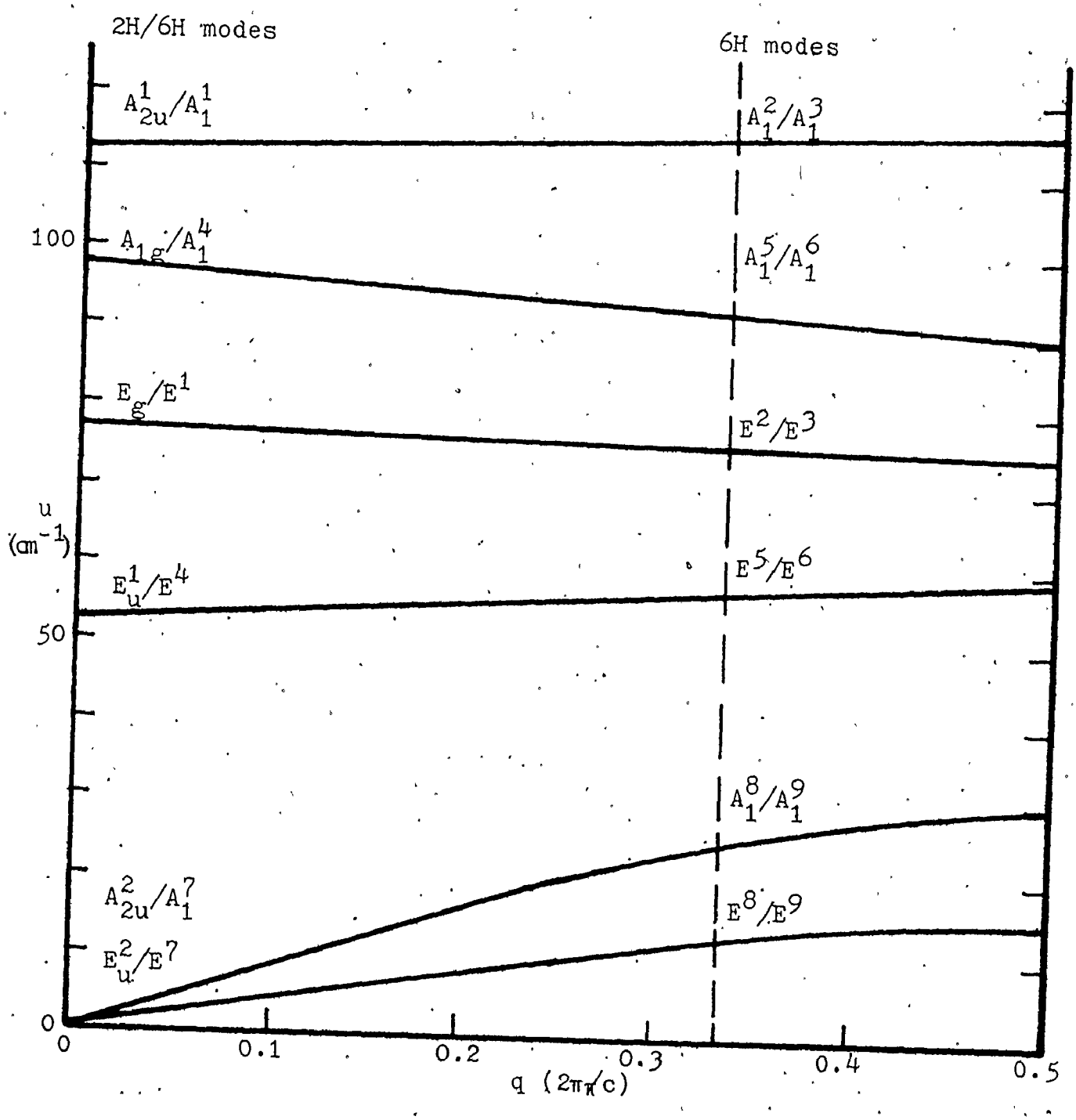

FIGURE 14

RAMAN SPECTRUM OF PbI_2 POLYTYPE 6H AT ROOM TEMPERATURE

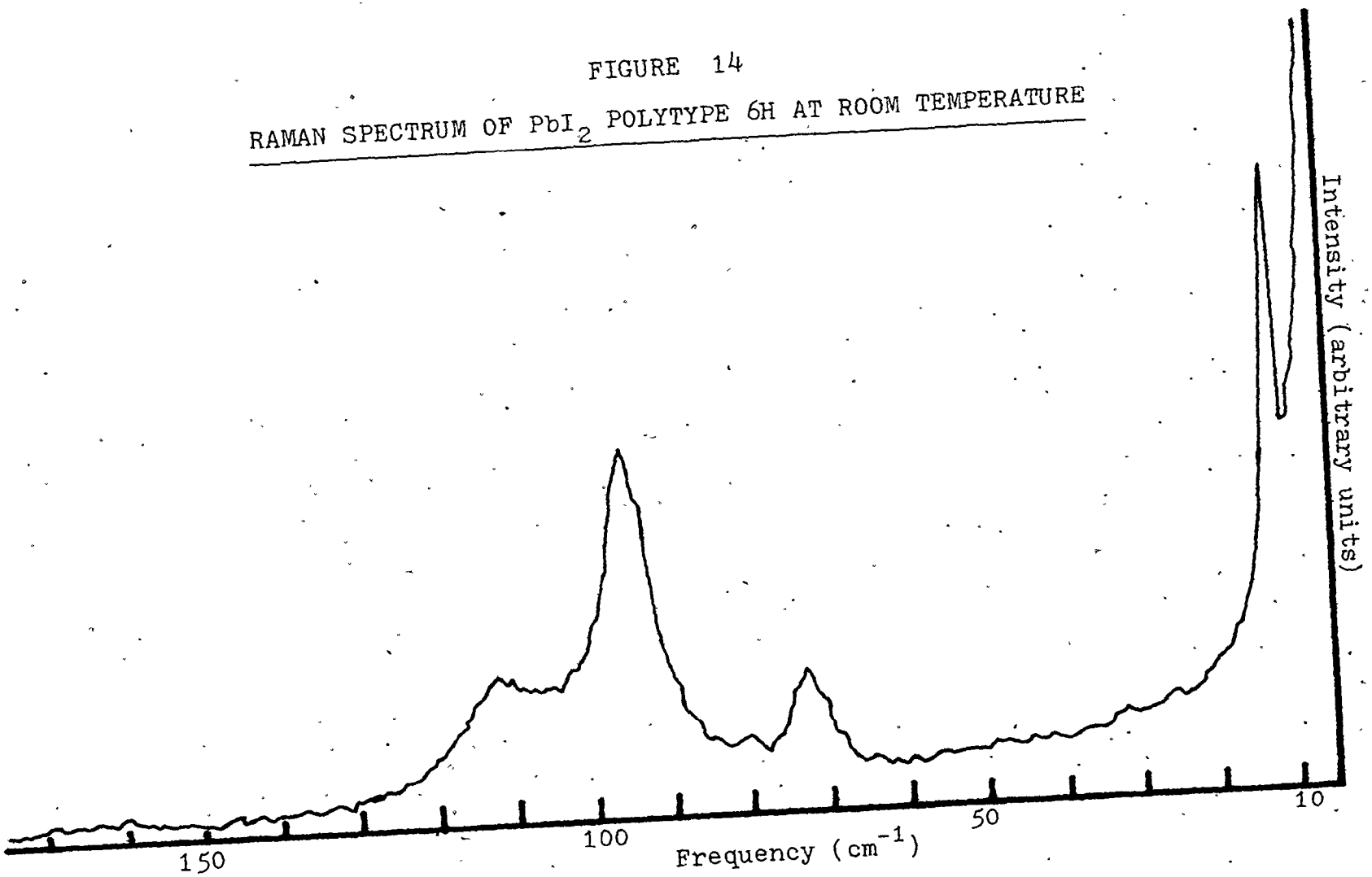

FIGURE 15

RAMAN SPECTRUM OF PbI_2 POLYTYPE 6H AT 50 K

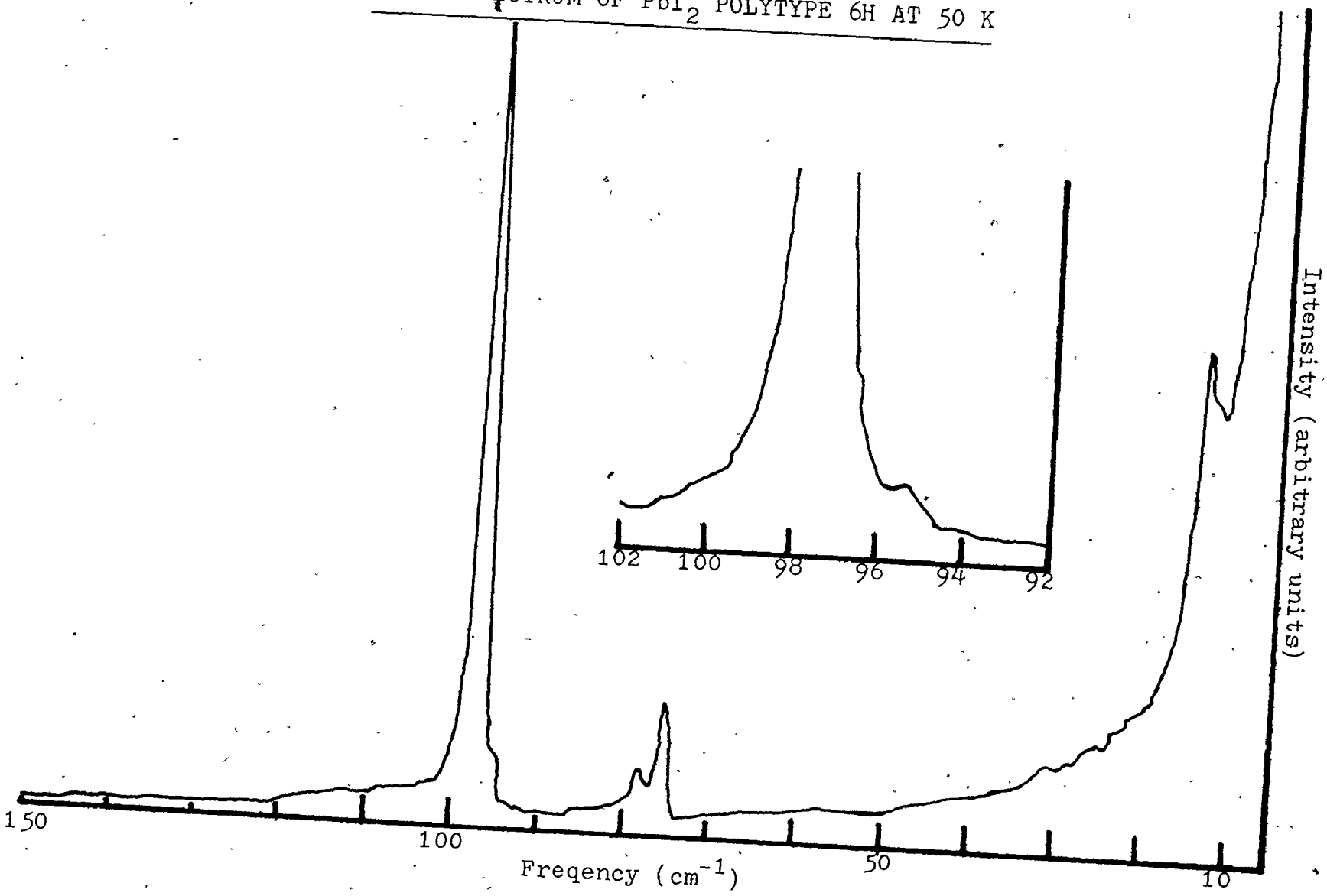

TABLE 9

ASSIGNMENT OF RAMAN LINES IN FIGURES 14 AND 15 PbI_2-6H

Frequency (cm^{-1})				
Rm Temp	200 K	50 K	Mode	Activity
12.8±0.2	13.5±0.2	13.8±0.2	E^8, E^9	$a_{xx} - a_{yy}$, a_{xy} a_{yz}, a_{zx}, T_x, T_y
72.3±0.2	73.5±0.5	75.5±0.3	E^2, E^3	"
-------	-------	77.9±0.3	E^1	"
-------	-------	95.1±0.2	A_1^5, A_1^6	$a_{xx} + a_{yy}$, a_{zz}, T_z
95.5±0.5	96.8±0.5	97.3±0.2	A_1^4	"

folding of the Brillouin zone at that point. This difference could not be detected in the Raman spectra, however, and so the modes will be treated as one. This is important to the assumption that the dispersion curves can be measured by the Raman effect.

Figures 14 and 15 show typical spectra of a 6H PbI_2 sample at room and low temperatures with a summary in Table 9. No polarization measurements were attempted with the 6H crystal as there are no ambiguities to be resolved in the assignment of the peaks in the Raman spectrum. The A_1 and E modes are obvious from the correlation table and the work on 2H and 4H.

The rigid layer mode (E^8,E^9) was very strong and distinct in this crystal. It lost intensity at lower temperatures but was still easily measured. The 2H longitudinal acoustic mode is Raman active in 6H (as all modes are in 6H) but was not observed. The modes around 50 cm^{-1} (E^4,E^5,E^6) were likewise too weak to be resolved.

The E^1 and E^2,E^3 pair were easily separated at low temperatures and thus can easily be placed on the dispersion curve which we are now building up. There is, of course, no distinction of symmetry.

In 6H the partner of the $A_1{}^4$ mode (A_{1g} in 2H) becomes active and, in fact, was observed (the $A_1{}^5$,$A_1{}^6$).

The second order effects above 100 cm^{-1} were indistinguishable from those in 2H. No additional modes

could be differentiated.

3.1.5 Raman Spectra of 8H-PbI_2

Polytype 8H-PbI_2 contains four molecules per unit hexagonal cell, but the exact structure has not been determined. Layer structures of the PbI_2 or CdI_2 type can only have space groups P3m1, $P\bar{3}m1$, $P6_3mc$, R3m1, $R\bar{3}m1$.[4] We recall that 2H had space group $P\bar{3}m1$, 4H the group $P6_3mc$, and 6H the group P3m1. Of these three, P3m1 would seem to be the most probable for 8H.[41] Considering that there would be 36 modes for the 12 atoms and that the symmetry is C_{3v}^1, the irreducible representation should be;[40]

$$12A_1 + 12E$$

where, as before, one set of $A_1 + E$ are acoustical and the rest, $11A_1 + 11E$, Raman and infrared active. The correlation of these modes with those of polytype 2H follows the pattern of Table 8. In Figure 16, the positions of these modes are indicated on the 2H large zone. The folding of the Brillouin zone, as before, causes the splitting of any modes occurring within the 2H large zone.

Figures 17 and 18 show typical spectra of an 8H-PbI_2 sample at room and low temperatures. Table 10 gives the observed frequencies and their probable assignment (from Figure 16).

The most important things to be noted are the observation of the transverse rigid layer modes and the

FIGURE 16

PHONON DISPERSION CURVES FROM RAMAN (8H) MEASUREMENTS

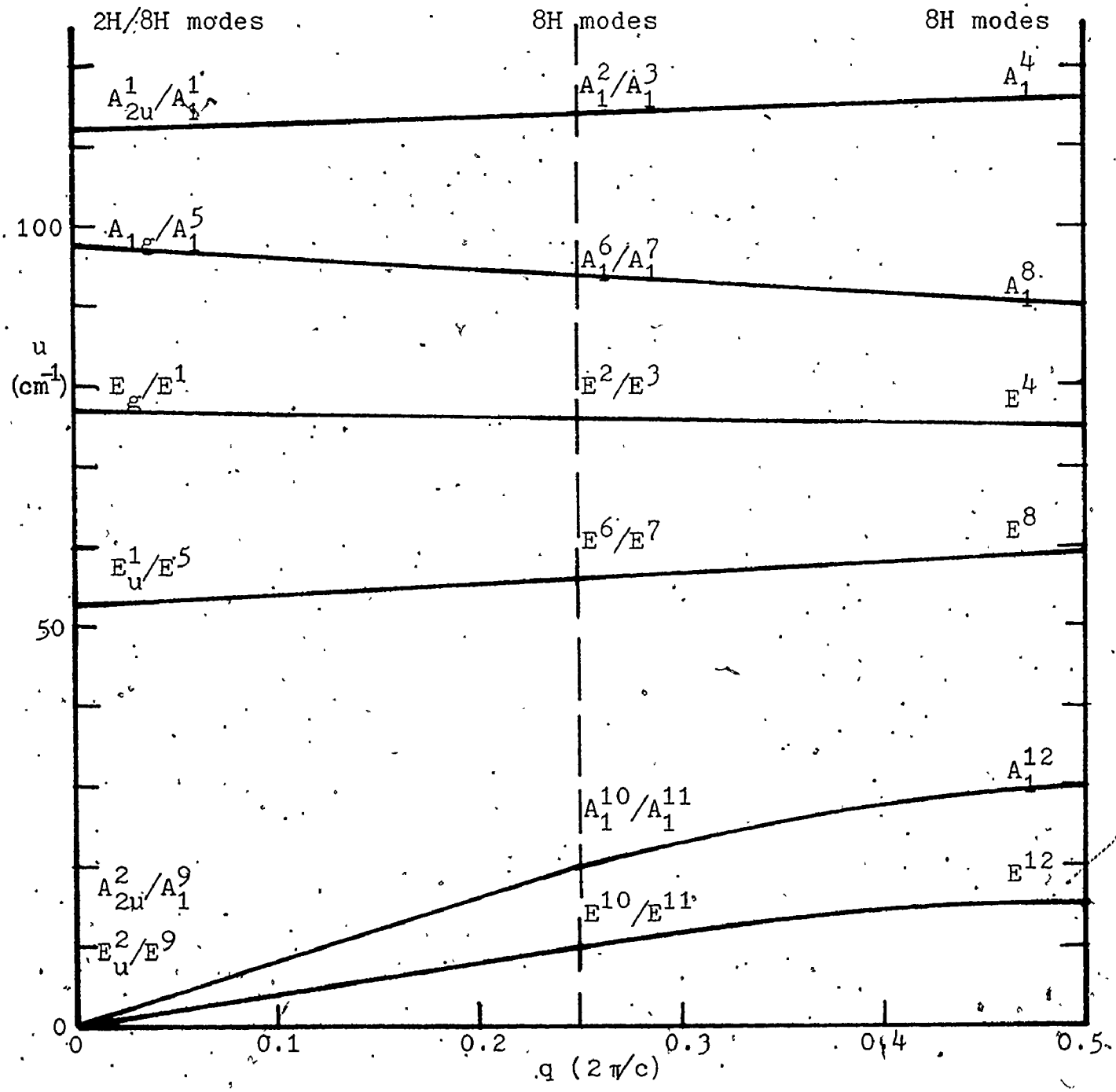

FIGURE 17

RAMAN SPECTRUM OF PbI_2 POLYTYPE 8H AT ROOM TEMPERATURE

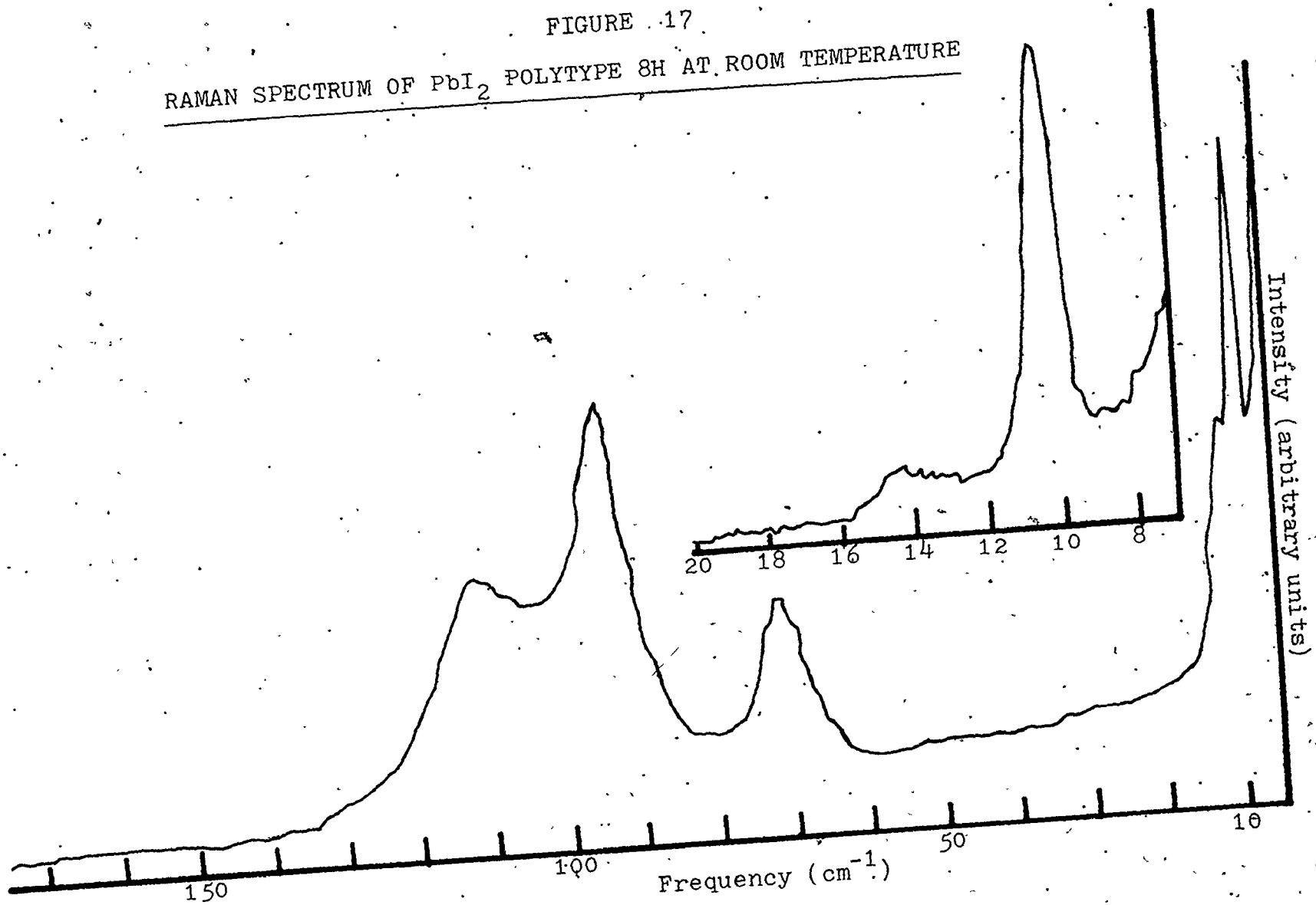

FIGURE 18

RAMAN SPECTRUM OF PbI_2 POLYTYPE 8H AT 50 K

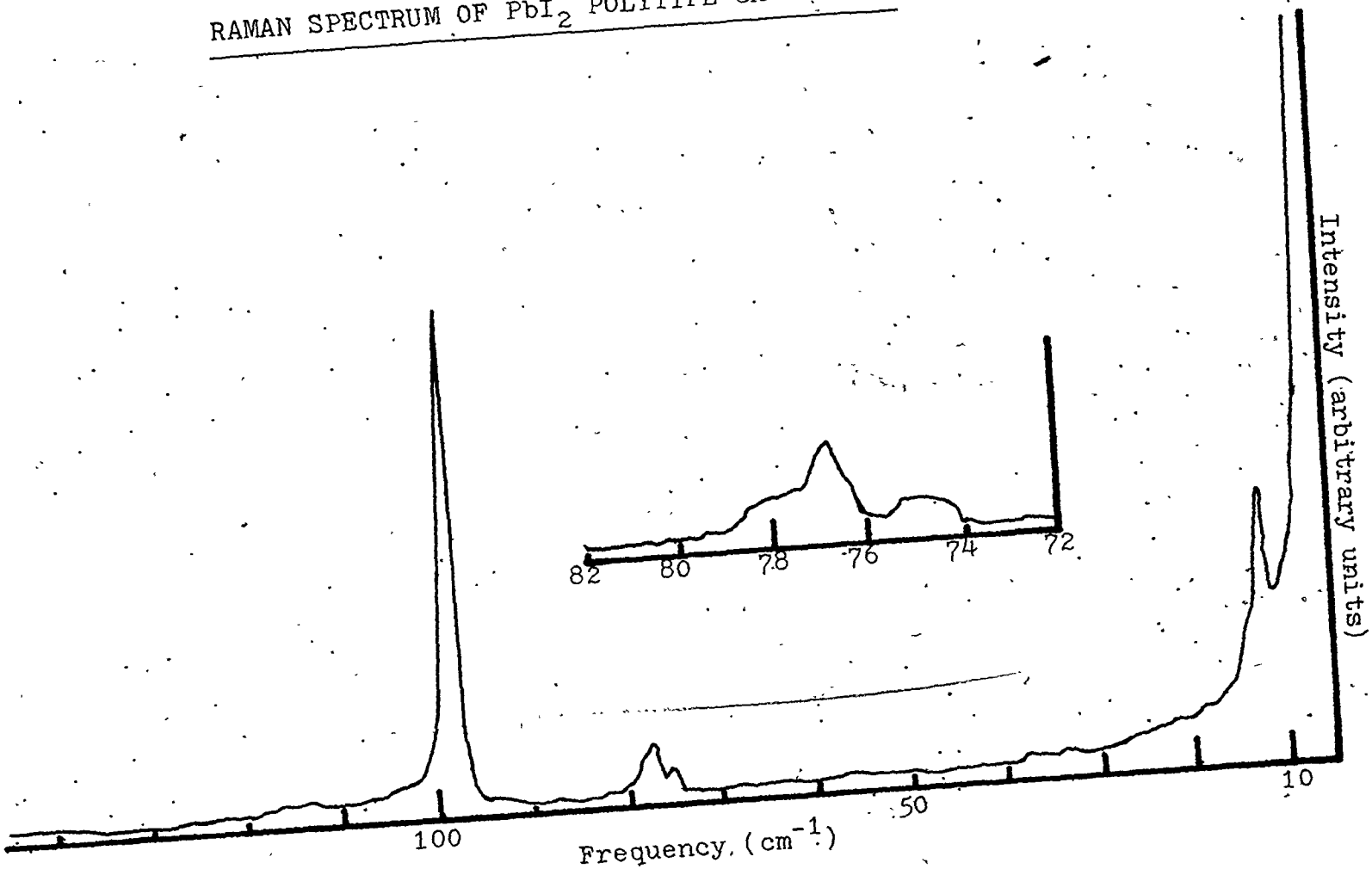

TABLE 10

ASSIGNMENT OF RAMAN LINES IN FIGURES 17 AND 18 PbI_2-8H

Frequency (cm^{-1})				
Rm Temp	200 K	50 K	Mode	Activity
10.4±0.2	11.0±0.2	11.8±0.2	E^{10}, E^{11}	$a_{xx} - a_{yy}$, a_{xy} a_{yz}, a_{zx}, T_x, T_y
13.6±0.5	-------	15.2±0.5	E^{12}	"
-------	-------	74.3±0.2	E^4	"
72.4±0.2	73.8±0.5	76.3±0.2	E^2, E^3	"
-------	-------	77.9±0.5	E^1	"
95.5±0.5	96.8±0.5	97.3±0.2	A_1^5	$a_{xx} + a_{yy}$, a_{zz}, T_z

clear triplet splitting of the E_g mode of polytype 2H. As before, some active modes were not observed and the second order effects above 100 cm^{-1} were indistinguishable from those of a 2H crystal.

3.1.6 Raman Spectra of 12H-PbI_2

Polytype 12H-PbI_2 contains six molecules per unit hexagonal cell and, following the argument used for 8H (because the 12H structure is also unknown), we assume a C_{3v}^1 space group and thus an irreducible representation of:[40]

$18A_1 + 18E$.

All modes are active and are shown on the 2H large zone of Figure 19. Figures 20 and 21 show typical spectra of a 12H-PbI_2 sample.

The 12H specimens were aggregated with 2H in all cases; the fraction of 12H was quite small. Therefore, the 12H features of the spectra tended to be very weak.

Although weak, the three transverse rigid layer modes expected on the basis of Figure 19 can be seen. There is also a new mode at $q=2\pi/6c$ (see Table 11 for summary). Because of the intensity reduction (of these modes) at low temperatures, only the positions of bands at room temperature could be determined. Of the four modes expected from transformation of the 2H E_g mode, only two were observed. The E^1 mode that corresponds to the 2H frequency was seen, of course, plus a central mode which was most likely the

FIGURE 19

PHONON DISPERSION CURVES FROM RAMAN (12H) MEASUREMENTS

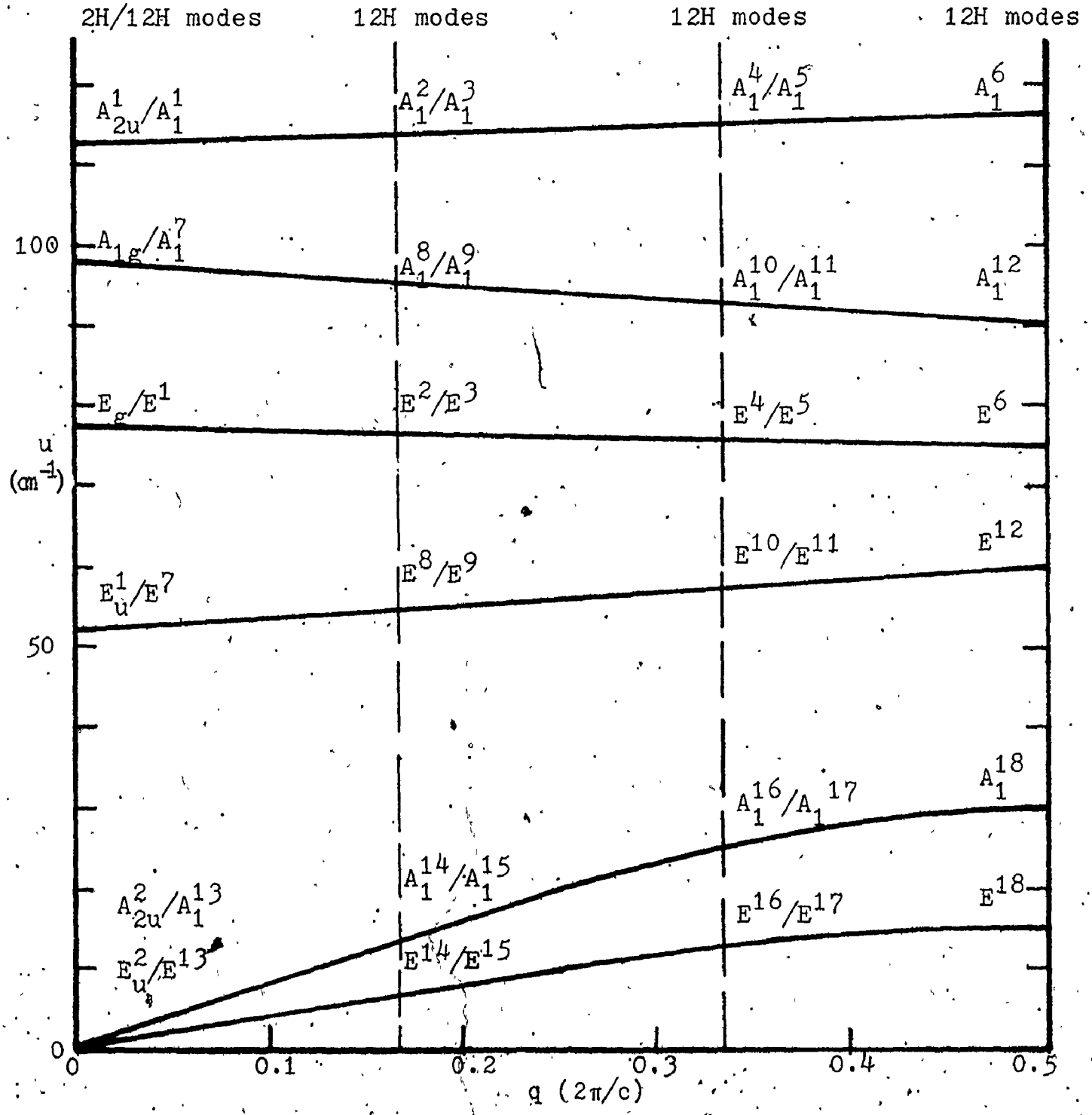

FIGURE 20

RAMAN SPECTRUM OF PbI_2 POLYTYPE 12H AT ROOM TEMPERATURE

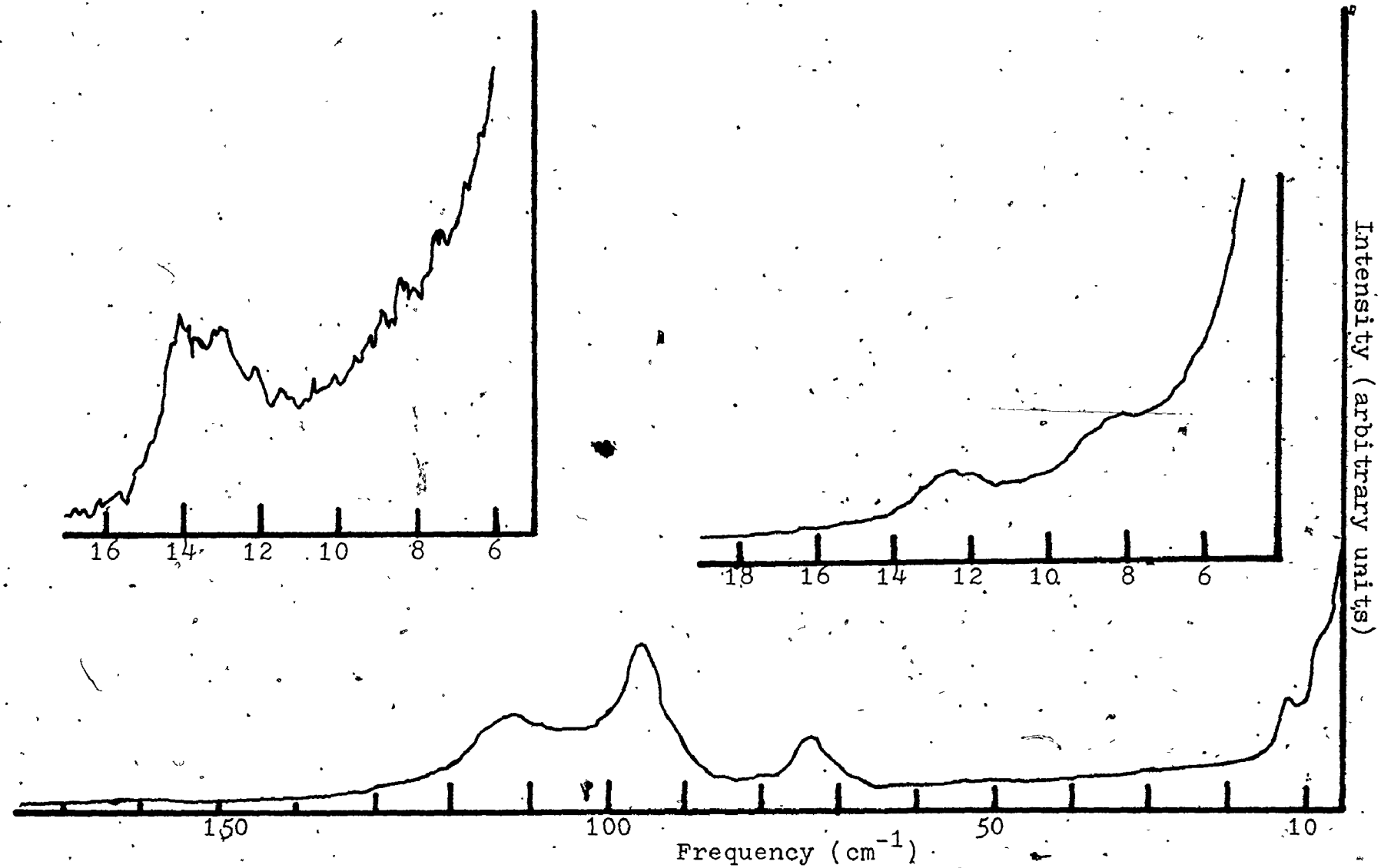

FIGURE 21

RAMAN SPECTRUM OF PbI_2 POLYTYPE 12H AT 50 K

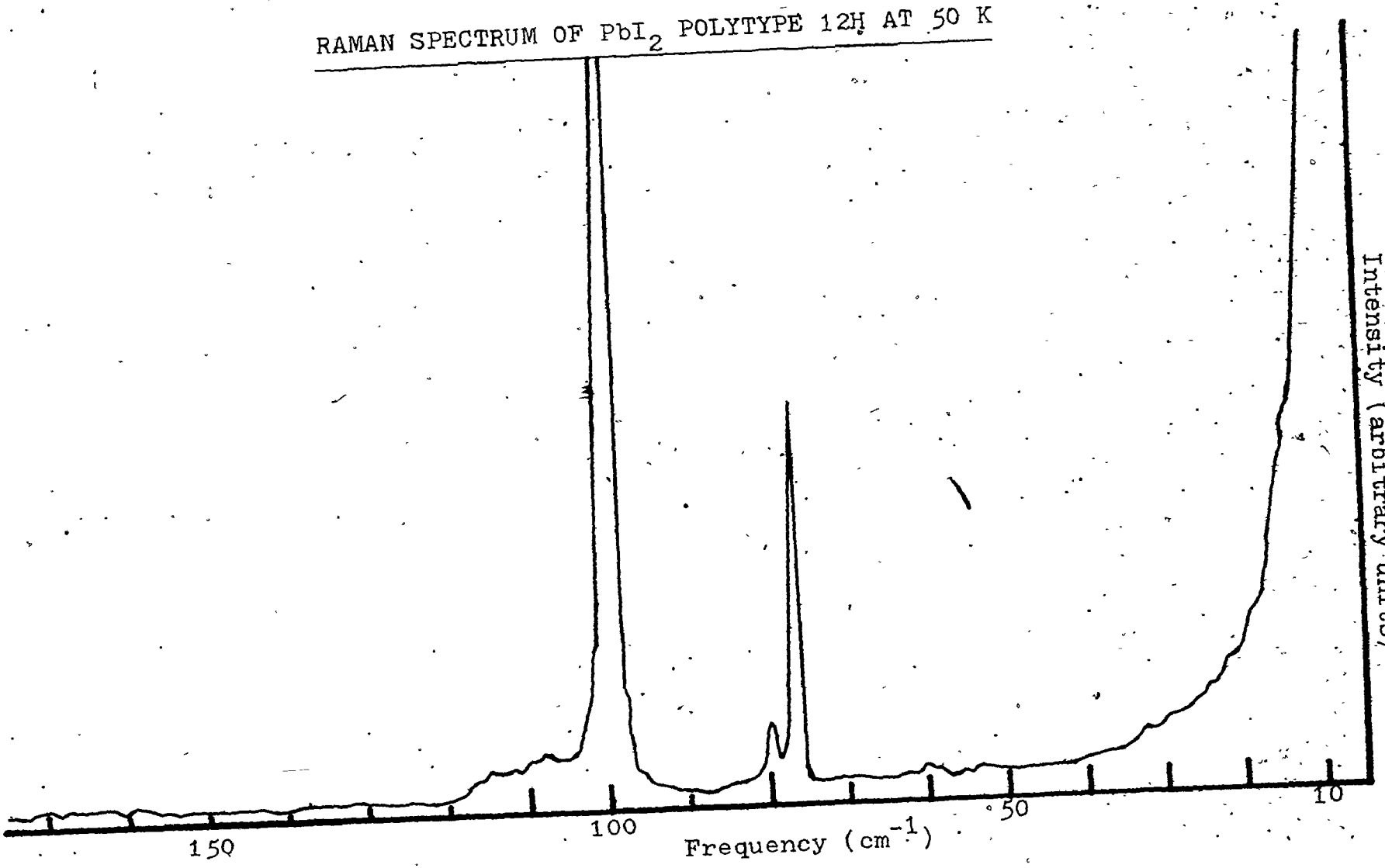

TABLE 11

ASSIGNMENT OF RAMAN LINES IN FIGURES 20 AND 21 PbI_2-12H

Frequency (cm^{-1})				
Rm Temp	200 K	50 K	Mode	Activity
8.5±0.2	-------	-------	E^{14}, E^{15}	$a_{xx} - a_{yy}$, a_{xy} a_{yz}, a_{zx}, T_x, T_y
12.8±0.2	-------	-------	E^{16}, E^{17}	"
13.6±0.2	-------	-------	E^{18}	"
71.5±0.2	-------	75.0±0.5	E^2, E^3 or E^4, E^5	"
74.0±0.5	-------	78.0±0.5	E^1	"
95.5±0.5	96.8±0.5	97.3±0.2	A_1^7	$a_{xx} + a_{yy}$, a_{zz}, T_z

E^4, E^5 combination (at the 6H position).

3.1.7 Raman Spectra of 12R-PbI_2

Polytype 12R-PbI_2 contains six molecules per unit hexagonal cell and two molecules per unit rhombohedral cell. The two molecules (6 atoms) lead to 18 vibrational modes at q=0. The space group is $R\bar{3}m$ or D_{3d}^5. The lead atoms are on separate sites of symmetry D_{3d}, and the iodine atoms on 2,2 atom, sites of symmetry C_{3v}.[39] As in the case of 2H, this gives an irreducible representation of;[40]

$$2A_{1g} + 2E_g + 4A_{2u} + 4E_u.$$

Of these, $2A_{1g} + 2E_g$ are Raman active, $3A_{2u} + 3E_u$ infrared and $A_{2u} + E_u$ acoustical. The 12R structure can be thought of as a doubling back of the Brillouin zone in the c-direction in the same manner as occurs in polytype 4H. But fewer Raman active modes should be observed (four compared with seven in polytype 4H). This is illustrated on the large zone dispersion curves of Figure 22.

It is apparent that no rigid layer modes should be observed in a 12R Raman spectrum. It would be useful to obtain infrared data on a 12R spectra to verify this point. The absence of rigid layer modes is obscured by the fact that a 12R sample is usually found aggregated with 4H. It was observed, however, that the 12R samples with smaller aggregates of 4H had a weaker Raman line at the E_u^4 position.

The results are summarized in Figures 23 and 24 and

FIGURE 22

PHONON DISPERSION CURVES FROM RAMAN (12R) MEASUREMENTS

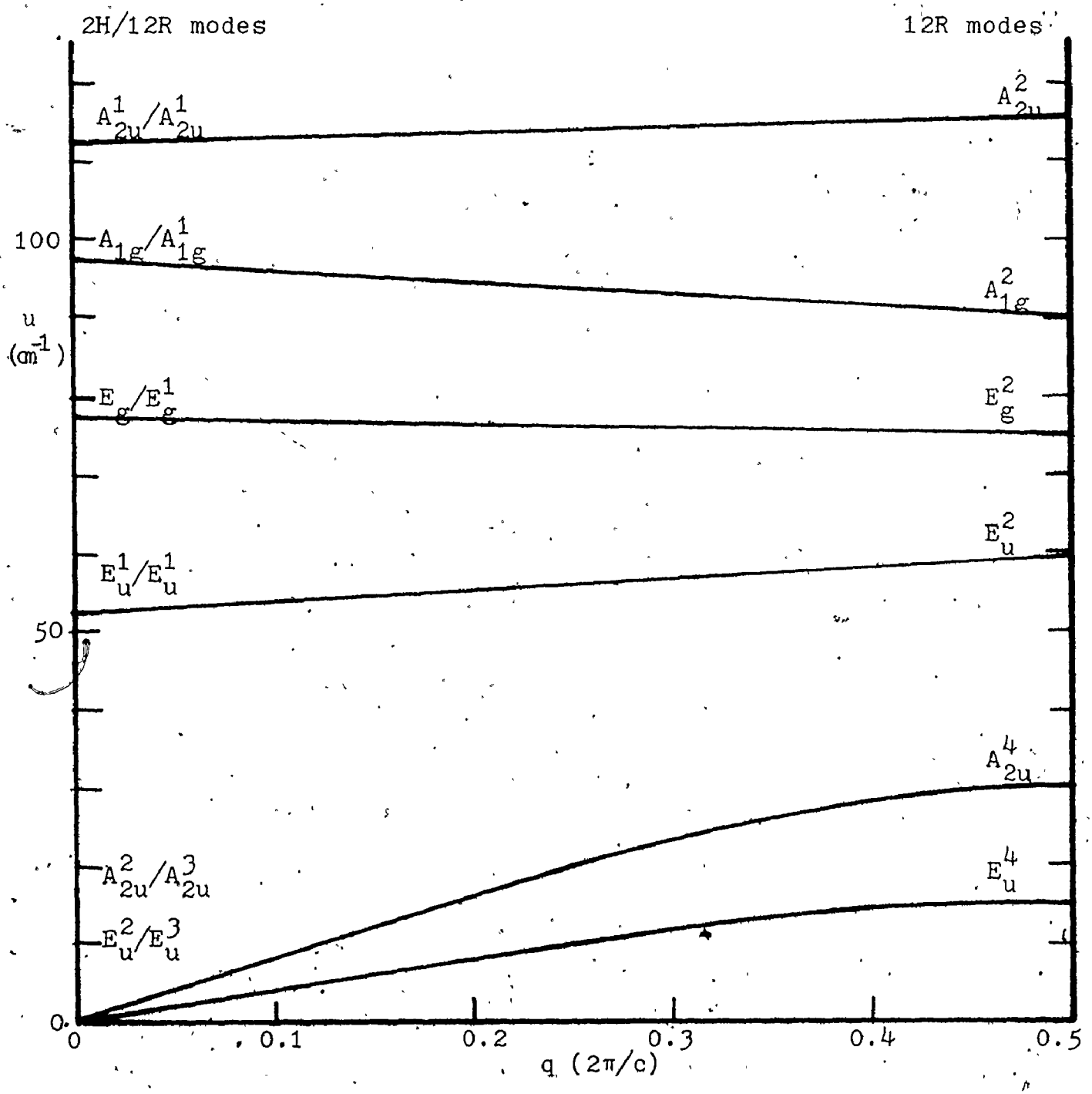

FIGURE 23

RAMAN SPECTRUM OF PbI_2 POLYTYPE 12R AT ROOM TEMPERATURE

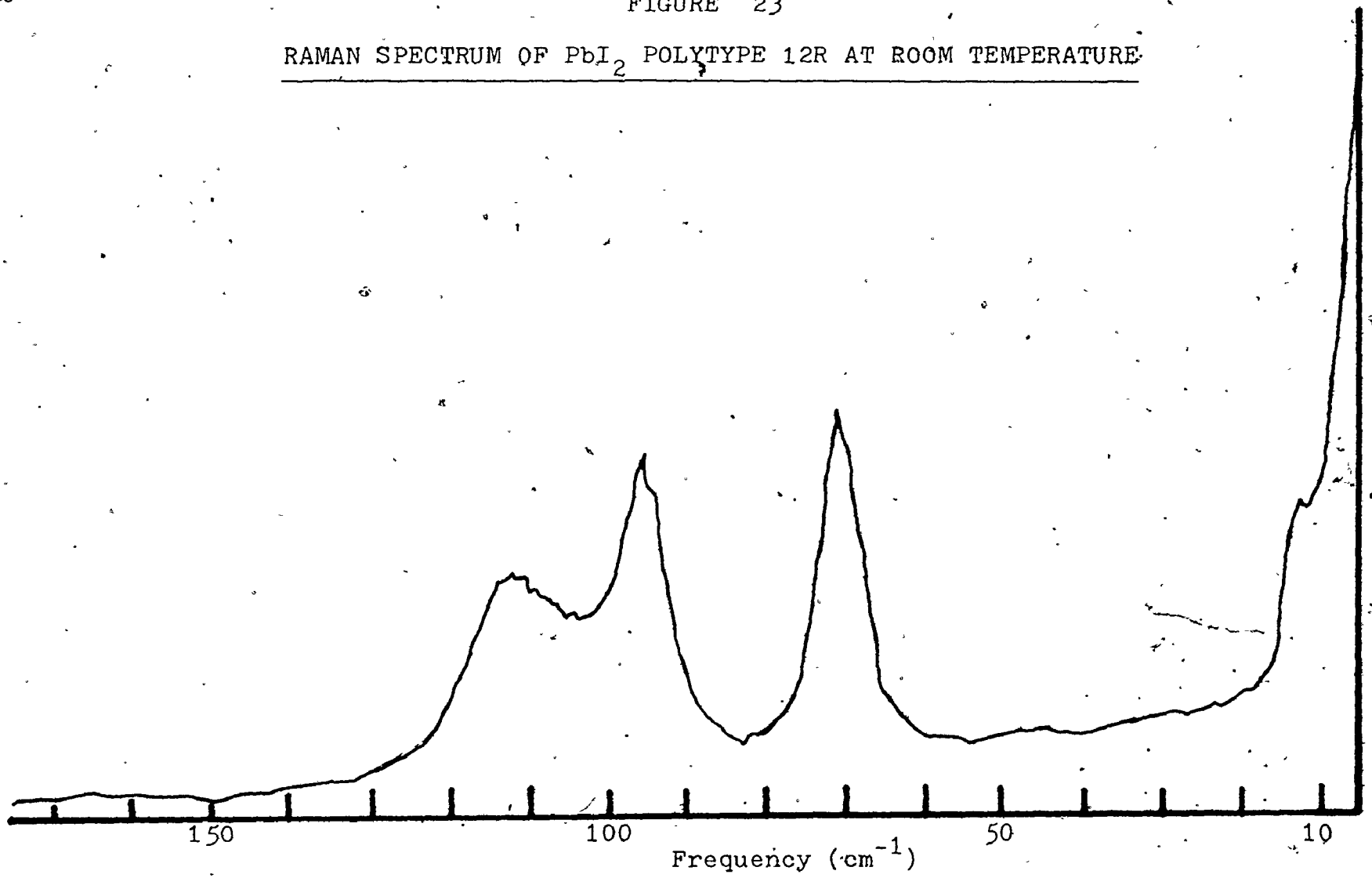

FIGURE 24

RAMAN SPECTRUM OF PbI_2 POLYTYPE 12R AT 50 K

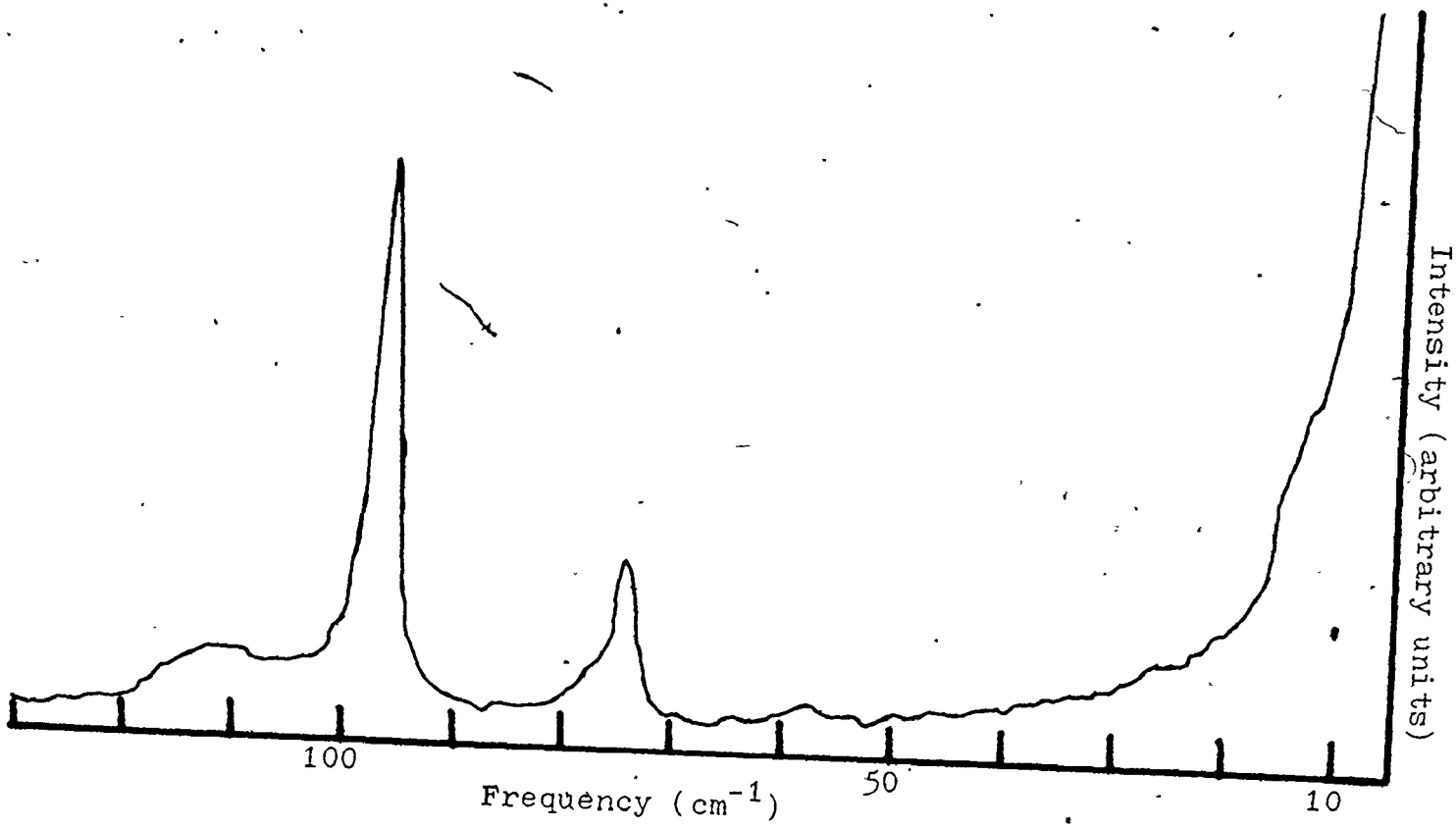

TABLE 12

ASSIGNMENT OF RAMAN LINES IN FIGURES 23 AND 24 PbI_2-12R

Frequency (cm^{-1})				
Rm Temp	200 K	50 K	Mode	Activity
70.0±0.5	-------	74.6±0.5	E_g^2	$a_{xx} - a_{yy}$, a_{xy} a_{yz}, a_{zx}
-------	-------	78.1±0.5	E_g^1	"
95.5±0.5	96.8±0.5	97.3±0.2	A_{1g}^1	$a_{xx} + a_{yy}$, a_{zz}

Table 12. Only one mode was not seen; the elusive partner of A_{1g}. There is no polarization distinction between the E_g^1 and E_g^2, of course, but the difference between A_{1g} and E_g was clearly evident in polarization measurements on the 12R specimens.

3.2 Correlation of Raman Frequencies with other Information on Vibrational Structure

3.2.1 Acoustic Branches

Figure 25 shows the doubly-degenerate transverse acoustic dispersion curve along the c-direction of PbI_2 as defined by the results of Raman or neutron scattering experiments. The neutron scattering results were obtained by Dorner et al [24] and the Raman data are as summarized in section 3.1.

It should be noted that, due to laser heating, the temperature of the PbI_2 crystal as measured by the Raman effect for the room temperature experiments was about 400 K. It is thus reasonable that the "room" temperature Raman data tend to lie below the results for the neutron scattering experiments. The exception, the mode at 8.5 cm^{-1} was obtained from the measurements on polytype 12H. The peak in the spectrum was, however, very weak and close to the Rayleigh line and thus its identification is less reliable.

The Raman frequencies for T=50 K are higher, as is to be expected, since the lattice should stiffen as the temperature is decreased.

The sound velocities corresponding to the long wave limit are;

$$v_t(\text{neutron, } 300\text{ K}) = 0.93\ (\pm 0.06) \times 10^5 \text{ cm/s}$$

$$v_t(\text{Raman, } 400\text{ K}) = 0.87\ (\pm 0.02) \times 10^5 \text{ cm/s}.$$

FIGURE 25

TRANSVERSE ACOUSTICAL DISPERSION CURVE ALONG c-DIRECTION OF PbI_2

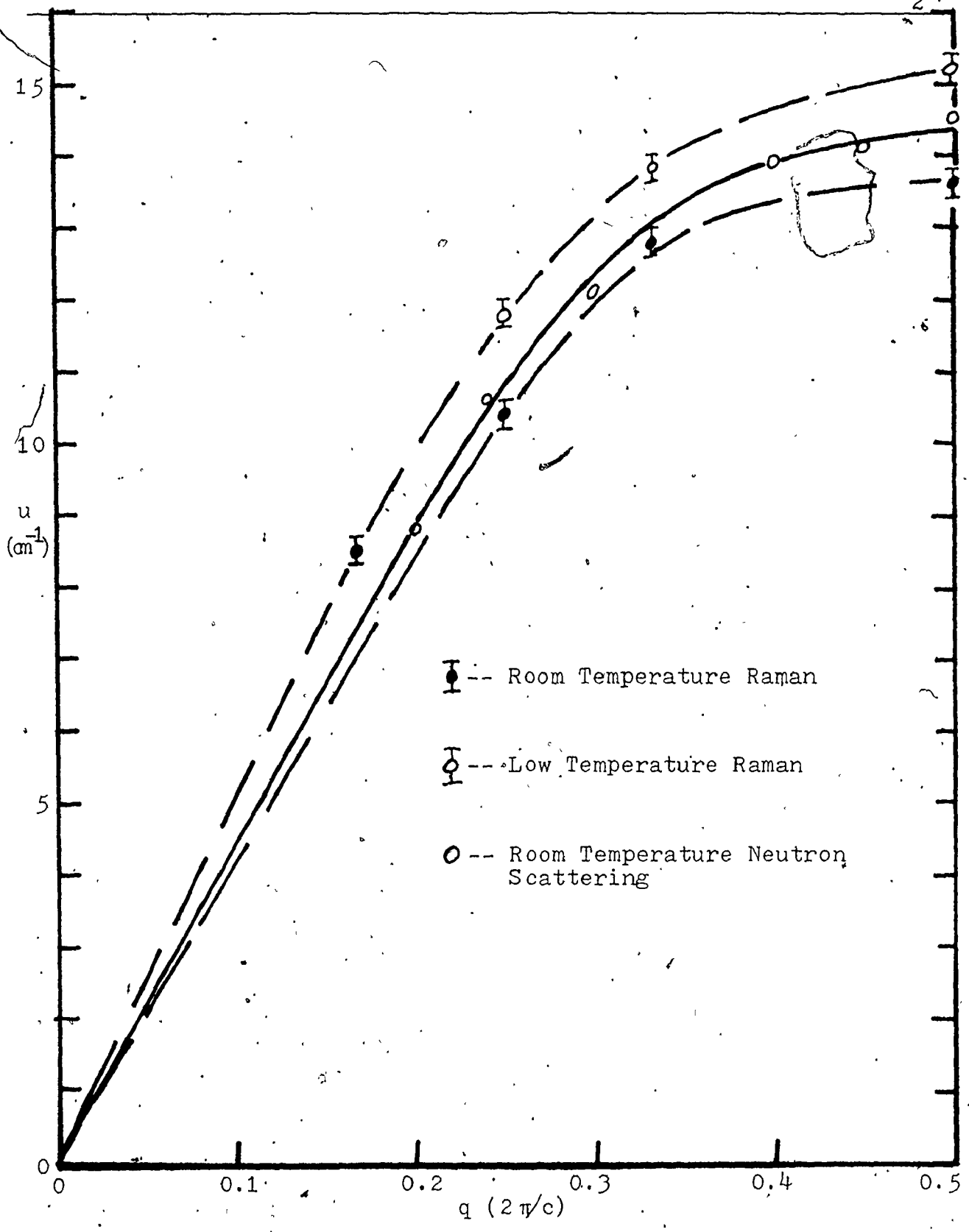

These agree nicely within the limits indicated. They are also consistent with a result from the measurement of Brillouin spectra;[25]

v_t(Brillouin, 300 K) = 1.00 ($\pm$0.02) x 10^5 cm/s.

The Raman result for the lower temperature indicates;

v_t(Raman, 50 K) = 1.06 ($\pm$0.03) x 10^5 cm/s.

No Raman features have definitely been observed which would correspond to the longitudinal branch observed by the neutrons. A weak peak at 25 cm^{-1} has been quoted by Nakashima [23] for T=36 K, but its cause is very uncertain.[20] It would seem to be more likely due to a Raman active mode of 6 or 8H rather than the forbidden 4H.

In contrast to the deductions for the transverse branch, there is some discrepancy in the wave velocities for the longitudinal branch derived from different experiments;

v_l(neutron, 300 K) = 1.54 ($\pm$0.08) x 10^5 cm/s

v_l(Brillouin, 300 K) = 1.81 ($\pm$0.02) x 10^5 cm/s

v_l(ultrasonic at 15 MHz,[42] 300 K) = 1.755 ($\pm$0.01) x 10^5 cm/s.

We will discuss this further in Chapter 4.

3.2.2 Optical Branches

Figure 26 shows the optical dispersion curves of the 2H large zone of PbI_2. The T.O.1 branch is obtained from the neutron scattering experiments,[24] whereas the rest are

FIGURE 26

OPTICAL DISPERSION CURVES ALONG c-DIRECTION OF PbI_2

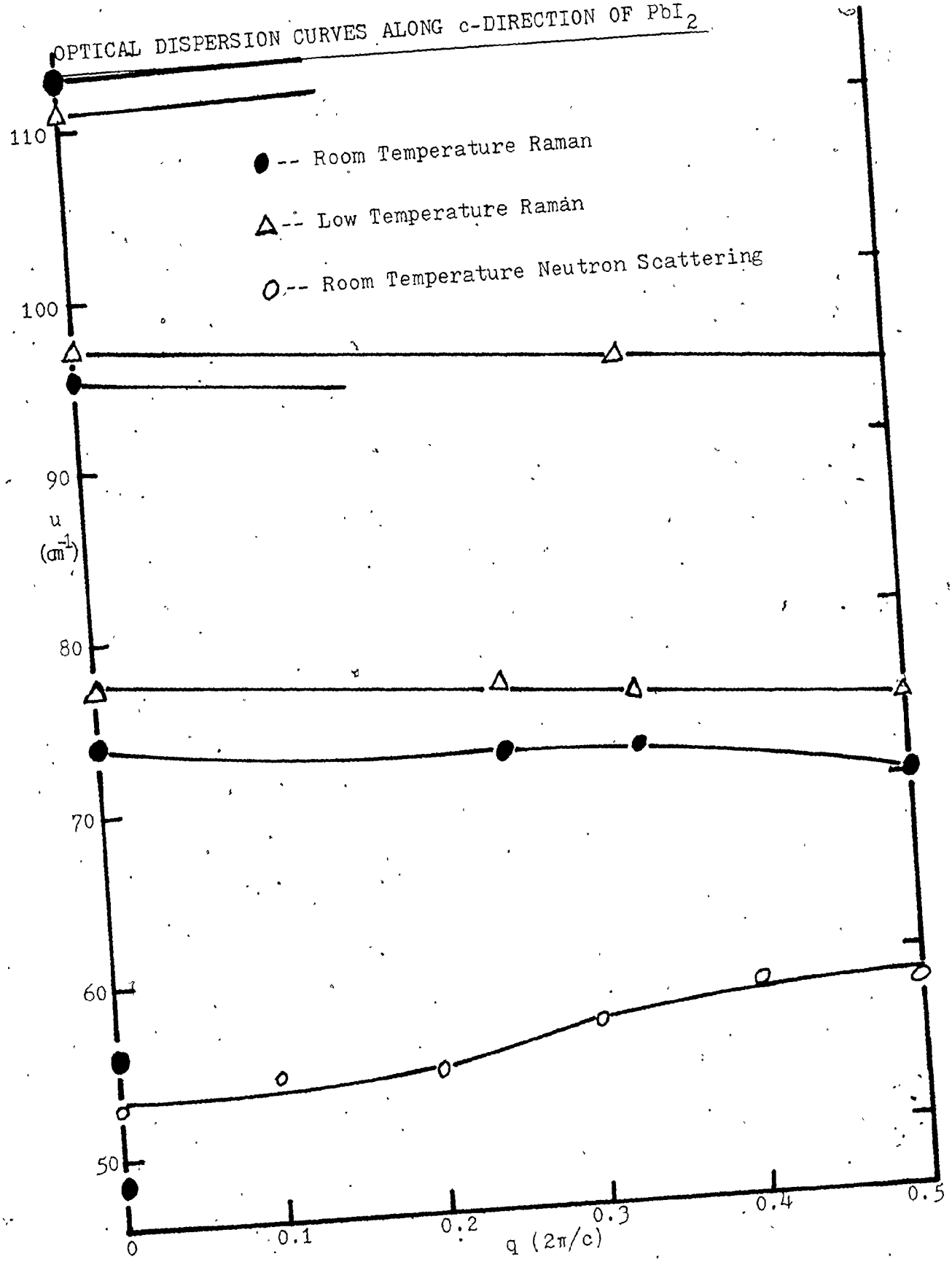

from the Raman modes of the various polytypes as given in section 3.1.

The Raman frequency of 53 cm^{-1} comes from the assignment of the peak at 106 cm^{-1} as being the first overtone. The peak at 48.5 cm^{-1} is a direct measurement from a 4H/12R crystal (400 K). Grisel and Schmid [7] observed this mode at 51 ($\pm$2) cm^{-1} (77 K) in a Raman experiment. Mon [21] observed a peak at 62 cm^{-1} in the infrared spectrum (room), Clasen et al (as quoted in reference 24) [43] at 60 ($\pm$3) cm^{-1} (room?), and Lucovsky et al [44] at 51.7 ($\pm$0.5) cm^{-1} (room?); this value is also quoted in reference 24. Despite the spread in these values, there is reasonable consistency with the neutron curve in Figure 26.

The T.O.2 branch is well defined by the Raman results as is its temperature dependence. Less information is obtained for the L.O.1 and L.O.2 branches but more information could be contained in the infrared spectra of the various polytypes. Mon [21] gives the frequencies 85, 100, and 117 cm^{-1} (no experimental errors are given) which can be correlated with the top three branches (room temperature) of Figure 26, though it should be noted that T.O.2 and L.O.2 are not infrared active in 2H PbI_2. Another frequency given by Mon at 128 cm^{-1} is probably an overtone of the mode at 62 cm^{-1}.

Infrared reflectivity measurements of Grisel and Schmid [7] give a transverse E_u mode at 52.5 ($\pm$1.5) cm^{-1} and

a longitudinal A_{2u} mode at about 110 cm^{-1}. These also agree with the T.O.1 and L.O.1 curves of Figure 26.

3.3 Heat Capacities at Low Temperatures

The measured heat capacities of the large crystal of PbI_2 are listed in Table 13. As is indicated in the next section, the thermal conductivity of the crystal was found to be surprisingly low. The resulting long equilibrium time introduced significant inaccuracy into the thermal measurements, as was described in section 2.3.3. The heat capacity of the copper tray determined in a separate experiment,[38] is given in the third column in Table 13.

The heat capacity data are plotted in Figure 27 in the form C_p/T^3 against T^2. This is a convenient form for the determination of the coefficients of the low temperature expansion:

$$C_p = a_1 T^3 + a_2 T^5 + \ldots\ldots \qquad (1)$$

that the heat capacity of simple insulators is expected to follow in the region approaching the continuum limit.[45]

The coefficient a_1 is well-defined as the intercept when $T^2 \to 0$ and, from the graph, we obtain

$$a_1 = 5.94\ (\pm 0.05)\ \text{mJ/K}^4\ \text{mol}.$$

This corresponds to a limiting Debye characteristic temperature at T=0 K. In particular,

$$\Theta_0^c = (12\pi^4 N K_B / 5a_1)^{1/3} \qquad (2)$$

where N = total number of atoms ($3N_A$ per mole for PbI_2), from which we obtain:

$$\Theta_0^c = 99.4\ (\pm 0.3)\ \text{K}.$$

TABLE 13

MEASURED HEAT CAPACITIES AT LOW TEMPERATURES

T (K)	Total C_p (mJ/K)	C_p of Tray (mJ/K)	C_p of PbI_2 Sample (mJ/K)	C_p of PbI_2 per mole (mJ/K mol)
0.494	0.180±0.002	0.089±0.002	0.091±0.004	0.743±0.033
0.514	0.193±0.004	0.092±0.002	0.101±0.006	0.824±0.049
0.619	0.282±0.004	0.112±0.002	0.170±0.006	1.39 ±0.05
0.821	0.557±0.009	0.155±0.002	0.402±0.012	3.28 ±0.10
0.844	0.598±0.008	0.161±0.002	0.437±0.010	3.57 ±0.08
1.055	1.08 ±0.02	0.22 ±0.002	0.86 ±0.02	7.02 ±0.16
1.094	1.18 ±0.01	0.24 ±0.002	0.94 ±0.02	7.67 ±0.16
1.360	2.14 ±0.02	0.28 ±0.003	1.86 ±0.03	15.2 ±0.2
1.628	3.54 ±0.06	0.35 ±0.004	3.19 ±0.06	26.0 ±0.5
1.688	3.87 ±0.04	0.37 ±0.004	3.50 ±0.05	28.6 ±0.4
1.904	5.50 ±0.14	0.45 ±0.005	5.05 ±0.15	41.2 ±1.2
1.972	6.16 ±0.11	0.48 ±0.005	5.68 ±0.12	46.4 ±1.0
2.159	8.07 ±0.21	0.56 ±0.006	7.51 ±0.22	61.3 ±1.8
2.228	8.97 ±0.18	0.59 ±0.006	8.38 ±0.18	68.4 ±1.5
2.478	12.7 ±0.4	0.72 ±0.007	12.0 ±0.4	97.9 ±3.3
2.758	19.1 ±1.2	0.89 ±0.02	18.2 ±1.2	149 ±10
3.039	26.6 ±2.3	1.1 ±0.02	25.5 ±2.3	208 ±19
3.322	36.6 ±5.3	1.3 ±0.03	35.3 ±5.3	288 ±43
3.601	50.5 ±11.3	1.6 ±0.03	48.9 ±11.3	399 ±92
3.874	59.2 ±15.0	1.9 ±0.04	57.3 ±15.0	468 ±122

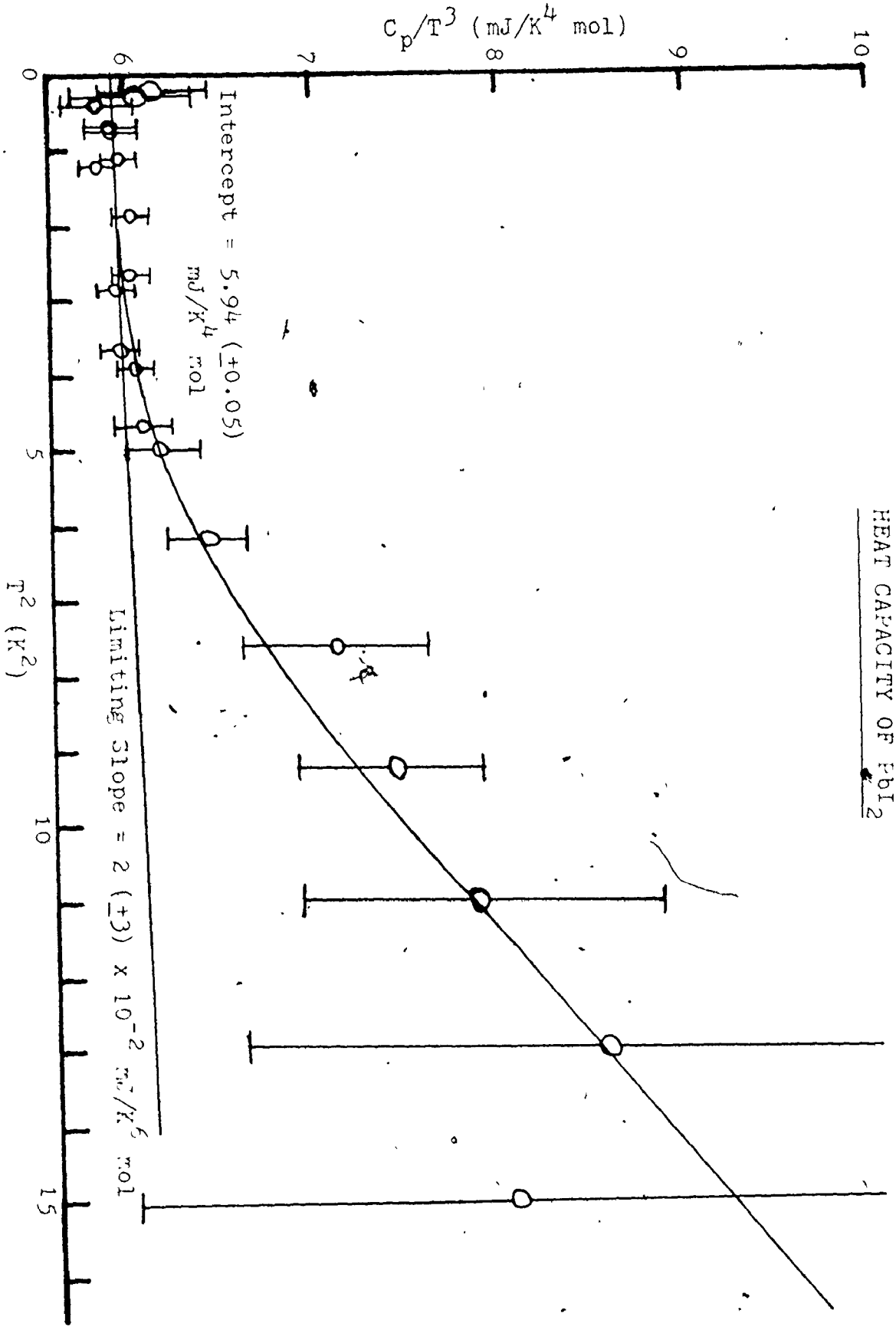

FIGURE 27

HEAT CAPACITY OF PbI_2

From a_1 or θ_0^c, we can also obtain the mean wave (or sound) velocity;

$$v_{av}^c = K_B \theta_0^c (4\pi V/3N)^{1/3}/\hbar \qquad (3)$$

where V is the volume of the sample (or volume per mole). Using an estimated density for PbI_2 at T=0 K (see section 3.5);

$$V = M_{PbI_2}/\rho = 461 \text{ amu}/6.23 \text{ g/cm}^3 = 74.0 \text{ cm}^3/\text{mol}. \qquad (4)$$

$N = 3N_A$ as before and therefore;

$$v_{av}^c = 1.151\ (\pm 0.005) \times 10^5 \text{ cm/s}.$$

We also obtain some information about dispersion of the lattice waves from the heat capacity data. The coefficient of the T^5 term in equation (1) should indicate how the acoustical branches of the phonon dispersion curves begin to deviate (on average) from linearity at low energies. Figure 27 gives a value of a_2, obtained from the limiting slope, of:

$$a_2 = 2\ (\pm 3) \times 10^{-2} \text{ mJ/K}^6 \text{ mol}.$$

We see that, within the limits assigned, a_2 could be zero or negative, in which case PbI_2 would be showing a feature of 2-dimensional structures such as graphite:[1] negative dispersion in some crystallographic directions. More accurate measurements are needed before more can be said about this test of 2-dimensionality.

To compare the properties of PbI_2 with those of other crystals, we can conveniently use the expansion

$$C_p = a_1'(T/\theta_0^c)^3 + a_2'(T/\theta_0^c)^5 + \ldots\ldots, \qquad (5)$$

where $a_1' = a_1(\theta_0^c)^3$ and $a_2' = a_2(\theta_0^c)^5$. For PbI_2,

$a_1' = 5.83\ (\pm 0.10) \times 10^3$ J/K mol

$a_2' = 2\ (\pm 3) \times 10^5$ J/K mol.

To compare with PbI_2, we choose MgO for which data of good accuracy are available:[46]

$\theta_0^c = 946\ (\pm 4)$ K

$a_1 = 4.588\ (\pm 0.059) \times 10^{-3}$ mJ/K^4 mol

$a_2 = 3.6\ (\pm 0.8) \times 10^{-7}$ mJ/K^6 mol,

from which we obtain

$a_1' = 3.88\ (\pm 0.10) \times 10^3$ J/K mol

$a_2' = 2.7\ (\pm 0.7) \times 10^5$ J/K mol.

The normalized coefficients of MgO and PbI_2 are similar and this is further emphasized by Figure 28 where $(C_p/T^3)/(C_p/T^3)_{T=0}$ is plotted against $(T/\theta_0^c)^2$.

FIGURE 28

COMPARISON OF HEAT CAPACITIES OF PbI_2 AND MgO ON A NORMALIZED SCALE

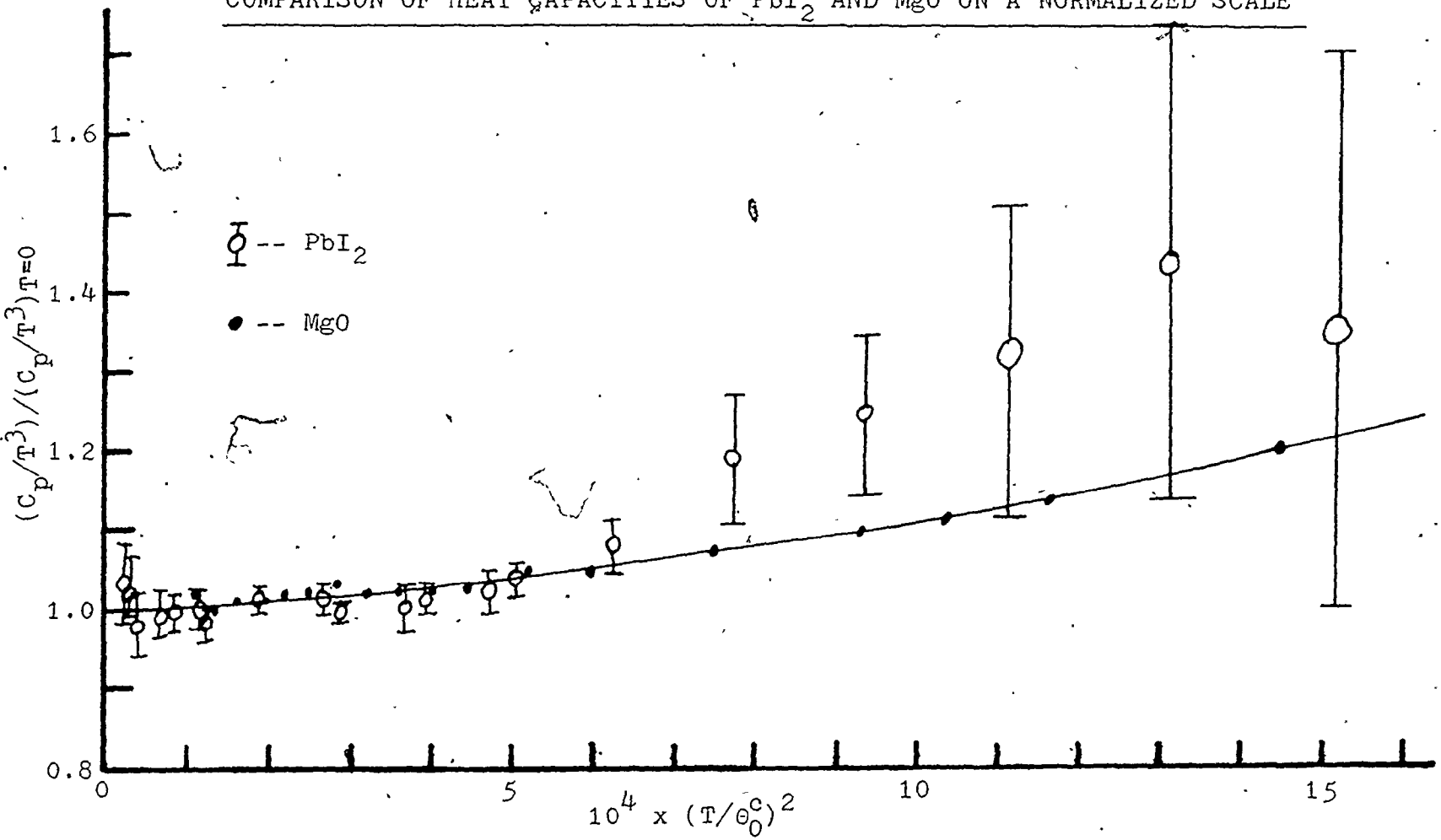

3.4 Thermal Conductivity of PbI_2

3.4.1 General Remarks

Thermal conduction of a solid can be determined with the tray-type calorimeter used here, provided that the thermal equilibration time of the specimen is neither too large nor too small. For the PbI_2 specimen, the equilibration time turned out to be in a convenient range. As is depicted in Figure 6 or 29 the markedly curved after drift of temperature versus time occurred over the convenient interval of the order of 5 minutes. Measurements of temperature could be made at intervals of 10 seconds so that the rate of equilibration could be measured comfortably.

3.4.2 Determination of the Thermal Conductivity

The solution to the heat conduction problem for a "slab with one face in contact with a layer of perfect conductor" is given by Carslaw and Jaeger (page 128 of reference 47). The initial conditions that apply after the heat pulse, given that the copper tray equilibrates instantaneously, are: no energy transfer other than from the perfect conductor; initial temperature of the tray taken as T_o with respect to the temperature of the PbI_2 crystal defined as T=0 at t=0. The equation that describes the variation of the temperature of the copper tray with time is (equation 3.13-6 of reference 47):

FIGURE 29

SAMPLE DECAY CURVE OF HEAT CAPACITY MEASUREMENTS IN PbI_2

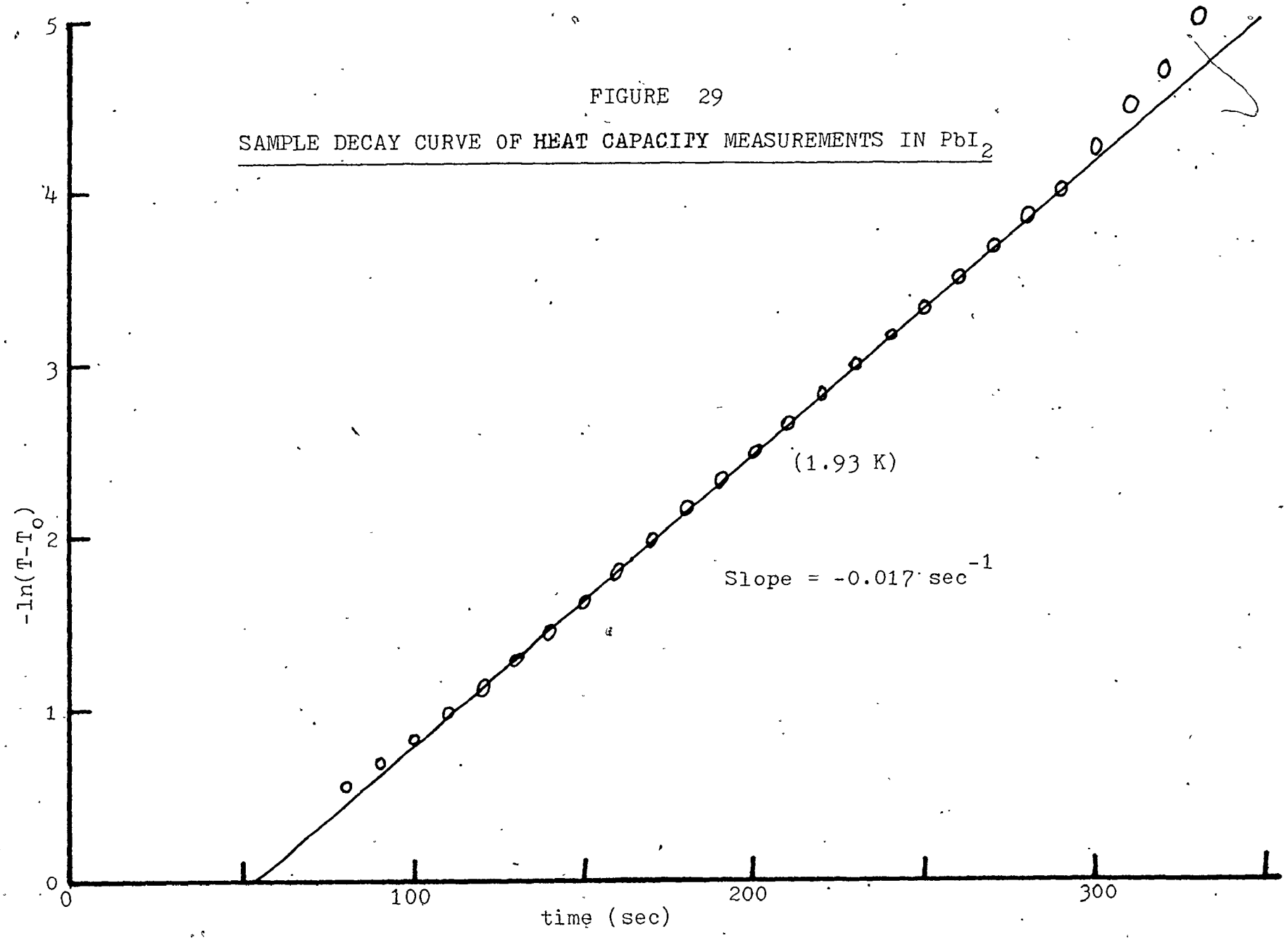

$$T = \frac{T_o}{1+\ell r} + \sum_{n=2}^{\infty} \frac{2rT_o \exp(-d\beta_n^2 t)}{\ell(\beta_n^2 + r^2) + r} \quad (6)$$

Here, ℓ is the height of the slab which, in the case of the PbI_2 specimen, is not well-defined because of the odd shape of one end of the specimen. An average ℓ of 3 cm was taken and this was adequate for the calculations. The parameter r is given by

$$r = \rho A C_p / M C_p', \quad (7)$$

where ρ is the density of PbI_2 at low temperatures (about 6.23 g/cm^3), A is the surface area of the crystal in contact with the tray (3.63 cm^2), C_p and C_p' are the heat capacities (as a function of temperature) of the PbI_2 crystal and the copper tray respectively, and M is the mass of the crystal specimen (56.48 g). In the exponent, d is the thermal diffusivity and the β_n are the roots of the equation:

$$\tan(\beta\ell) = -\beta/r. \quad (8)$$

Referring to equation (6), we note that it contains an infinite series of exponentials. However, the contribution of each of them decreases rapidly for successive roots of equation (8). In calculating the relative sizes of successive exponentials, we will take two extreme cases: T=0.6 K and T=4.2 K. This leads to (from equation (7)) r=0.4 cm^{-1} and r=12 cm^{-1}. For the two cases, the first three roots of equation (8) are;

	T=0.6 K	T=4.2 K
	$\beta_1 = 0$	$\beta_1 = 0$
	$\beta_2 = 0.7$	$\beta_2 = 1.0$
	$\beta_3 = 1.6$	$\beta_3 = 2.0$

The denominator in the terms in the summation in equation (6) becomes for β_2 and β_3:

	T=0.6 K	T=4.2 K
$\ell(\beta_2^2 + r^2) + r =$	2.3	438
$\ell(\beta_3^2 + r^2) + r =$	9.0	448.

The change is a factor of 4 at the lower temperature but almost insignificant at the higher temperature.

If we examine the exponential, we see that:

$$\exp(-d\beta_n^2 t) = (\exp(-|\beta_n^2|))^{|dt|},$$

where

	T=0.6 K	T=4.2 K
$\exp(-\|\beta_2^2\|) =$	0.6	0.35
$\exp(-\|\beta_3^2\|) =$	0.07	0.02.

For $|dt|$ greater than one, the changes in the numerator and denominator yield minimum ratio of the terms in β_2 and β_3 of 34 at T=0.6 K and 18 at T=4.2 K. This means that, if we restrict our analysis to times such that $|dt|$ is greater than one (i,e. t greater than 100 seconds), we can truncate the series in equation (6) without significant error after the term in β_2. Equation (6) then reduces to:

$$T = \frac{T_o}{1+\ell r} + \frac{2rT_o}{\ell(\beta_2^2 + r^2) + r} \exp(-d\beta_2^2 t). \qquad (9)$$

Letting $T' = T - T_o/(1+\ell r)$ and $A_o = 2rT_o/(\ell(\beta_2^2 + r^2) + r)$, we have

$$T' = A_o \exp(-d\beta_2^2 t), \tag{10}$$

where T' can be calculated from the measurements of T versus t by observing that, at $t=\infty$, $T'=0$. The determination of the point at t=0 is of little importance because the constant A_o is not used subsequently.

Therefore, by plotting $\ln|T'|$ versus t, we can obtain $d\beta_2^2$ from the slope (see Figure 29). In the figure, the initial deviation from the straight line is easily seen. The deviation at long times is due to the small energy exchange between the calorimeter and surroundings through the thin Nylon suspension cords and electrical leads.

3.4.3. Numerical Results

The quantity $d\beta_2^2$ is the equilibration time constant listed in Table 14. Knowing the heat capacities as functions of temperature (Table 13) we can easily calculate β_2 for each experiment (ρ, A and ℓ are assumed to be constant). This allows us to calculate d and the results are given in the second column of Table 14.

The thermal conductivity is defined as

$$\kappa = d\rho C_p/M, \tag{11}$$

and the numerical values are given in the fourth column.

Within the framework of the Debye model, the thermal conductivity of a dielectric solid is given by

TABLE 14

MEASURED THERMAL CONDUCTIVITIES AT LOW TEMPERATURES

T (K)	$10^2 \times d\beta_2^2$ (sec^{-1})	$10^2 \times d$ (cm^2/s)	$10^6 \times \kappa$ (w/cm K)	ℓ_m (A)
0.60	0.94	1.68	0.30±0.08	44
0.62	1.31	2.28	0.46±0.12	59
0.73	1.13	1.77	0.56±0.14	46
0.94	1.50	2.05	1.40±0.28	53
0.98	1.13	1.54	1.20±0.24	40
1.18	1.16	1.44	1.96±0.39	38
1.25	1.13	1.37	2.20±0.37	36
1.51	1.33	1.47	4.12±0.70	38
1.82	1.60	1.69	8.34±1.50	44
1.93	1.70	1.78	10.4±1.9	46
2.06	1.65	1.71	12.3±2.2	45
2.19	1.54	1.57	13.5±2.4	41
2.34	1.38	1.40	15.0±2.6	36
2.44	1.39	1.40	17.5±2.6	36
2.65	1.17	1.16	20.2±3.0	30
3.07	1.21	1.18	35.1±5.3	31
3.32	1.07	1.04	41.3±7.8	27
3.79	0.90	0.87	53.4±13.4	23
3.98	0.94	0.90	66.0±19.8	23
4.21	0.85	0.81	71.3±21.4	21

The estimated uncertainties in $d\beta_2^2$, d, and ℓ_m are ±10%.

$$\kappa = \rho C_p v_{av}^c \ell_m / 3M, \qquad (12)$$

where ℓ_m is the phonon mean free path and v_{av}^c is the average phonon velocity. If we take $v_{av}^c = 1.151\ (\pm 0.005) \times 10^5$ cm/s from the heat capacity measurements, we get the values of ℓ_m given in the last column of Table 14.

Figure 30 is a plot of the thermal conductivity in the form of κ/T versus T^2. This shows that for T less than 3K, the thermal conductivity follows the heat capacity in displaying a T^3 temperature dependence. Such behavior is consistent with the Debye model. More sensitive ways of displaying the results are given in Figure 31 (ℓ_m versus T) and Figure 32 (ℓ_m versus 1/T). The latter shows that, in the higher temperature region, there is a T^{-1} dependence which would be expected for phonon-phonon scattering. At lower temperatures, this scattering is overwhelmed by some sort of boundary or resonant scattering. In general, this is what would be expected except that the magnitude of the calculated mean free path is much less than the dimensions of the crystal specimen or even of its probable mosaic substructure.

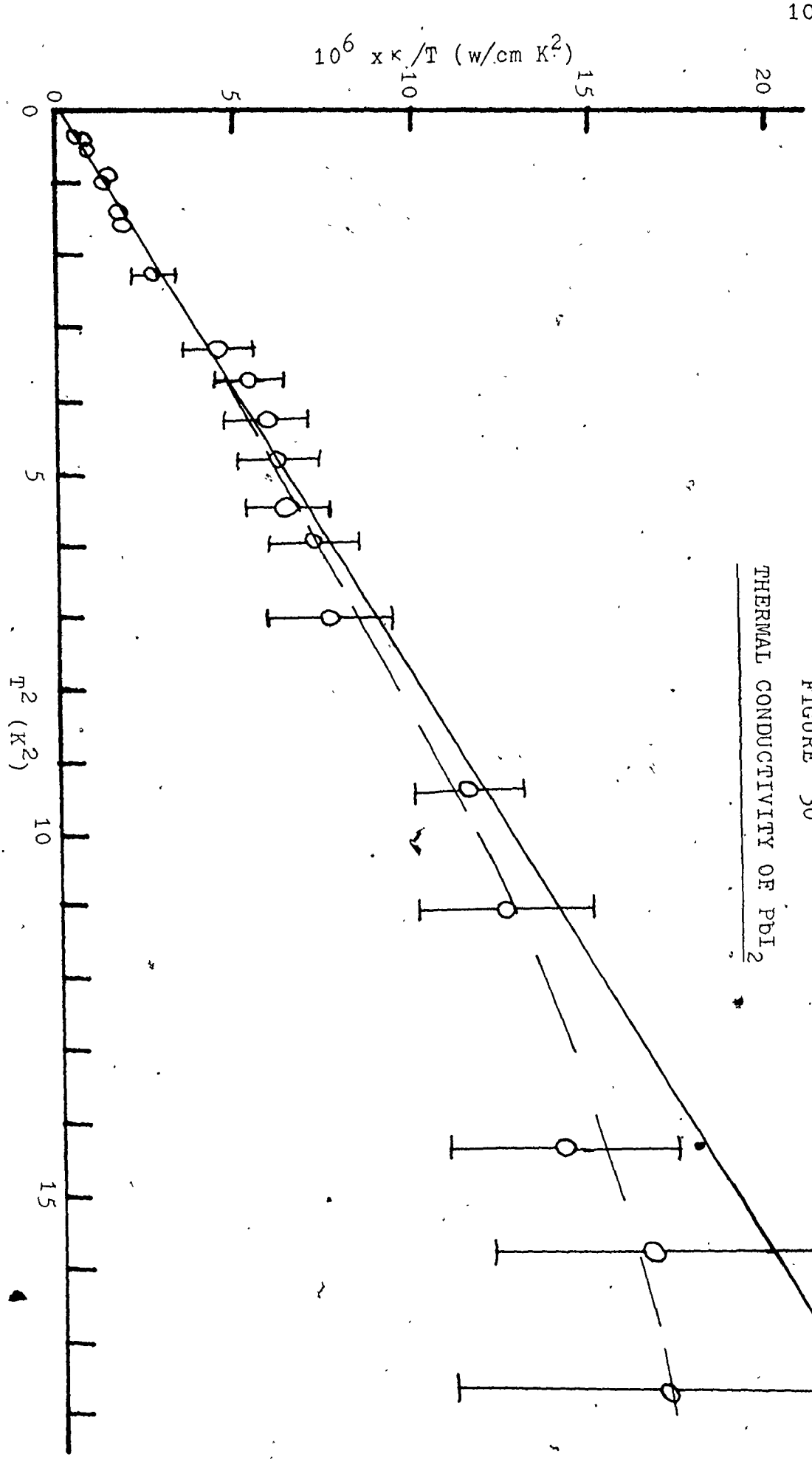

FIGURE 30

THERMAL CONDUCTIVITY OF PbI_2

FIGURE 31

MEAN FREE PATH OF PbI_2

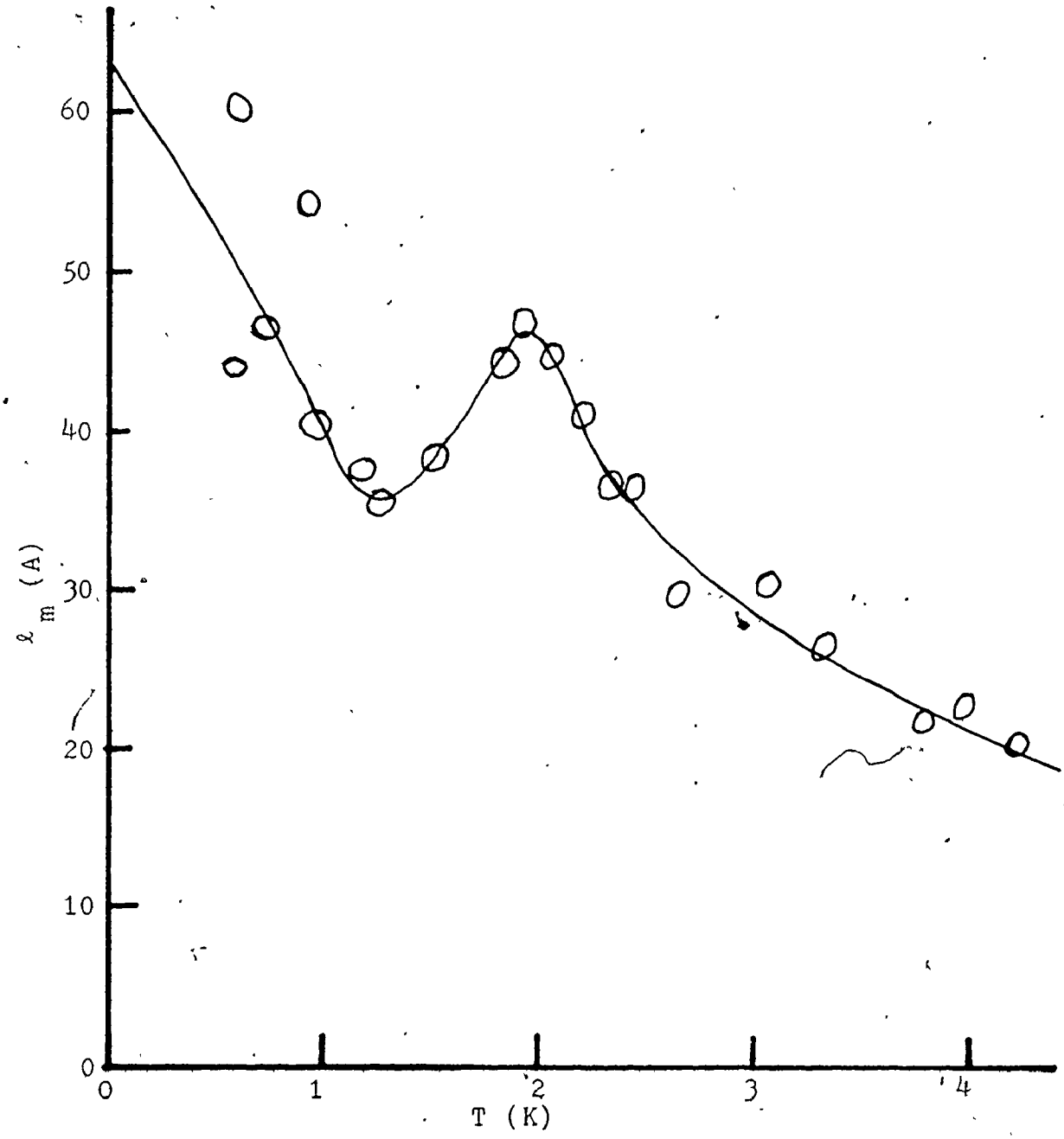

FIGURE 32

MEAN FREE PATH OF PbI_2

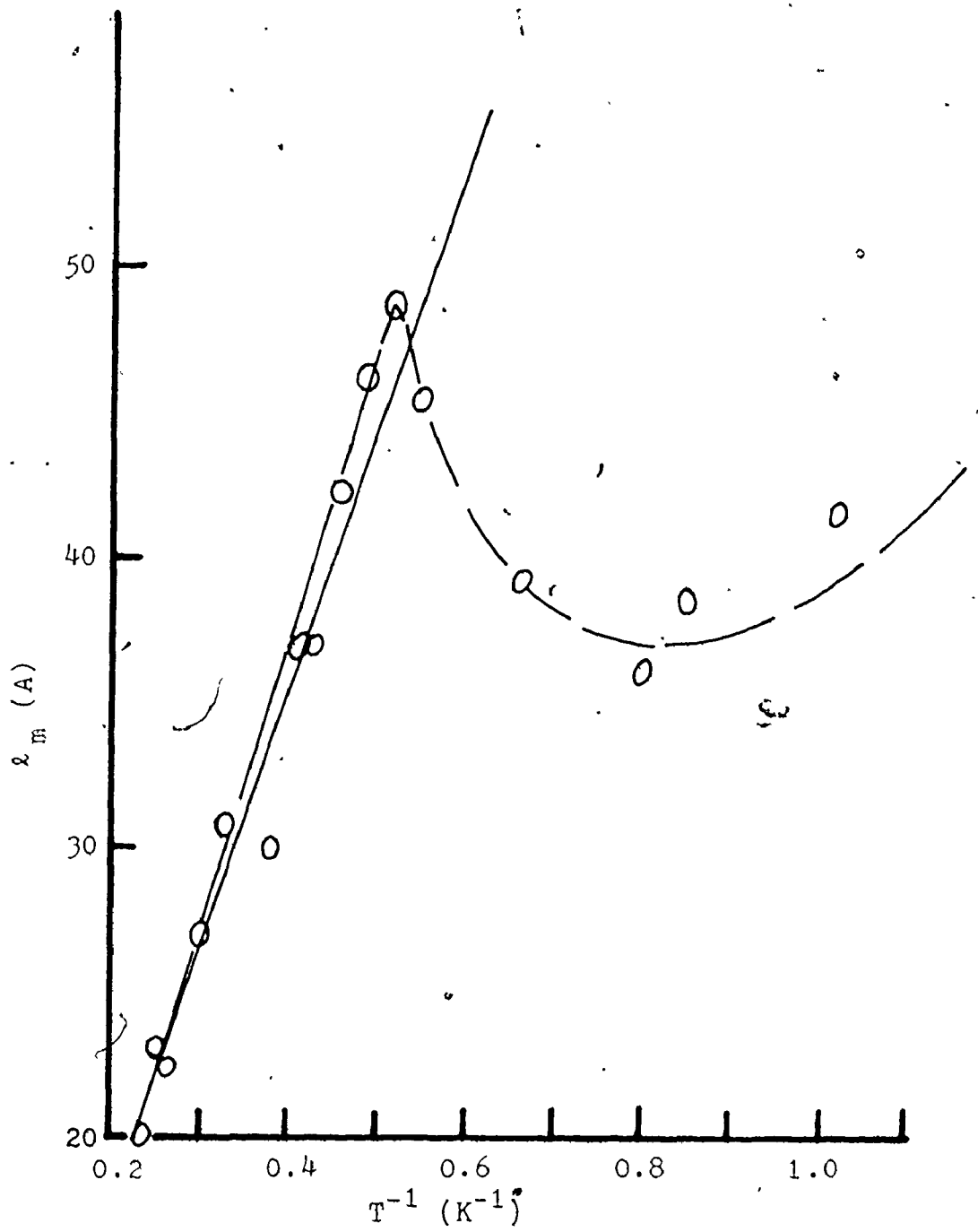

3.5 Thermal Expansion

The lattice parameters (a,c) of polytype 2H as measured as a function of temperature by the technique described in section 2.4, are presented in Table 15. The uncertainties shown reflect the precision of the measurements more than the accuracy. The lattice parameters given in Wyckoff [39] for room temperature are a = 4.557 Å and c = 6.979 Å and these agree well with the values a = 4.5562 (±0.0004) Å and c = 6.9830 (±0.0004) Å obtained by Sirdeshnakh and Deshpande.[48] The results for both a and c given in Table 15 for T = 293 K are appreciably smaller and the difference is probably ascribable to the centering difficulty mentioned in section 2.4.2.

In order to discuss the thermal expansion, the lattice parameters given in Table 15 were shifted by $\Delta a = 0.008$ Å and $\Delta c = 0.032$ Å. They are compared on this basis with the results of Sirdeshnakh and Deshpande as a function of temperature in Figures 33 and 34. It is clear that the temperature dependence of the two sets of measurements agree very nicely.

From Figure 33, we see that the contraction of the PbI_2 layers in the c-direction is linearly dependent upon T down to the lowest experimental temperature. The slope of the graph is 2.5 (±0.1) x 10^{-4} Å/K. The corresponding average expansivity is $(c^{-1}dc/dT) = 3.6\ (\pm 0.1) \times 10^{-5}/K$.

Along the a-direction, on the other hand, the expansivity departs from a constant value, at low temperatures, as clearly seen in Figure 34. The average high temperature expansivity is $(a^{-1}da/dT) = 4.0\ (\pm 0.1) \times 10^{-5}/K$, which is derived from the straight line in the figure of slope $1.80\ (\pm 0.05) \times 10^{-4}$ Å/K.

From these results, we calculate a room temperature volume expansivity of PbI_2 of $1.16\ (\pm 0.03) \times 10^{-4}/K$. This result can be compared with the values of $1.008 \times 10^{-4}/K$ and $1.086 \times 10^{-4}/K$ reported by Fizeau [49] and Klemn et al [50] respectively.

TABLE 15

LATTICE PARAMETERS OF PbI_2 (2H)

T (K)	a (Å) ±0.003	c (Å) ±0.016
102	4.524	6.899
121	4.525	6.908
140	4.526	6.914
162	4.527	6.913
187	4.531	6.923
215	4.534	6.930
244	4.538	6.937
276	4.543	6.944
293	4.547	6.946

FIGURE 33

LATTICE PARAMETER OF PbI_2 IN c-DIRECTION AS A FUNCTION OF TEMPERATURE

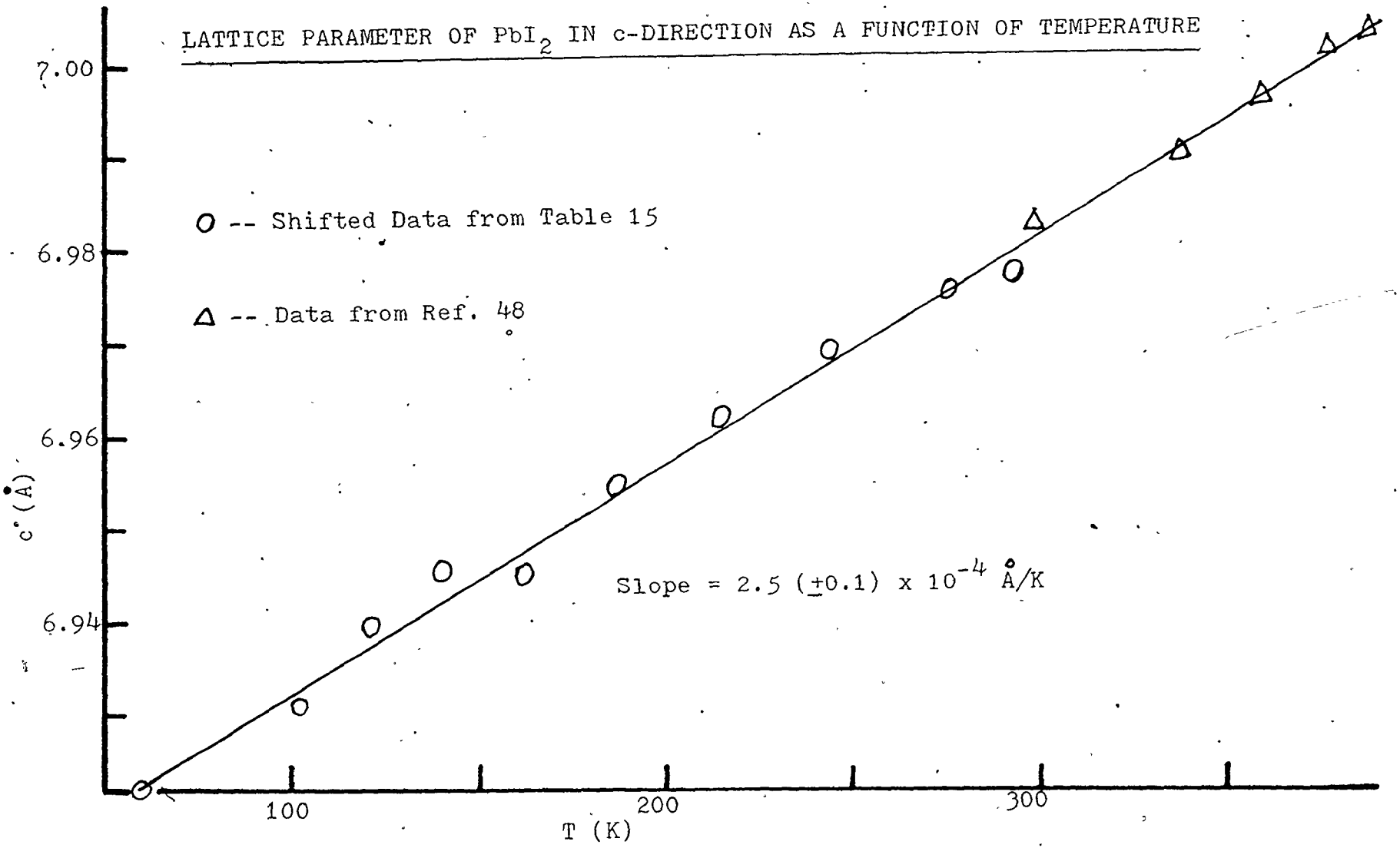

FIGURE 34

LATTICE PARAMETER OF PbI_2 IN a-DIRECTION AS A FUNCTION OF TEMPERATURE

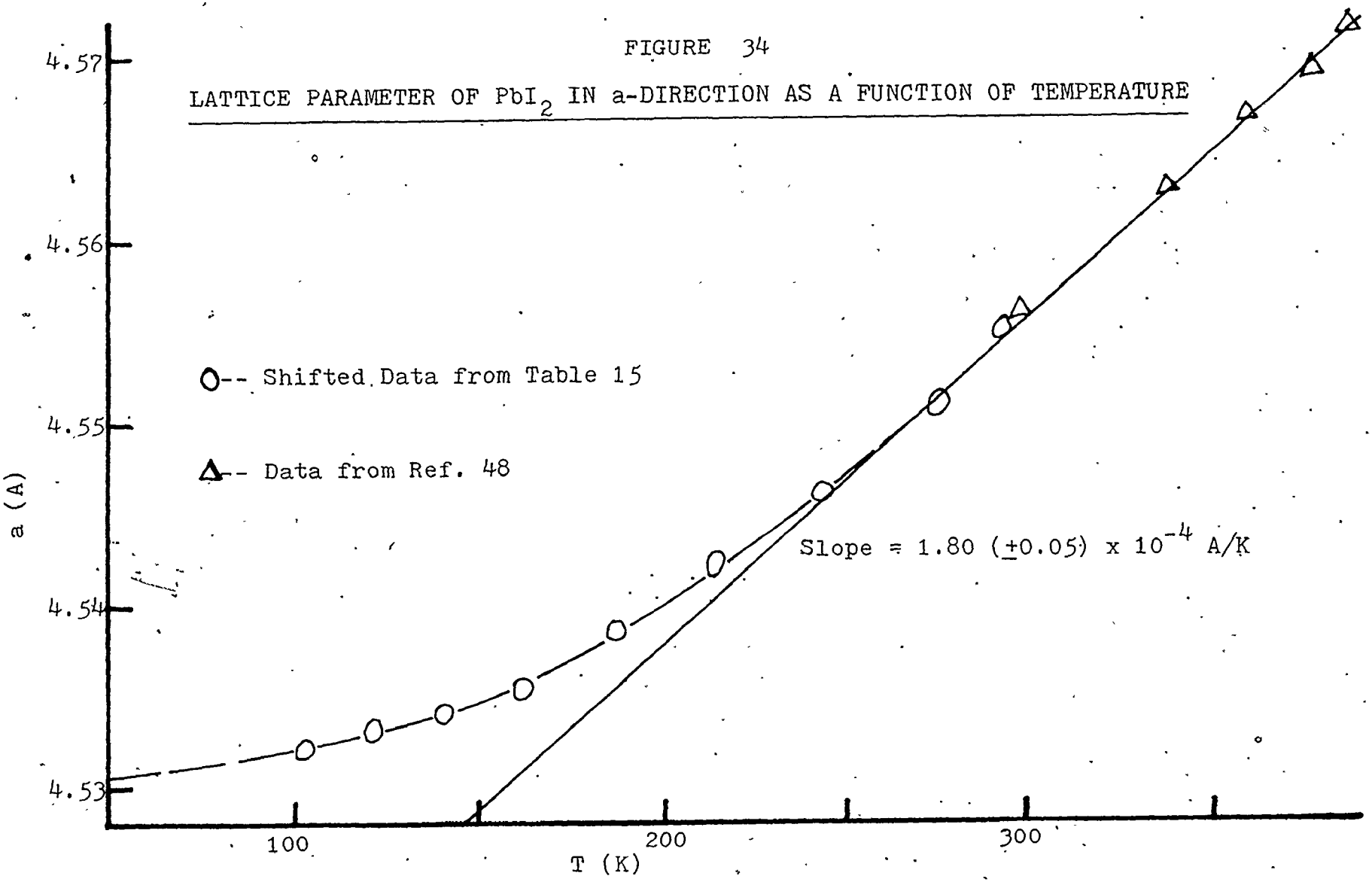

CHAPTER 4

DISCUSSION

4.1 A Vibrational Model for PbI_2

4.1.1 Calculation of Force Constants

With a linear chain model of the type described by Anderson and Todoeschuck [26] for the layered crystals $FeCl_2$ and $CoCl_2$, six force constants can be fitted to the frequencies measured by the Raman, infrared, and neutron scattering experiments. The force constants involved (three shear and three compressional) are illustrated in Figure 35. The normal modes corresponding to this rigid layer model are identified in Figure 36.

Writing down the equations of motion for these modes, we obtain;

$$M\ddot{Z}_o = -K_o(Z_o-Z_{-1}) - K_o(Z_o-Z_1) \quad (13)$$

$$m\ddot{Z}_1 = -K_o(Z_1-Z_o) - K_2(Z_1-Z_{-1}) - K_1(Z_1-Z_2) \quad (14)$$

$$m\ddot{Z}_{-1} = -K_o(Z_{-1}-Z_o) - K_2(Z_{-1}-Z_1) - K_1(Z_{-1}-Z_{-2}) \quad (15)$$

where M = mass of lead atom, m = mass of iodine atom, and Z_n = layer displacement in the Z-direction at layer n for compressional modes; in X-direction for shear modes.

For plane waves, we have:

$$Z_o = A_1 \exp i(wt) \quad (16)$$

$$Z_1 = A_2 \exp i(wt-qc') \quad (17)$$

$$Z_{-1} = A_3 \exp i(wt+qc') \quad (18)$$

FIGURE 35

INTERLAYER FORCE CONSTANTS FOR PbI_2

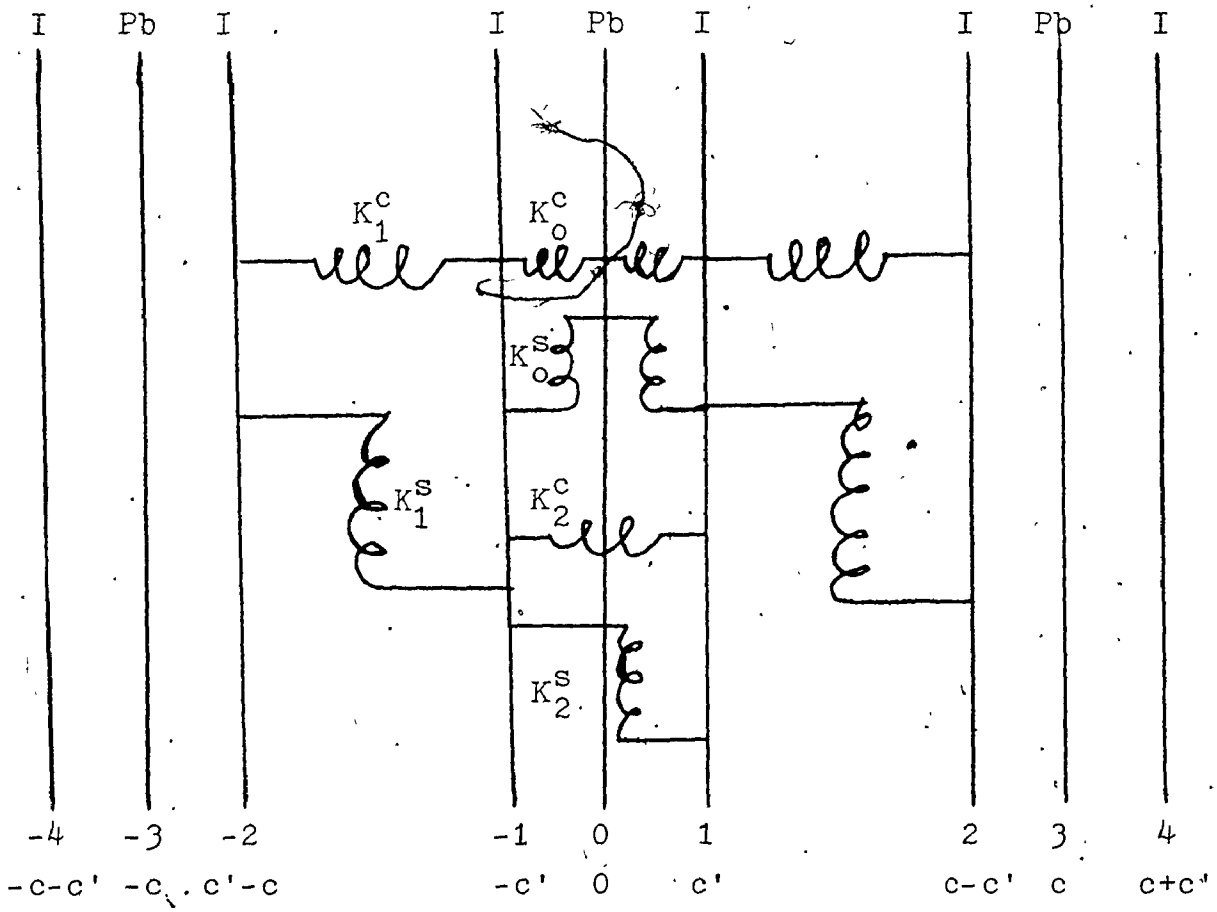

FIGURE 36

COMPRESSIONAL* RIGID LAYER NORMAL MODES OF PbI_2

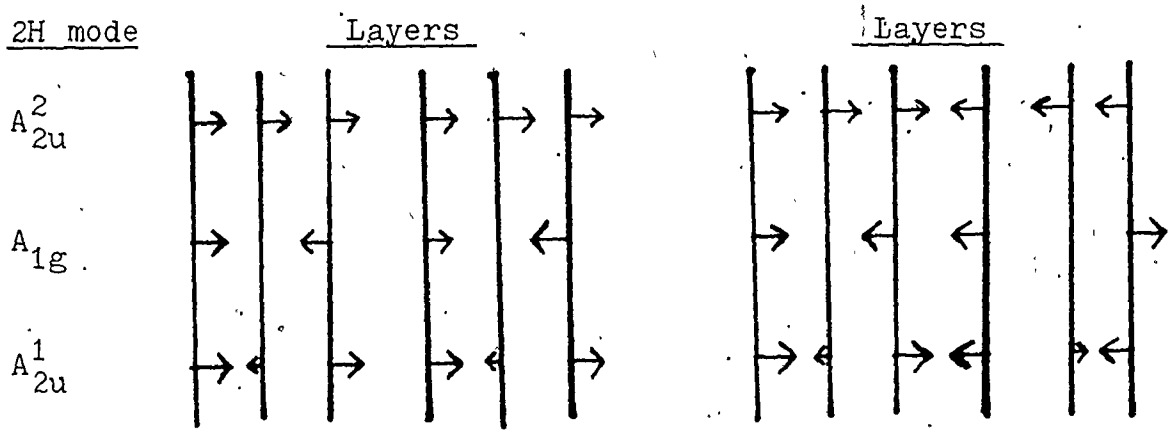

* A similar array can be identified for the doubly-degenerate shear modes (E_u^2, E_g, E_u^1) that are perpendicular.

$$Z_2 = A_3 \exp i(wt-q(c-c')) \quad (19)$$

$$Z_{-2} = A_2 \exp i(wt+q(c-c')). \quad (20)$$

Solving for the secular equation, we obtain:

$$\begin{vmatrix} Mw^2-2K_o & K_o & K_o \\ K_o & mw^2-K_o-K_2-K_1 & K_2 + K_1 \exp i(-qc) \\ K_o & K_2 + K_1 \exp i(qc) & mw^2-K_o-K_2-K_1 \end{vmatrix} = 0 \quad (21)$$

which leads to an equation, cubic in w^2:

$$w^6(Mm^2) + w^4(-2m(K_o(M+m)+(K_2+K_1)M)) + w^2((K_o^2+2K_oK_2+2K_oK_1)(M+2m)+2K_2K_1M(1-\text{Cos}(qc))) + 2K_oK_1(K_o+2K_2)(\text{Cos}(qc)-1) = 0.$$

We shall consider two special cases; the first at $q=0$, where $1-\text{Cos}(qc) = 0$, and the cubic equation can be factored into the solutions:

$$w_1^2 = 0 \quad (23)$$

$$w_2^2 = (K_o + 2(K_2+K_1))/m \quad (24)$$

and $w_3^2 = K_o(M+2m)/Mm.$ (25)

Substituting back into equations (13), (14) and (15), we see that w_1 corresponds to $A_1=A_2=A_3$ which gives the acoustic modes A_{2u}^2 or E_u^2. Likewise for w_2, we obtain $A_1=0$ and $A_2=A_3$ which from Figure 36, corresponds to the Raman modes A_{1g} or E_g. Finally for w_3, we see that $A_2=A_3= -A_1(M/2m)$ which gives the infrared modes A_{2u}^1 or E_u^1.

The second case of special interest occurs at $q=\pi/c$, where $1-\text{Cos}(qc) = 2$, and the cubic equation can be partially factored into:

$$\bar{w}_2^2 = (K_o + 2K_2)/m \quad (26)$$

$$\text{and } \bar{w}^2_{3,1} = \frac{K_o(M+2m) + 2K_1M \pm (K_o^2(M+2m)^2 + 4K_oK_1M(M-2m) + 4K_1^2M^2)^{\frac{1}{2}}}{2Mm} \quad (27)$$

If $\bar{w}_3^2 >> \bar{w}_1^2$, it can easily be seen that the last equation reduces to:

$$\bar{w}_3^2 \simeq (K_o(M+2m) + 2K_1M)/Mm \quad (28)$$

$$\text{and } \bar{w}_1^2 \simeq 4K_oK_1/(K_o(M+2m)+2K_1M). \quad (29)$$

These can be related to the zone edge normal modes as was done for q=0. The subscripts show the correspondance that must pertain across the zone.

For w_1 and w_3, we have $A_2 = \exp(2\pi c'/c)A_3$ and $A_1 = -(mw^2-K_o-2K_1)A_2/(K_o\exp(\pi c'/c))$. This can be written approximately as $A_1 \simeq A_2/\exp(\pi c'/c)$ for w_1 and $A_1 \simeq -2mA_2/(M \exp(\pi c'/c))$ for w_3. For w_2 we have $A_1 = 0$ and $A_2 = -\exp(2\pi c'/c)A_3$. This differs somewhat from the completely antiphase modes shown in Figure 36.

Equations (24), (25), (26), (28) and (29) represent five equations in three unknowns: K_o, K_2 and K_1. As the splitting of modes across the zone is the most prone to error it is best to use three independent equations to calculate the force constants: w_3, w_2 or $\bar{w}_2$, and $\bar{w}_1$. The last equation can be solved by iteration for K_1, once K_o is known, to obtain an accurate value. Once the force constants have been determined, the full cubic equation can easily be solved for any point on the dispersion curves in the c-direction.

Table 16 shows the calculated force constants and

the frequencies used in their computation. The room temperature values were obtained from the Raman and neutron results outlined in Chapter 3. The low temperature values were obtained from the Raman spectra with the exception of $\bar{u}_1^c$ and u_3^s which were estimated from the room temperature values. This proved to be a more accurate method than using the observed splitting of the Raman active modes.

The interlayer force constant (K_1) is the weakest as is to be expected - especially for shear motion. It is to be especially noted, however, that the anion-anion force constant is stronger than the anion-cation one in the shear direction within the layer.

Figures 37 and 38 show the dispersion curves calculated from the force constants of Table 16, along with data points from the Raman and neutron scattering experiments. The fit is reasonably good cosidering the simplicity of the model. The only point that is disturbingly off is the observation at a frequency of 95.1 cm^{-1} made on a 6H polytype. The apparent reversal with temperature of the L.O.1 branch may only be due to the uncertainty of the room temperature Raman measurement at 113 cm^{-1}.

TABLE 16

CALCULATED FORCE CONSTANTS

Frequencies	Force Constants
Compressional (Room)	
$u_3^c = 113\ (\pm 1)\ cm^{-1}$	$K_o^c = 43\ (\pm 1)\ N/m$
$u_2^c = 95.5\ (\pm 0.5)\ cm^{-1}$	$K_2^c = 6.6\ (\pm 1)\ N/m$
$\bar{u}_1^c = 29\ (\pm 2)\ cm^{-1}$	$K_1^c = 6.1\ (\pm 1)\ N/m$
Shear (Room)	
$u_3^s = 53\ (\pm 3)\ cm^{-1}$	$K_o^s = 9.4\ (\pm 1)\ N/m$
$u_2^s = 74\ (\pm 0.5)\ cm^{-1}$	$K_2^s = 14.4\ (\pm 0.5)\ N/m$
$u_1^s = 13.6\ (\pm 0.2)\ cm^{-1}$	$K_1^s = 1.33\ (\pm 0.05)\ N/m$
Compressional (T=50 K)	
$u_3^c = 111.1\ (\pm 0.5)\ cm^{-1}$	$K_o^c = 41\ (\pm 0.5)\ N/m$
$u_2^c = 97.3\ (\pm 0.2)\ cm^{-1}$	$K_2^c = 7.6\ (\pm 1)\ N/m$
$\bar{u}_1^c = 31\ (\pm 3)\ cm^{-1}$	$K_1^c = 7.0\ (\pm 1)\ N/m$
Shear (T=50 K)	
$u_3^s = 59\ (\pm 3)\ cm^{-1}$	$K_o^s = 11.7\ (\pm 1)\ N/m$
$u_2^s = 78.1\ (\pm 0.2)\ cm^{-1}$	$K_2^s = 15.3\ (\pm 0.3)\ N/m$
$\bar{u}_1^s = 15.2\ (\pm 0.2)\ cm^{-1}$	$K_1^s = 1.67\ (\pm 0.05)\ N/m$

FIGURE 37

CALCULATED DISPERSION CURVES OF PbI_2

(ACOUSTIC)

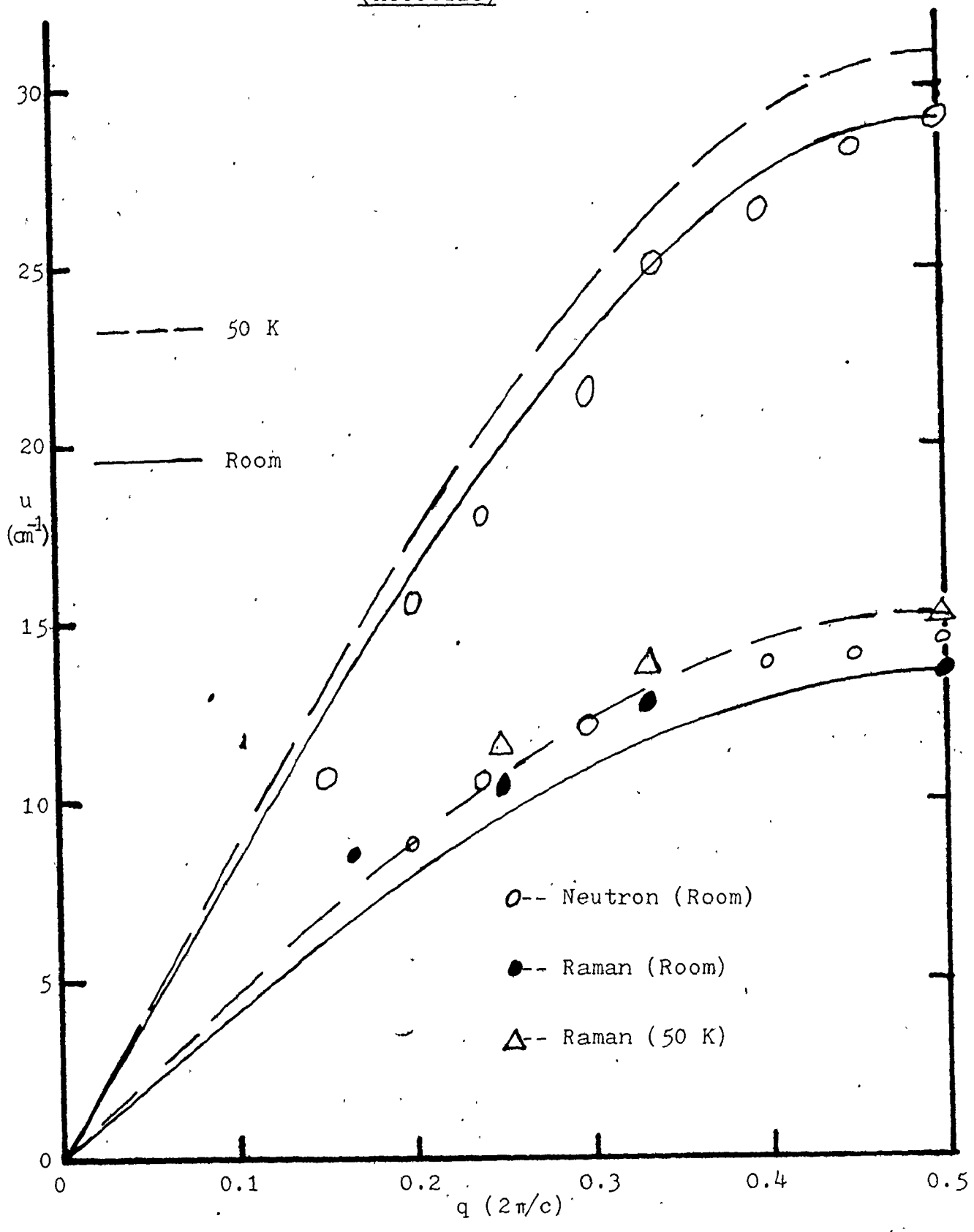

FIGURE 38

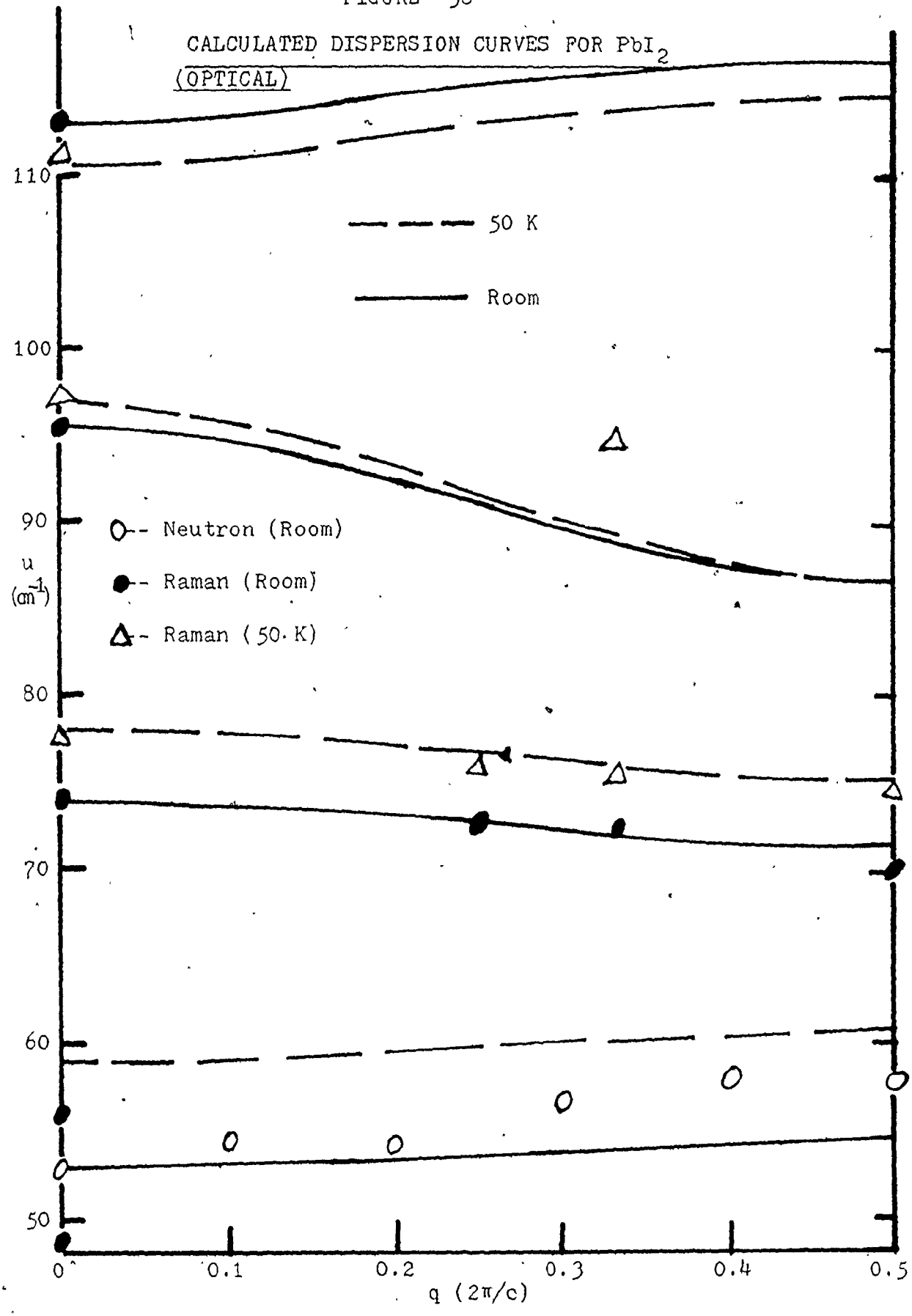
CALCULATED DISPERSION CURVES FOR PbI_2
(OPTICAL)
110
100
90
80
70
60
50
50 K
Room
Neutron (Room)
Raman (Room)
Raman (50 K)
u
(cm^{-1})
0
0.1
0.2
0.3
0.4
0.5
q (2π/c)

4.1.2 Comparison of Results

A useful quantity for comparing the properties of PbI_2 with those of other layered crystals is the ratio K_1^s/K_o^c, which has the value of 0.031 ($\pm$0.002) at room temperatures and 0.041 ($\pm$0.002) at T=50 K. This compares to values calculated by Zallen and Slade [20] of 0.035, by Grisel and Schmid [7] of 0.02 and by Nakashima [23] of 0.05. The last is based on an incorrect assignment of the E_2^3 rigid layer mode, however.

Table 17 shows a comparison of the above ratio and of K_1^c/K_o^c to those of other layered compounds. There is a fairly regular progression from graphite to PbI_2 and we might conclude that PbI_2 is considerably less layer like than graphite.

Table 18 shows a detailed comparison of the force constants calculated by Anderson and Todoeschuck [26] for $FeCl_2$ and $CoCl_2$ with those of PbI_2 in Table 16. The important values of K_o^c, K_1^c, and K_1^s are all fairly close, but the rest all show significant deviations in the case of PbI_2. The value of K_2^c is very close to that of K_1^c, which means that the anion-cation compressional interaction dominates in PbI_2 more than in the other two crystals. The relative sizes of K_o^s and K_2^s are the reverse in PbI_2 which shows the importance of the anion-anion shear interaction.

Two independant elastic constants can be calculated

TABLE 17

COMPARISON OF FORCE CONSTANT RATIOS IN SELECTED LAYER CRYSTALS

Crystal	K_1^s/K_o^c	K_1^c/K_o^c (room temp.)
Graphite [51]	0.001	0.010
MoS_2 [51]	0.014	0.038
$CoCl_2$ [26]	0.021 ($\pm$0.002)	0.112 ($\pm$0.007)
$FeCl_2$ [26]	0.025 ($\pm$0.002)	0.090 ($\pm$0.005)
PbI_2	0.031 ($\pm$0.002)	0.14 ($\pm$0.03)

TABLE 18

COMPARISON OF FORCE CONSTANTS CALCULATED BY "ANDERSON" MODEL

(N/m) (room temp.)

	$FeCl_2$ [26]	$CoCl_2$ [26]	PbI_2
K_o^c	53.8 (±1.8)	52.5 (±2.2)	43 (±1)
K_2^c	29.4 (±2.0)	33.2 (±1.2)	6.6 (±1)
K_1^c	4.82 (±0.10)	5.86 (±0.10)	6.1 (±1)
K_o^s	35.0 (±1.5)	34.2 (±1.8)	9.4 (±1)
K_2^s	1.91 (±0.80)	5.91 (±0.93)	14.4 (±0.5)
K_1^s	1.37 (±0.05)	1.12 (±0.05)	1.33 (±0.05)

from the wave velocities in the c-direction: designated as C_{33} and C_{44}, C_{33} being related to the compressional force constants and C_{44} to the shear.

The wave velocities as obtained from the force constant dispersion curves of Figure 37 are:

v_t (room) = 0.88 ($\pm$0.02) x 10^5 cm/s

v_l (room) = 1.77 ($\pm$0.04) x 10^5 cm/s

v_t (50 K) = 0.99 ($\pm$0.02) x 10^5 cm/s

v_l (50 K) = 1.85 ($\pm$0.04) x 10^5 cm/s.

These "model" wave velocities agree more closely with the Brillouin [25] or ultrasonic [42] measurements than with the velocities derived from neutron dispersion curves.[24]

For symmetry directions, the elastic constants are related to the wave velocities by:

$$v^2 = C/\rho, \qquad (30)$$

where ρ is the density (6.10 ($\pm$0.01) g/cm^3 at room temperature and 6.23 ($\pm$0.01) at T=50 K). The results are, for room temperature:

C_{33} (neutron) = 14.5 ($\pm$1.5) GN/m^2

C_{33} (ultrasonic) = 18.8 ($\pm$0.2) GN/m^2

C_{33} (Brillouin) = 20.0 ($\pm$0.4) GN/m^2

C_{33} (model) = 19.1 ($\pm$0.9) GN/m^2

C_{44} (Raman) = 4.6 ($\pm$0.2) GN/m^2

C_{44} (neutron) = 5.3 ($\pm$0.7) GN/m^2

C_{44} (Brillouin) = 6.1 ($\pm$0.2) GN/m^2

C_{44} (model) = 4.7 ($\pm$0.2) GN/m^2,

and for T=50 K:

C_{33} (model) = 21.3 ($\pm$0.9) GN/m^2

C_{44} (Raman) = 7.0 ($\pm$0.4) GN/m^2

C_{44} (model) = 6.1 ($\pm$0.2) GN/m^2.

C_{33} (model) is dominated by the longitudinal neutron scattering data at about 300 K but despite this, it agrees more closely with the Brillouin and ultrasonic results. C_{44} (model) is based primarily on the Raman measurements at 400 K and thus falls in the lower range of the small spread of the transverse acoustic data.

An approximation which is used in some papers [23,24] is:

$$|\bar{w}^2_{2,3} - w^2_{2,3}| = \bar{w}^2_1. \qquad (31)$$

Using equations (24) and (26), we can write:

$$\bar{w}^2_2 - w^2_2 = -2K_1/m. \qquad (32)$$

Moreover, with equations (25) and (27) or (28), we get approximately:

$$\bar{w}^2_3 - w^2_3 \approx 2K_1/m. \qquad (33)$$

Finally, from equation (29), we have:

$$\bar{w}^2_1 \approx 4K_oK_1/(K_o(M+2m)+2K_1M) \approx 4K_1/(M+2m), \qquad (34)$$

which is an approximation to the above equations if $2m \gg M$. Since M = 207.19 amu and 2m = 253.81 amu the condition is obviously not satisfied and the deviation of equation (31) from agreement with the 6-parameter force constant model

TABLE 19

COMPARISON OF CALCULATED DAVYDOV SPLITTINGS

(cm^{-2})

	$\bar{u}_1^2$	$\lvert\bar{u}_2^2 - u_2^2\rvert$		$\lvert\bar{u}_3^2 - u_3^2\rvert$	
	observed	observed	model	observed	model
Compressional at room temp.	841 ($\pm$116)	-------	1632	-------	785
Compressional at T=50 K	961 ($\pm$186)	631 ($\pm$133)	1873	-------	913
Shear at room temp.	185 ($\pm$5)	576 ($\pm$144)	356	555 ($\pm$111)	171
Shear at T=50 K	231 ($\pm$6)	534 ($\pm$61)	447	-------	215

is at least 50%. Table 19 compares the splittings of the force constant model, of equation (31), and those observed, based on the actual acoustical frequencies.

As seen in Table 19 the approximations involved in comparing the $\bar{u}_1^2$ observed to the $|\bar{u}_3^2 - u_3^2|$ model cancel to a large extent. In general the force constant model does not give the observed splittings to any great accuracy but it does give the trends quite well.

4.1.3 Anharmonic Effects

One of the most obvious effects of anharmonicity in crystals is thermal expansion. A useful parameter in this respect is the Gruneisen constant. For axial crystals it has two values which can be defined as [52,53,54]

$$\gamma_a = V/C_\sigma((C_{11} + C_{12})\alpha_a + C_{13}\alpha_c) \quad (35)$$

and $$\gamma_c = V/C_\sigma(2C_{13}\alpha_a + C_{33}\alpha_c), \quad (36)$$

where V is the volume, C_σ is the heat capacity at constant stress equal to the heat capacity at constant pressure for low pressures, and the rest have previously defined meanings.

To obtain high temperature values of the Gruneisen constants the heat capacity was estimated from the low temperature measurements and from the vibrational structure as measured by the Raman and neutron scattering experiments. At infinite temperature this would mean all 9R modes would be completely excited for PbI_2. The heat capacity at constant volume would thus be 9R. At T=300 K this value

would be 8.9 R and at T=100 K it would be 8.2 R.

To calculate the heat capacity at constant pressure (or stress) we make use of the equation (ref. 55 p. 254 eq. 9.8-1)

$$C_p = C_v + B^2VT/X; \qquad (37)$$

where B is the volume expansivity (see sec. 3.5) and X is the bulk compressibility. For axial crystals this last can be written as:[2]

$$X = 2S_{11} + 2S_{12} + 4S_{13} + S_{33} \qquad (38)$$

where the S's are compliances readily calculated from the elastic constants (ref. 56 p. 358 eqs 13.4 & 13.5). We thus obtain a value of 6.4 ($\pm$1) x 10^{-11} m^2/N for X using the Brillouin results for the elastic constants.[25] If we use the same values for T=100 K and T=300 K we obtain rough estimates for C_p from equation (37) of 68 J/K.mol and 79 J/K.mol respectivily.

We thus have values for all the variables in equations (35) and (36) at T=300 K if we use the Brillouin results [25] and the expansivity data (see sec. 3.5). We therefore calculate γ_a(300 K) = 1.8 and γ_c(300 K) = 1.6. The values of the linear expansivities at T=100 K can be calculated from Figures 33 and 34 as α_a = 6 ($\pm$0.5) x 10^{-6}/K and α_c = 3.6 ($\pm$0.1) x 10^{-5}/K. There are no low temperature data on the elastic constants used in equations (35) and (36) and so we are forced to use the higher temperature values to estimate values of the Gruneisen constant at T=100 K.

The error caused by this should not be too great as the dominant effect is the temperature variation of the expansivities (nevertheless it was not thought useful to assign an experimental error to the Gruneisen constant calculation). We thus obtain values of $\gamma_a(100\ K) = 0.7$ and $\gamma_c = 0.9$.

For comparison the Gruneisen constants of Graphite are [2] $\gamma_a(1000\ K) = 0.37$, $\gamma_c(1000\ K) = 0.29$, $\gamma_a(300\ K) = -0.97$, and $\gamma_c(300\ K) = 0.44$. Therefore it can be seen that PbI_2 shows the same tendencies as graphite but to a much less extent. In particular a negative value of γ_a and thus α_a was not observed, however, lower temperature measurements would be useful in this regard.

The general definition of the mode Gruneisen constant is usually expressed as

$$\gamma = -\partial \ln w / \partial \ln V. \qquad (39)$$

For an axial crystal we can write [54]

$$\gamma_c = -(\partial \ln w / \partial \ln c)_a \qquad (40)$$

and $$\gamma_a = -\tfrac{1}{2}(\partial \ln w / \partial \ln a)_c. \qquad (41)$$

Since w^2 is directly proportional to the second derivative with respect to the displacement of the potential energy function (U) of a linear spring model (such as presented in sec. 4.1.1) equation (40) can be rewritten (ref. 57, p. 56 eq. 5.9 and p. 60 eq. 5.19):

$$\gamma_c = -\tfrac{1}{2}(\partial \ln U''(c-c_o)/\partial \ln c) = -\tfrac{1}{2}c(U'''(c-c_o)/U''(c-c_o)) \qquad (42)$$

where c_o is the equilibrium value of the lattice parameter at T=0 K.

For the Gruneisen constant to be non-zero (i.e. for thermal expansion to be possible) the potential energy function must contain an anharmonic term. Thus we have (ref. 58, p. 222 eq. 6-49):

$$U(c-c_o) = k(c-c_o)^2 - g(c-c_o)^3. \qquad (43)$$

The average displacement, as calculated from the Boltzmann factor (ref. 58, p. 222 eq. 6-53) is

$$\langle c-c_o \rangle = 3gK_BT/4k^2. \qquad (44)$$

Relating this to the expansivity we have

$$g/k^2 = 4c\alpha_c/3K_B. \qquad (45)$$

In the range T=100 K to 300 K we can assign this the value $g/k^2 = 2.4\ (\pm 0.1) \times 10^9\ N^{-1}$. We would expect that thermal expansion would take place primarily between the layers so that using $\frac{1}{2}K_1^c$ for k in equation (45) we obtain k = 3.5 ($\pm$0.5) N/m and g = 2.9 ($\pm$0.9) x 10^{10} N/m^2.

Substituting equation (43) in (42) we obtain

$$\gamma_c = 3cg/(2k-6g(c-c_o)), \qquad (46)$$

which if we use the lattice parameter data from section 3.5 ($c-c_o$ = 0.07 Å, c = 6.979 Å) we obtain for T=300 K; γ_c = 11 ($\pm$4). At T=100 K, where we can estimate $c-c_o$ = 0.02 Å, equation (46) gives; γ_c = 9 ($\pm$3). The magnitudes of the Gruneisen constants thus obtained are much too high, showing the crudeness of the model when applied to expansivity though the expected temperature variation is shown.

4.2 A Search for 2-Dimensional Effects

The layer-type structure of PbI_2 crystals might be expected to induce some 2-dimensional features into the lattice vibrational spectrum. This was considered by Dorner et al,[24] but they concluded from their measurements of dispersion curves, by inelastic neutron scattering, that the apparent dispersion in the acoustical branches was probably normal for a 3-dimensional structure. Supporting this was the observation of only slight anisotropy of the wave velocities (v_1(in the plane)/v_1(c-direction) = 1.17). However, their conclusion depended upon a reasonable extrapolation of w-q data to the region q→0. With the additional information about the low frequency region that we now have available, we can examine the matter of possible 2-dimensionality more carefully.

We shall first compare estimates of the average wave velocities obtained from the different kinds of experiments. To obtain the average wave velocity from the neutron scattering and Brillouin experiments, we make use of the tables compiled by Wolcott.[59] They involve the special case of hexagonal crystals and require the elastic constants as input. The polytype 2H of PbI_2 is trigonal and possesses an extra elastic constant, C_{14}, than the hexagonal symmetries. Its value is small ($\sim 3 \times 10^{10}$ dyn/cm^2, ref. 24, 25) compared to the other elastic constants and given also that for 4H

it should be zero, we will ignore it here.

One of the elastic constants needed, C_{13}, is not obtainable from the neutron scattering data [24] and so a value slightly lower than the Brillouin results,[25] in line with the variation in the other elastic constants, has been used. The results are

$$v_{av}(\text{neutron, } 300 \text{ K}) = 1.04\ (\pm 0.05) \times 10^5 \text{ cm/s},$$

and $v_{av}(\text{Brillouin, } 300 \text{ K}) = 1.18\ (\pm 0.03) \times 10^5$ cm/s.

The average velocity calculated from the heat capacity is (sec. 3.3)

$$v^c_{av}(T \to 0 \text{ K}) = 1.151\ (\pm 0.005) \times 10^5 \text{ cm/s}.$$

This value will be lower at room temperature. The only data on the temperature variation of the wave velocity is from the Raman data on the transverse acoustic branch in the c-direction. This shows a decrease of about 22% from 400 K to 50 K; let us say about 12 to 15% for 300 K to 0 K. Because of the anisotropy of the crystal the average velocity will not decrease by that great an amount. A 10% decrease, which is not unreasonable, would bring the heat capacity measurement into agreement with the neutron scattering data. The Brillouin result, however, can not be brought into agreement.

The heat capacity measurements correspond to temperatures $T < 1$ K and therefore to vibrational frequencies of $f < 21$ GHz ($0.7\ \text{cm}^{-1}$). The Brillouin measurements correspond to the same range $u \sim 0.5\ \text{cm}^{-1}$, but the neutron

scattering to much higher frequencies u~10 to 30 cm^{-1}. Therefore the explanation to this discrepancy may lie in the high temperature (i.e. anharmonic) behavior of PbI_2.

One of the main tests for 2-dimensionality in crystals is the appearance of negative phonon dispersion in one or more directions. For graphite this is shown quite well by Figures 6 and 8 of reference 1 which show a strong quadratic dependance of the phonon dispersion in the transverse modes of directions in the plane of the layers but not in the c-direction. Negative dispersion in directions parallel to the layers is a general property of layered crystals.[60] A closely related effect is negative expansion, and the related Gruneisen constant, in the plane of the layers as discussed in section 4.1.3.

It has been observed experimently in such crystals as $TiSe_2$ [61] and $FeCl_2$ [62] which are considerably less layer-like than graphite (see sec. 4.1.2 and Table 17). The amount of negative dispersion is, however, correspondingly less evident especially in $FeCl_2$. This has also been examined by a shell model calculation of Pasternak [63] on $FeCl_2$. PbI_2 is less layer-like than these (see sec. 4.1) and would be expected to show even less negative dispersion. In fact, from the neutron scattering data,[24] it appears to show none.

The behavior at low momentum transfers is shown by the Brillouin measurements [25] which tend to give higher wave velocities than the neutron scattering data, thereby denying

negative dispersion (at room temperatures it must be emphasized). The heat capacity average wave velocity as discussed earlier leaves the question more open for low temperatures. The last piece of evidence in this regard comes from the dispersive term of the heat capacity of section 3.3. This gives the average dispersion and, as mentioned, leaves open the possibility of a slight negative contribution in some directions.

Because of its layer structure the thermal conductivity of graphite is very low [64] about 5μ W/cm K at T=1 K. The thermal conductivity of PbI_2 is comparable to this; about 1.2μ W/cm K at T=1 K. However, the mean free path of PbI_2 is extraordinarily low when calculated by the Debye model (see sec. 3.3). This leads one to conclude that the reason for the low thermal conductivity in PbI_2 must be quite different than in graphite.

CHAPTER 5

CONCLUSION

Although it is not very sophisticated, the force constant model discussed in Chapter 4 has proved to be useful for interpreting the vibrational properties of PbI_2. It leads to the conclusion that PbI_2 displays much less 2-dimensional character than graphite or MoS_2. The existence of such 2-dimensional effects as negative phonon dispersion and negative expansivity in the plane of the layers is just barely discernable. With respect to the interatomic forces, the apparent importance of the iodine-iodine interaction indicates that the forces are more covalent than ionic.

As was seen in section 4.1.3, the force constant model cannot adequately account for the anharmonicity evident in the expansivity, even when an anharmonic term is added.

There are two problems that remain unresolved. The exact nature of the low thermal conductivity and the seemingly small phonon mean free path has not been resolved. More extensive thermal conductivity measurements than those presented in this thesis might shed some light on this matter.

The discrepancy between the wave velocities obtained

from the Brillouin spectra and from neutron scattering experiments still exists and this indicates that investigations of both types of low temperature experiments would be worthwhile. It would be particularly valuable to obtain the actual shape of the acoustical phonon branches at low momenta as a function of temperature.

A useful addition to the spectroscopic information provided by the Raman experiments performed here would be a study of infrared spectra of the higher polytypes. This could help to refine the exact shape of some of the phonon dispersion curves.

The next stage of refinement for calculations should probably be of the shell model type performed on the $FeCl_2$ lattice by Pasternak.[63] That would be facilitated if the additional experiments mentioned above could be done.[65,66,67,68]

REFERENCES

1. R. Nicklow, N. Wakabayashi, and H. G. Smith; Phys. Rev. B 5, 4951 (1972).
2. R. W. Munn; J. Phys. C 5, 535 (1972).
3. W. DeSorbo and G. E. Nichols; J. Phys. Chem. Solids 6, 352 (1958).
4. A. R. Verma and P. Krishna; Polymorphism and Polytypism in Crystals, John Wiley and Sons Inc., (1966).
5. L. S. Ramsdell; Am. Mineralogist 32, 64 (1947).
6. J. I. Hanoka, K. Vedam, and H. K. Henisch; Proceedings of an International Conference on Crystal Growth, Boston, June 20-24 1966, ed. H. S. Peiser, Pergamon Press, p. 369 (1967).
7. A. Grisel and Ph. Schmid; Phys. Stat. Sol. (b) 73, 587 (1976).
8. R. Prasad; J. Phys. Chem. Solids 37, 337 (1976).
9. D. W. Feldman, J. H. Parker, Jr., W. J. Choyke, and L. Patrick; Phys. Rev. 173, 787 (1968).
10. L. Patrick; Phys. Rev. 167, 809 (1968).
11. D. W. Feldman, J. H. Parker, Jr., W. J. Choyke, and L. Patrick; Phys. Rev. 170, 698 (1968).
12. C. H. Hodges; Phys. Rev. 187, 994 (1969).
13. M. R. Tubbs; Phys. Stat. Sol. (b) 49, 11 (1972).
14. T. Yao and I. Imai; Solid State Comm. 9, 205 (1971).

15. A. E. Dugan and H. K. Henisch; J. Phys. Chem. Solids 28, 971 (1967).

16. F. Levy, A. Mercier, and J. P. Voitchovsky; Solid State Comm. 15, 819 (1974).

17. A. E. Dugan and H. K. Henisch; Phys. Rev. 171, 1047 (1968).

18. M. Yashiro, T. Goto, and Y. Nishina; Solid State Comm. 17, 765 (1975).

19. L. C. Thanh, C. Depeursinge, F. Levy, and E. Mooser; J. Phys. Chem. Solids 36, 699 (1975).

20. R. Zallen and M. L. Slade; Solid State Comm. 17, 1561 (1975).

21. J. P. Mon; C. R. Acad. Sc. Paris B 262, 493 (1966).

22. M. C. Carabatos; C. R. Acad. Sc. Paris B 272, 465 (1971).

23. S. Nakashima; Solid State Comm. 16, 1059 (1975).

24. B. Dorner, R. E. Ghosh, and G. Harbeke; Phys. Stat. Sol. (b) 73, 655 (1976).

25. J. Sandercock; Festkörperprobleme XV, 183 (1975).

26. A. Anderson and J. P. Todoeschuck; Can. J. Spect. 22, 113 (1977).

27. R. E. Liesegang; Phot. Archiv. 221 (1896).

28. M. Flicker and J. Ross; J. Chem. Phys. 60, 3458 (1974).

29. H. K. Henisch; Crystal Growth in Gels, The Pennsylvania State University Press (1970).

30. H. K. Henisch, J. Dennis, and J. I; Hanoka; J. Phys. Chem. Solids 26, 493 (1965).

31. J. Dennis and H. K. Henisch; J. Electrochemical Society 112, 1240 (1965).

32. V. Vand and J. I. Hanoka; Mat. Res. Bull. 2, 241 (1967).

33. R. S. Mitchell; Zeitschrift für Kristallographie 111, 372 (1959).

34. R. Prasad and O. N. Srivastava; J. Crystal Growth 19, 11 (1973).

35. T. Minagawa; Acta Cryst. A31, 823 (1975).

36. K. Jain, W. T. Wozniak, and M. V. Klein; Applied Optics 14, 811 (1975).

37. K. Lushington and J. A. Morrison; to be published (1978).

38. O.P. Bansal, J. A. Morrison, and E.L. Richards; to be published (1978).

39. R. W. G. Wyckoff; Crystal Structures 2nd ed. vol. 1, Interscience Publishers (1963).

40. W. G. Fateley, N. T. McDevitt, and F. F. Bentley; Applied Spectroscopy 25, 155 (1971).

41. S. Montero and W. Kiefer; J. Raman Spectroscopy 1, 565 (1973).

42. W. Rehwald; unpublished work quoted in reference 24.

43. R. Clasen, H. Burkhard, G. Harbeke, and G. Lang; Verhandl. DPG (VI) 10, 391 (1975).

44. G. Lucovsky, R. M. White, W. Y. Liang, R. Zallen, and Ph. Schmid; Solid State Comm. 18, 811 (1976).

45. T. H. K. Barron and J. A. Morrison; Can. J. Phys. 35, 799 (1957).

46. T. H. K. Barron, W. T. Berg, and J. A. Morrison; Proc. Roy. Soc. A 250, 70 (1959).

47. H. S. Carslaw and J. C. Jaeger; Conduction of Heat in Solids 2nd ed. Oxford University Press (1959).

48. D. B. Sirdeshnakh and V. T. Deshpande; Current Science 41, 210 (1972).

49. H. Fizeau; Comp. Rend. 64, 314 (1867).

50. W. Klemm, W. Tilk, and S. V. Mullenheim; Z. Anorg. Allg. Chem. 176, 1 (1928).

51. R. Zallen and M. Slade; Phys. Rev. B 9, 1627 (1974).

52. R. W. Munn; Adv. Phys. 18, 515 (1969).

53. R. W. Munn; Phil. Mag. 17, 433 (1968).

54. T. H. K. Barron and R. W. Munn; Phil. Mag. 15, 85 (1967).

55. M. Tribus; Thermostatics and Thermodynamics, D. Van Nostrand Company, Inc. (1961).

56. D. C. Wallace; Solid State Physics 25 p. 301, Academic Press (1970).

57. M. Born and K. Huang; Dynamical Theory of Crystal Lattices, Oxford University Press (1954).

58. C. Kittel; Introduction to Solid State Physics 4th ed. Wiley (1971).

59. N. M. Wolcott; J. Chem. Phys. 31, 536 (1959).

60. T. H. K. Barron and T. G. Gibbons; J. Phys. C 7, 3269 (1974).

61. W. G. Stirling, B. Dorner, J. D. N. Cheeke, and J. Revelli; Solid State Comm. 18, 931 (1976).

62. W. B. Yelon, R. Scherm, and C. Vettier; Solid State Comm. 15, 391 (1974).

63. A. Pasternak; J. Phys. C 9, 2987 (1976).

64. D. O. Edwards, R. E. Sarwinski, P. Seligmann, and J. T. Tough; Cryogenics 8, 392 (1968).

65. N. Wakabayashi; Il Nuovo Cimento 38, 256 (1977).

66. G. Lucovsky and R. M. White; Il Nuovo Cimento 38, 290 (1977).

67. R. Zeyher; International Conference on Lattice Dynamics Paris, Sept. (1977).

68. A. Frey; Thesis, Stuttgart, unpublished (1977).